Computational Acoustic Beamforming for Noise Source Identification for Small Horizontal Axis Wind Turbines

by

Ping Ma

A thesis
presented to the University of Waterloo
in fulfillment of the
thesis requirement for the degree of
Doctor of Philosophy
in
Mechanical and Mechatronics Engineering

Waterloo, Ontario, Canada, 2017

Examining Committee Membership

The following served on the Examining Committee for this thesis. The decision of the Examining Committee is by majority vote.

External Examiner	Prof. Xinfeng Gao (Colorado State University)
Supervisor(s)	Prof. Fue-Sang Lien Prof. Eugene Yee
Internal Member	Prof. Gordon Stubley Prof. Zhongchao Tan
Internal-external Member	Prof. Siva Sivoththaman

Author's Declaration

I hereby declare that I am the sole author of this thesis. This is a true copy of the thesis, including any required final revisions, as accepted by my examiners.

I understand that my thesis may be made electronically available to the public.

Abstract

This thesis develops a computational acoustic beamforming (CAB) method for identification of sources of small wind turbine noise. The methodology consists of three components: computational fluid dynamic (CFD), acoustic propagation and acoustic beamforming components. Each component of the CAB method is validated on the component level. The numerical results agree well with the experimental data for the validation of each component.

The CAB method is then validated on the whole system level using the NACA 0012 airfoil trailing edge noise case. The predicted acoustic maps are in excellent agreement with the corresponding observed acoustic maps obtained from wind-tunnel experiments. It is found that the spatial resolution of the acoustic maps increases with increasing frequency. It is also found that the Archimedean spiral array has a better spatial resolution than the star array at all frequencies of interest. Furthermore, an Archimedean spiral array exhibits better signal to noise ratio (SNR) at frequencies below 1000 Hz, but poorer SNR at frequencies above 1000 Hz when compared to the performance of a star microphone array.

Following these validation studies, the CAB methodology was applied to the identification of noise sources generated by a commercial small wind turbine (WINPhase 10 wind turbine). Despite the coarse grid and large time step used in the CFD simulations, the simulated aerodynamic results (wind turbine power output) and the aeroacoustic results (A-weighted SPL spectra) are in good agreement with some field measurements for this wind turbine. The simulated acoustic maps reveal that the blade tower interaction and the wind turbine nacelle are two possible noise generation mechanisms in the range of frequencies between 200 and 630 Hz for this small wind turbine.

Acknowledgements

I cannot express enough appreciation to my co-supervisors Prof. Fue-Sang Lien and Prof. Eugene Yee for their helpful advice and guidance. I would like to thank Prof. Gordon Stubley, Prof. Zhongchao Tan, Prof. Siva Sivoththaman and Prof. Xinfeng Gao for taking time from their busy schedule to be part of my exam committee. Finally, to my husband and parents, I would never have finished this without your patience and selfless support.

Dedication

To my lost baby

Table of Contents

List of Figures

List of Tables

Nomenclature

A_{WT}	Wind turbine swept area
c	Speed of sound
c_{d_cy}	Cylinder drag coefficient
c_D	Airfoil drag coefficient
c_k	Thermal conductivity
c_{l_cy}	Cylinder lift coefficient
c_L	Airfoil lift coefficient
c_p	Heat capacity at constant pressure
c_{p_cy}	Cylinder surface pressure coefficient
c_{Power}	Wind turbine power coefficient
C	Airfoil chord length
d	Normal distance from the wall
$\tilde{d}$	Characteristic length scale in DDES
d_m	Minimum distance between the two microphones on a microphone array
D	Wind turbine rotor diameter
D_a	Drag force applied on airfoil surface
D_{cy}	Cylinder diameter
D_{ref}	Reference characteristic length to calculate the non-dimensional time step
D_ω	Cross diffusion term in $k-\omega$ SST turbulence model
e_0	Total energy
e_{0_r}	Relative total energy
$f=0$	Function that describes the integration Surface for FW-H acoustic analogy calculation
f_v	Van Driest damping function
G	Free space Green's function $G=\delta(\mathrm{g})/4\pi\mathrm{r}$
G_k	Generation of turbulence kinetic energy

$\tilde{G}_k$	Generation of turbulence kinetic energy
$G_{\tilde{\nu}}$	Production term of modified turbulent viscosity
G_ω	Generation of ω
h	Airfoil maximum thickness
$H(f)$	Heaviside function
k	Local turbulent kinetic energy
l_ε	Characteristic length scale
L	Measurement distance
L_a	Lift force applied on airfoil surface
L_c	Characteristic length
L_{cy}	Gap region length for tandem cylinders case
L_i	Components of vector defined in Eq. (3.38)
L_M	$= L_i M_i$
$\dot{L_r}$	$= \dot{L}_i \hat{r}_i$
L_{span}	Airfoil span width
M	Magnitude of Mach number of source
M_i	Components of local Mach number vector of source
M_n	Mach number of source in normal direction, $M_n = n_i M_i$
M_r	Mach number of source in radiation direction, $M_r = \hat{r}_i M_i$
Ma	Mach number
n_i	Normal direction to the boundary surface defined by $f = 0$, $n_i = \partial f / \partial x_i$
p	Pressure
p_m	Measured pressure signals for microphone m
$\mathrm{P_{ij}}$	Compressive stress tensor
ΔP_{ij}	Local force intensity
P_{WT}	Wind turbine power
$\mathbf{q}$	Heat flux

r	Rotation radius
r	Distance between receiver and sound source, $r = \|x - y\|$
$\hat{r}_i$	Component of unit radial vector, $\hat{r}_i = \frac{\partial r}{\partial x_i}$
r_m	Location vector for microphone m
r_{WT}	Radial location on wind turbine rotor plane
rpm	Round per minute
R	Wind turbine rotor radius
R_{BF}	Acoustic beamformer spatial resolution
$R_{specific}$	Specific gas constant
Re	Reynolds number
Re_{y}	Wall distance Reynolds number
s	Distance between assumed source and microphone array center
s_m	Distance between the assumed source and microphone m
S	Modulus of the mean rate of strain tensor
S_a	Airfoil frontal area
S_{ij}	Rate of strain tensor
t	Time
t^*	Non-dimensional time step, $t^* = tU_{ref}/D_{ref}$
T	Temperature
T_{ij}	Lighthill stress tensor
u	Flow velocity magnitude
u_i	Components of flow velocity
$\mathrm{u_n}$	Local fluid velocity in direction normal to the boundary surface, $u_n = u_i n_i$
u_r	Local fluid velocity in the radial direction, $u_r = u_i r_i$
u_{r_i}	Components of relative velocity
u^*	Friction velocity
U_i	Components of vector defined in Eq. (3.37)

$\dot{U}_n$	$= \dot{U}_i \hat{n}_i$
$U_{\dot{n}}$	$= U_i \dot{\hat{n}}_i$
U_{ref}	Reference velocity to calculate the non-dimensional time step
v_i	Component of surface boundary velocity $\boldsymbol{v}$
v_n	Local normal velocity of the boundary surface, $v_n = -\partial f / \partial t$
v_r	Surface boundary velocity in radiation direction, $v_r = v_i r_i$
v_{r_i}	Components of rotational velocity
v_{ref}	Reference wind speed for calculation of one-seventh power law velocity profile
v_{wind}	Wind speed
V	Cell volume
w_m	Weighting coefficient for microphone m
x_i	Components of position vector
$(\boldsymbol{x}, t)$	Receiver space-time variables
y^+	Dimensionless wall distance
$(\boldsymbol{y}, \tau)$	Sound source space-time variables
y_{ref}	Reference height for calculation of one-seventh power law velocity profile
y_{WT}	Height above the ground for calculation of one-seventh power law velocity profile
Y_k	Dissipation of k
$Y_{\tilde{\nu}}$	Destruction term of modified turbulent viscosity
Y_ω	Dissipation of ω
α	Inverse effective Prandtl number
γ	Heat capacity ratio
δ_{ij}	Kronecker delta
$\delta(f)$	Dirac delta function
ε	Turbulent dissipation rate
ζ	Bulk viscosity

η	Ratio of the turbulent to mean strain time scale
θ	Local angle between normal to the surface and the radial direction at the emission time, $cos\theta = n_i r_i$
θ_{cy}	Cylinder angular position defined by Figure 4.20
ϑ_i	Grid point i at the acoustic beamforming source plane
κ	Von-Karman constant
λ	Wavelength
μ_{eff}	Effective viscosity
μ_t	Turbulent eddy viscosity
μ	Dynamic viscosity
ν	Kinematic viscosity
$\tilde{\nu}$	Modified turbulent kinematic viscosity
υ_t	Turbulent kinematic viscosity
ξ	Roughness function
ϖ	Wave number
ρ	Density
σ_{ij}	Viscous stress tensor
$\sigma_{r_{ij}}$	Relative viscous stress tensor
ς^*	Trailing edge thickness
τ_{ij}	Reynolds stress
ω	Dissipation per unit turbulence kinetic energy
ω_{WT}	Wind turbine rotational speed
Δ	Length scale in LES
Δ_{im}	Propagation time from source plane grid point i to microphone m
$\Delta_m(\psi)$	Time delay for microphone m with a select direction characterized by a unit vector $\boldsymbol{\psi}$
$\Delta_{mspherical}$	Time delay for microphone m for spherical wave incidence

Λ	Maximum computational cell dimension in the x-, y- and z- directions
Π	Microphone array diameter
Ω_{ij}	Rate of rotation tensor

Subscripts/Accent

0	Fluid properties at rest
L	Loading noise
n	Component in normal direction
ret	Retarded time
$\dot{}$	Source-time differentiation
$\widehat{\ }$	Favre (density-weighted) averaged
$\bar{}$	Generalized function
$=$	Time averaged
$\overline{\Box}^2$	d'Alembertian operator, $\overline{\Box}^2 = \left[(1/c^2)\left(\bar{\partial}^2/\partial t^2\right)\right] - \bar{\nabla}^2$
$\langle \ \rangle$	Time average, $\langle f(t)\rangle = \frac{1}{T}\int_0^T f(t)dt$

List of Abbreviations

ADM	Actuator Disc Method
ALT	Actuator Line Technique
AOA	Angle of Attack
BEM	Blade Element Method
CAA	Computational Aero-Acoustics
CAB	Computational Acoustic Beamforming
CDS	Central Differencing Scheme
CFD	Computational Fluid Dynamics
CFL	Courant-Friedrichs-Lewy number
DAS	Delay And Sum
DDES	Delayed Detached Eddy Simulation
DES	Detached Eddy Simulation
EAM	Enhanced Amplitude Modulation
FW-H	Ffowcs Williams and Hawkings
GIS	Grid Induced Separation
HAWT	Horizontal Axis Wind Turbine
IDDES	Improved Delayed Detached Eddy Simulation
LES	Large Eddy Simulation
MRF	Multiple Reference Frame
MSD	Modeled Stress Depletion
MSL	Maximum Side-lobe Level
N-S	Navier-Stokes
NSI	Noise Source Identification
OASPL	Overall Sound Pressure Level
PIV	Particle Image Velocimetry
PSD	Power Spectral Density

RANS	Reynolds Averaged Navier-Stokes
RMS	Root Mean Square
SGS	Subgrid-Scale
SNR	Signal to Noise Ratio
SPL	Sound Pressure Level
SPLA	A-weighted Sound Pressure Level
TOA	Time of Arrival
TSR	Tip Speed Ratio
URANS	Unsteady Reynolds Averaged Navier-Stokes

Chapter 1

Introduction

1.1 Wind Turbine Operation Mechanism

A wind turbine is a rotary device that extracts energy from the wind. Mechanical energy from the wind turbine is converted to electricity (wind turbine generator). The wind turbine which rotates through a horizontal axis as shown in Figure 1.1 is called a horizontal axis wind turbine (HAWT).

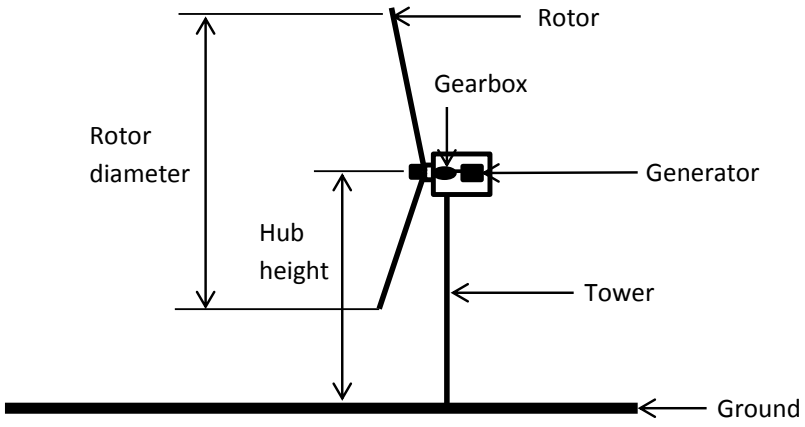

Figure 1.1: Schematic plot of a HAWT.

Wind turbines work by converting the kinetic energy in the wind first into rotational kinetic energy in the rotor and then electrical energy by the generator. The wind power available for conversion mainly depends on the wind speed and the swept area of the turbine:

$$Power = \frac{1}{2}\rho A_{WT} v_{wind}^3, \quad (1.1)$$

where ρ represents the air density, A_{WT} is the wind turbine rotor swept area and v_{wind} is the undisturbed wind speed. Albert Betz (German physicist) concluded in 1919 that no wind turbine can convert more than 16/27 (59.3%) of the kinetic energy of the wind into mechanical energy turning a rotor (Betz limit). The theoretical maximum power efficiency of any kind of wind turbine is therefore 0.59.

1.2 Small Wind Turbine Industry Development

The international standardization body, International Electrotechnical Commission (IEC), in their standard IEC 61400-2 [1], defines a small wind turbine as having a rotor swept area of less than 200 m^2, equating to a rated power generation of approximately 50 kW at a voltage below 1000 V AC or 1500 V DC. However, technically, there are several countries setting up their own definition of what constitutes a small wind turbine. In consequence, differences in the upper limit of power capacity of a small wind turbine can range between 15 and 100 kW [2].

The small wind turbine industry has seen a rapid growth and maturity since 2010 with political and regulatory support, such as Feed-In Tariffs (FITs), net metering, tax credits and capital subsidies. At the beginning of 2010, the American Wind Energy Association (AWEA) established performance and safety standards for small wind turbines [3]. These standards include not only the measurement and publication of standardized power

curves, but also the measurement and reporting of noise emissions from small wind turbines. This performance standard mostly follows the British standard for small wind turbines and the international standard for large wind turbines. In April 2010, Great Britain launched a comprehensive system of FITs for projects up to 5 MW with six different tranches for wind turbines. Three of the six tranches refer to small wind turbines. Statistics showed that this FIT policy had contributed to four fifths of the newly installed small wind capacity in the country, which resulted in over 100 MW of installed capacity in 2012 [4]. Figure 1.2 shows the total cumulative installed units for small wind turbines by the year 2013. In North America, the United States reached a cumulative capacity of almost 1 GW from the small wind turbine industry by the end of 2014, reflecting nearly 74,000 wind turbines deployed nationwide. Among them, 63.6 MW of new small wind turbine capacity was added in 2014, representing nearly 1,700 units and $170 million in investment across 24 states [5]. In March 2015, Denmark and Poland introduced new FITs for small wind turbines with an attractive remuneration. The World Wind Energy Association (WWEA) estimated that a cumulative total more than a million units of small wind turbines have been installed by the end of 2015 worldwide [2].

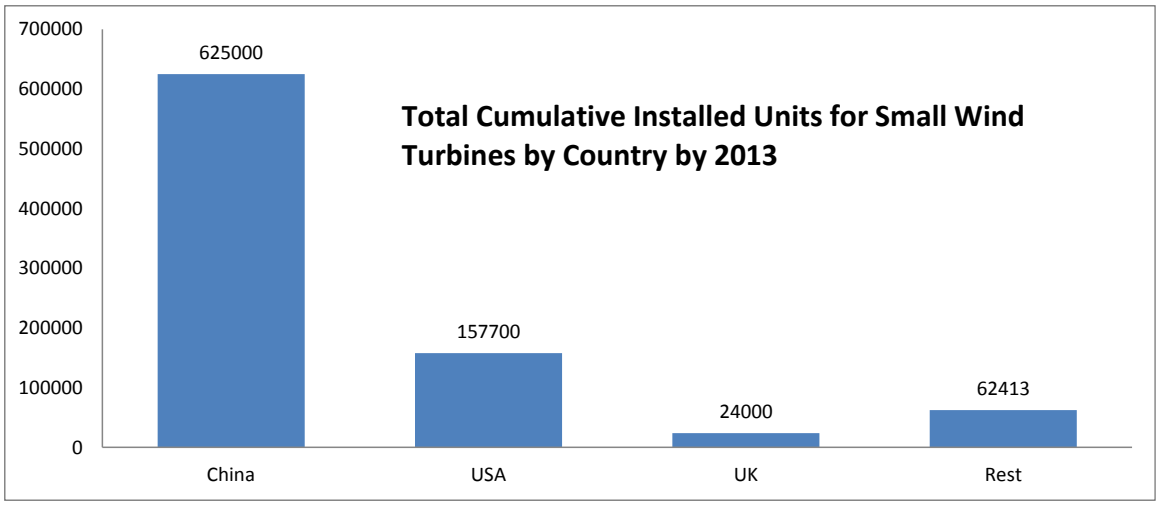

Figure 1.2: Total cumulative installed units by country for small wind turbines [5].

Small wind turbines are a reliable and sustainable off-grid solution in developing and emerging markets [6]. First of all, small wind turbines can be easily combined with other energy sources within a hybrid system, such as solar or diesel, which makes it possible to optimize the usage of available resources and avoid dependency on just one energy source with limited availability for a certain time or a particular season of the year. Secondly, as interest in electrification of remote and rural areas increases, small wind turbines offer a very advantageous cost-competitive solution for off-grid applications [6]. In addition, as the price of conventional energy resources, like fossil fuels, is constantly rising while the cost of wind energy is gradually declining, it is expected that more rigorous policies will be deployed to support small wind turbine investment.

1.3 Small Wind Turbine Noise Issue

Since small wind turbines are often installed in the proximity of residential (populated) areas with some particularly designed to be placed on the roofs of the buildings as

shown in Figures 1.3 - 1.5, the noise issue is a critical issue affecting the continued development and use of small wind turbines. However, similar to other emerging industries, noise issues are of secondary importance for small wind turbine manufacturers. Indeed, manufacturers still view the fabrication process and the total wind turbine cost (affordability) as the most important issues that need to be considered for the widespread use of small wind turbines [7]. In addition, the lack of regulations with respect to the noise generated by small wind turbines has curtailed research in this area in both academia and industry. Nevertheless, as more and more people are incentivized to install small wind turbines to supply their electricity needs at home, the noise issues accruing from the operation of small wind turbines will become so critical that rigorous policies will need to be formulated by local and federal agencies to govern the permissible (acceptable) sound levels of noise sources generated by use of small wind turbines in residential areas.

Figure 1.3: Wind turbines on the roof of Boston Museum of Science in Massachusetts [8].

Figure 1.4: Wind turbines in the Strata Tower in London, UK [9].

Figure 1.5: Vertical wind turbine on the roof of Witherspoon's pub known as "The Kettleby Cross" in Melton Mowbray [10].

In order to resolve the noise issues associated with the operation of small wind turbines, it is important to determine the locations of the primary sources of sound generation on a wind turbine. To this purpose, it is noted that application of a systematic methodology for noise source identification (NSI) would enable the localization of the sound sources on a wind turbine. This in turn would allow engineers to redesign the wind turbine (e.g., blades, hub, tower) in order to reduce (or minimize) the noise generation. Currently, the NSI methodology for small wind turbines relies mainly on the use of acoustic

beamforming measurements. This experimental methodology for noise source determination utilizes arrays of microphones in various geometric configurations for the measurement of the sound field generated by the wind turbine. Subsequently, the array-based microphone sound measurements are processed using high-resolution acoustic beamforming algorithms for the noise source identification. However, the cost of conducting an acoustic beamforming measurement campaign for the noise characterization of a wind turbine is high, especially when it is necessary to use a complex array involving a very large number of microphones. Furthermore, it is frequently difficult to deploy a microphone array at the optimal measurement location for the noise source identification, owing to some environmental limitations (e.g., obstacles such as trees, rocks, buildings, etc.). As a consequence, there are very few researchers that have conducted acoustic beamforming measurements for small wind turbines [11]-[13].

1.4 Computational Acoustic Beamforming Method

In view of the limitations arising from the use of experimental acoustic beamforming for noise characterization of small wind turbines, this thesis proposes an alternative methodology. More specifically, this thesis proposes to use a computational acoustic beamforming (CAB) methodology for the identification of noise sources on a small wind turbine. The methodology is composed of three components: CFD, acoustic propagation and acoustic beamforming components.

The CAB methodology was first proposed by Li [14] where it was used to identify the sources of trailing edge noise for the NACA 0012 airfoil. However, in this application, Li used the methodology to compute only one acoustic map at 800 Hz which was found to be in poor conformance with the corresponding experimental measurement [15]. The poor agreement between the predicted and measured results for the acoustic map was probably due primarily to the coarse mesh used in the computational fluid dynamics (CFD) simulation, which caused an earlier flow separation along the leading edge of the airfoil which in turn inhibited the interaction between the turbulent boundary layer and the trailing edge of the airfoil.

To resolve the discrepancies between the experiment and numerical results reported by Li [14] for the NACA 0012 airfoil trailing edge noise, this thesis considers a more computationally demanding and sophisticated implementation of the CAB methodology. Firstly, in the generalization of the CAB methodology, this thesis will use higher fidelity models for prediction of the flow field. In particular, a large-eddy simulation (LES) with a very fine mesh ($y^+ \leq 1$) will be used to compute the flow around the NACA 0012 airfoil in comparison to what was used by Li [14] in his original implementation of the CAB methodology where the flow was determined using an improved delayed detached eddy simulation (IDDES) with a rather coarse mesh ($y^+ > 30$). Secondly, with reference to certain conclusions reached in some experimental acoustic beamforming studies [15]-[18], this thesis extends the CAB methodology described by Li [14] to include a diagonal removal process for acoustic beamforming and to include various geometric

configurations for the microphone array. Thirdly, this thesis generalizes the CAB methodology to incorporate a spherical wave incidence acoustic beamforming algorithm and applies the methodology to cases where the microphone arrays were located in the near and transition regions of the sound sources. Fourthly, the impermeable formulation of the Ffowcs Williams and Hawkings (FW-H) for the static source which has been used by Li [14] in the NACA 0012 airfoil trailing edge noise case is generalized to include scenarios of moving sound sources. Furthermore, the most general formulation of the FW-H equation for acoustic (sound) propagation, the permeable formulation of the FW-H equation, has also been included in the CAB methodology. The generalization of the CAB methodology considered herein will allow the application of this methodology for noise source identification to more complex problems (e.g., localization of noise source generation on a wind turbine and other complicated turbomachinery).

The objectives of this thesis are:

- Validate each component of the CAB method using available experimental data;
- Validate the whole CAB method with the experimental data for airfoil trailing edge noise localization; and
- Investigate the WINPhase 10 small wind turbine noise source information by applying the CAB method on this wind turbine.

The CAB methodology has the following advantages when compared with the use of conventional acoustic beamforming measurements for noise source identification. Firstly, with the increasing availability of relatively inexpensive high-speed computational platforms, the application of the CAB methodology will be more cost-effective than the use of acoustic beamforming measurements for noise source identification of complex turbomachinery. Secondly, the CAB methodology can be applied to cases where it is difficult to conduct the acoustic beamforming measurements owing to some environmental limitations (e.g., obstacles that limit the optimal placement of the microphone arrays). This limitation is absent in the virtual environment of where the CAB methodology is applied. Thirdly, given the flexibility for experimentation with the microphone array geometry and with the particular form of the acoustic beamforming algorithm used for the noise source identification, the CAB methodology can be used as an optimization tool to identify the best microphone array geometry that needs to be used with a specific acoustic beamforming algorithm for characterization of the noise sources for a particular form of turbomachinery. Fourthly, the CAB methodology provides both the flow field information and the noise source information for a particular form of turbomachinery, whereas the application of the conventional acoustic beamforming measurements only provides the noise source information. This additional flow field information can potentially help researchers to gain deeper insights into the physical mechanisms responsible for the identified noise sources. It is expected that this improved understanding will allow scientists and engineers to redesign turbomachinery to minimize noise.

This thesis is organized as follows. Chapter 2 reviews the literature on numerical simulations of wind turbine aerodynamics and aeroacoustics as well as acoustic beamforming experiments used for wind turbine noise source localization. Chapter 3 describes the proposed CAB method and the models used in the three principal components which comprise the CAB method. Chapter 4 presents the validation cases for each of the components comprising the CAB method. Chapter 5 presents a validation of the CAB method on a whole system level. In Chapter 6, the CAB method is applied to a commercial small horizontal axis wind turbine for localization of the noise source on the rotor plane. Conclusions and future work are summarized in Chapter 7.

Chapter 2

Literature Review

Each of the three components comprising the CAB method is itself a very active research area. In this chapter, reviews of the research area corresponding to each component in the CAB method are presented. For CFD component, Section 2.1 reviews the research conducted on wind turbine aerodynamic prediction. For the acoustic propagation component, Section 2.2 provides a review on wind turbine acoustic prediction. For the acoustic beamforming component, Section 2.3 presents a review on wind turbine noise source identification using the acoustic beamforming method.

2.1 Review of Wind Turbine Aerodynamic Simulations

The industrial design codes for wind turbines are still based on the semi-empirical method: Blade Element Method (BEM) [19]. The main idea underpinning the BEM is to analyze the wind turbine flow field by dividing the wind turbine blade into a number of independent elements and calculating the aerodynamic forces on each of these elements using tabulated airfoil data, which were obtained from wind-tunnel measurements that have been subsequently corrected for three-dimensional effects. Inputs for the BEM-based models generally include blade geometric parameters and the wind turbine operating conditions. Outputs from the model are local Reynolds number, local angle of attack (AOA) and boundary-layer displacement thickness, which can be used as relevant inputs to a semi-empirical noise prediction model.

In order to deal with various flow situations encountered in practice, it is necessary to introduce different empirical corrections to BEM models. Such situations include phenomena related to dynamic inflow, yaw misalignment, tip loss and heavily loaded rotors. Tangler [20] suggested that there may be considerable uncertainty involved in the incorporation of these empirical corrections into BEM models.

The Actuator Disc Method (ADM), which represents roughly an extension of the BEM models, was integrated in an Euler or Navier-Stokes (N-S) frame by many researchers [21], [22]. In ADM, the Euler (or N-S) equations are typically solved by a second order accurate finite difference/volume scheme, as in a usual CFD computation. In this approach, the geometry of the blades and the viscous flow surrounding the blades are not resolved. Instead, the swept surface of the rotor is replaced by the surface forces that act upon the incoming flow. Masson [23] used the actuator disc technique and a $k-\varepsilon$ type turbulence model to simulate a wind turbine operating in an uniform inflow and later extended this method to simulate a wind turbine rotor operating in an atmospheric boundary layer with different types of stratification [24].

The main assumption in ADM is that the forces are distributed evenly along the actuator disk. Hence, the influence of the blades is taken as an integrated quantity in the azimuthal direction. To overcome this limitation, a three-dimensional (3-D) N-S solver was combined with the so-called Actuator Line Technique (ALT) by Sørensen and Shen [25], in which the body forces were distributed along rotating lines representing the blades of the wind turbine.

The ALT allows for a detailed study of the dynamics of different wake structures, such as the tip and root vortices, using a reasonable number of grid nodes. Furthermore, the model benefits from being applicable to simple structured grids and therefore issues connected to grid generation do not occur. The drawback is that the method depends on the quality of the airfoil data [26].

Gonzalez and Munduate [27] performed aerodynamic analysis of parked and rotating configurations of the National Renewable Energy Laboratory (NREL) Phase VI wind turbine blade. They studied the mean values of the normal force coefficient and pressure coefficient in order to understand the physical mechanisms which govern the attached flow condition, the separation process and the onset of stall for a wind turbine blade planform with and without rotation. They found progressive delay from tip to root of the blade on the trailing edge separation process with respect to the two-dimensional (2-D) airfoil profile for the parked blade. They also found a local region of separated flow on the leading edge at 20% and 47% of the blade length. For the rotating blade, the strong radial flow resulted in dramatic suppression of the trailing edge separation at the inboard 30% and 47% stations of the wind turbine blade. They also found that the development of a leading edge separation structure was connected with the extra lift. They suggested a complex flow structure around the blade due to the serious augmentation of the blade normal force coefficient, which will require a further examination of the instantaneous pressure measurements in order to provide more insight into this phenomenon.

Schmitz et al. [28] used a coupled N-S/vortex-panel methodology to simulate the NREL Phase VI rotor under rotating and parked conditions. Good agreement was obtained with measured data for fully attached and stalled flows. For the rotating turbine under fully attached flow conditions, the effects of the vortex sheet dissipation and replacement by a rolled-up vortex on the computed normal force coefficient were investigated. The results revealed that rapid vortex sheet dissipation and roll-up led to a maximum of a 20% scatter in the computed rotor torque under zero yaw and attached flow conditions.

Ivanell et al. [29] used a three dimensional N-S LES solver combined with ALT for the simulation of the wake of the Tjæreborg wind turbine operating in an uniform inflow at four different tip speed ratios (TSRs). The promising LES technique successfully captured the strong unsteadiness of the wake field, while the high computational requirements of the technique were balanced by utilizing a “simple” ALT for calculating the blade loadings.

In the last decade, a consensus of opinion has been reached that aerodynamic modeling of a horizontal axis wind turbine (HAWT) by means of the semi-empirical methods (BEM type of models) has reached a point where no further improvement can be expected without a full understanding of the flow physics [30]. Consequently, there have been an increasing number of numerical studies to understand the HAWT aerodynamic features in recent years. These studies were conducted on many different levels, ranging from

BEM type of methods integrated with CFD calculations to full three-dimensional N-S models.

Sankar and colleagues [31]-[33] developed a hybrid N-S/full-potential/free wake method, mainly for predicting 3-D viscous flows over helicopter rotors and then extended it to the HAWT flow field. The computational domain was divided into three regions: N-S solution near the blades, potential flow representation on the outer field, and a collection of vortex methods for the vorticity field modeling. Later on they found that the full N-S simulations were better than the hybrid method in quality for all the properties studied: normal and tangential force distribution and surface pressure distributions [34]. They also found that at low wind speeds (less than about 7 m s^{-1}), even the algebraic turbulence model can yield good agreement with the experiment; at high wind speeds (15 m s^{-1} and 20 m s^{-1}) when the flow was partially separated, a combination of the Spalart-Allmaras (S-A) turbulence model and Eppler's transition model gave encouraging results. At intermediate wind speeds (7 m s^{-1} and 15 m s^{-1}), they suggested using a more sophisticated turbulence model with a finer resolution [35].

Full Reynolds Averaged Navier-Stokes (RANS) simulations of a wind turbine rotor were performed at the National Laboratory for Sustainable Energy (Risø) and the Technical University of Denmark (DTU). Several numerical investigations were carried out on a HAWT, using their in-house N-S solver EllipSys2D/3D and dealing with overall performance, loads, design of rotors and blade sections [25], [36], extreme operating conditions [37] and tip shape [38]. Among these investigations, Sørensen et al. [39]

performed simulations of several cases from the NREL wind tunnel tests using an incompressible finite volume solver EllipSys3D. Sectional forces and pressure distribution were calculated at varying wind speeds. After obtaining good agreement with the experimental results, they suggested that 3-D CFD can be used for wind turbine aerodynamic simulations.

The availability of experimental data from the NREL phase VI wind tunnel campaign motivated various researchers to test the performance of their CFD codes. The NREL phase VI wind turbine is a two-bladed, horizontal axis wind turbine. The blade is made up of an S809 airfoil.

Duque et al. [40] performed numerical computations on the NREL phase VI wind turbine. The numerical simulations were conducted by two CFD codes, CAMRAD II and OVERFLOW-D2. CAMRAD II is a lifting line code modified for wind turbine modeling which utilizes 2-D airfoil lift and drag data. OVERFLOW-D2 is a code which solves the compressible form of the RANS equations using an implicit finite difference approach with overset grids. Various stall delay models and dynamic stall models were implemented in the CAMRAD II code and the one-equation Baldwin-Barth model was implemented in the OVERFLOW-D2 code. Comparisons between the experimental data and computed aerodynamic loads showed that the OVERFLOW-D2 code can predict the stalled rotor performance, whereas the CAMRAD II code failed to capture the stalled rotor performance at the higher wind speeds.

Le Pape et al. [41] compared their results with the NREL Phase VI wind turbine experimental data at three wind speeds (7 m s^{-1}, 10 m s^{-1} and 20 m s^{-1}) using the ELSA compressible solver, developed by the French Aerospace Laboratory (ONERA) and the European Centre for Research and Advanced Training in Scientific Computation. The $k-\omega$ SST turbulence model was selected for turbulence closure. At 7 m s^{-1} wind speed, the agreement was good. However, at 10 m s^{-1} wind speed, there were discrepancies between the CFD predictions and the measurements and this was also the case for the 20 m s^{-1} wind speed computations. The thrust was well predicted, but the torque was under-predicted at 10 m s^{-1} and 20 m s^{-1} wind speeds. Later, Le Pape and Gleize [42] revisited the problem using a low-Mach number preconditioning technique on the ELSA solver and the $k-\omega$ SST turbulence model. The agreement at 7 m s^{-1} wind speed was still good and the numerical results at the 10 m s^{-1} wind speed were improved. However, at 20 m s^{-1} wind speed, the torque was still under-predicted.

Sezer-Uzol and Long [43] employed a 3-D, compressible, unsteady, inviscid finite volume flow solver, PUMA2, to simulate the NREL Phase VI wind turbine rotor for three selected cases. Comparisons of the sectional pressure coefficient distributions with experimental data showed good agreement. These investigations also observed considerable span-wise pressure variations, in addition to the chord-wise variations in all three cases. The authors suggested that 3-D time accurate CFD results can be used for the far-field noise predictions based on FW-H method.

Gomez et al. [44] performed unsteady compressible RANS simulation on an NREL tested wind turbine at zero degree yaw and 7 m s^{-1} wind speed using multi-block structured grids. Various root and tip configurations were compared and it was found that the blade aspect ratio and pitch angle had a primary role on the aerodynamic design of the turbine blade. The details of the root and tip shapes had a measureable effect within the resolution of CFD methods, although the overall power output was marginally affected by these changes. Gomez et al. also compared their results with the wind tunnel experimental data at three free stream velocities for the same rotor. Good agreement was shown for the surface pressure distributions at several stations along the blades as well as for the integrated thrust and torque. However, for moderately stalled flow conditions, some improvements were needed for the turbulence modeling to avoid over prediction of the wind turbine torque.

Carcangiu et al. [45] used a commercial CFD software package FLUENT® to perform the aerodynamic simulations of the NREL Phase VI wind turbine rotor. The steady flow field around an isolated rotor was predicted in a non-inertial reference frame, using both the S-A turbulence model and the $k-\omega$ SST model. Neither the tower nor the ground was included in the model, and a uniform wind speed profile was assumed at the entrance of the domain. The results of the computations on the turbine blade gave a good agreement with the experimental data.

CFD codes have also been used to study the blade tips in determining the performance of the wind turbine. Wang et al. [46] simulated a wind turbine blade with a tip vane

using the commercial software package FLUENT® and calculated the corresponding blade pressure distribution. They concluded that a blade with a tip vane resulted in a larger pressure difference between the suction and the pressure sides as compared to the usual blade configuration. Ferrer and Munduate [47] worked specifically on wind turbine blade tips. They analyzed the complex flow physics associated with the blade tips using a RANS CFD solver for three different wind turbine blade tip geometries. The effects of varying wind speeds and Reynolds number for different angles of attack of the blade tips were highlighted in their work. A considerable change in the pressure distributions depending on the blade tip geometries was noticed.

Despite the numerous reported investigations for isolated rotor cases, few authors have considered the wind-tunnel walls' influence on the CFD predictions. Wang and Coton [48] used a low-order panel method and a prescribed wake combined into a model capable of assessing the basic effect of wind-tunnel walls on wind turbine performance. This model was compared with wind-tunnel experiments results from Glasgow University [49], where Laser Sheet Visualization (LSV) and Particle Image Velocimetry (PIV) were used to study the wake structure of the wind turbine. Both experiments and calculations indicated the strong influence of the wind-tunnel walls on the wake structure. However, Simms et al. [50] used the method derived by Glauert [51] and adapted it for wind turbines to quantify the tunnel effects. After analyzing the data of the NREL Phase VI experiments, they estimated that the influence of the test section boundaries on the wake was smaller than 1% for most of the test conditions. Variations

in blade pitch were considered and the tunnel blockage was negligible for these experiments.

The first reported CFD study, where the effect of the walls was considered, was carried out by Sørensen et al. [39]. The wall effect was analyzed using an equivalent area as a computational domain (the square sectional area of the wind tunnel was modeled as circular). The wall boundary layer growth was not taken into consideration and a slip condition was applied at the far-field boundaries. The authors concluded that the tunnel blockage effect for the NREL Phase VI experimental cases was small.

Gómez-Iradi and Barakos [44] also considered the wind tunnel wall effect in their simulations of an isolated NREL Phase VI rotor at zero degree yaw and at a wind speed of 7 m s^{-1}. The unsteady compressible RANS simulation utilized a multi-block structured grid with a sliding mesh technique to deal with the interface of the moving and stationary domains. It was found that the wind tunnel walls had minimal influence on the mean pressure coefficient.

The effect of the blade-tower interaction is another key issue that must be taken into account when CFD results are compared against measurements. A few authors have studied the tower effect for a downwind wind turbine arrangement. A literature search showed that Duque et al. [52] performed the first CFD simulation on a NREL Phase II downwind arrangement wind turbine with a tower. Unsteady compressible thin layer

N-S solver was utilized with overset grids for the CFD simulation. The predictions of the rotor/tower interaction were not good due to the reported grid quality problems.

Zahle et al. [53] extended the incompressible solver EllipSys3D to include the use of overset grids and used it for computations of a downwind arrangement wind turbine. The numerical results were in reasonably good agreement with the experimental results capturing the unsteady interaction between the rotor and tower. However, the agreement with the experiment was less favorable at high wind speeds where large flow separations occurred. A different turbulence model and an appropriate transition model were recommended for improving the results at high wind speeds.

Gómez et al. [44] conducted a numerical simulation of the NREL Phase VI rotor with its tower in an upwind configuration. The unsteady compressible RANS method with multi-block grids was used for the simulations. The wind turbine torque agreed well with the experimental data. It was found that the presence of the tower reduced the rotor thrust and torque. It was also found that the tower effect increased with an increasing tower radius and a decreasing clearance distance between the wind turbine rotor and tower.

2.2 Review of Wind Turbine Aeroacoustic Simulations

In the wind turbine flow field research area, the models used can be classified into two broad categories: semi-empirical models and CFD based models. In a like manner, in the wind turbine noise prediction research area, the models employed can also be divided

into two broad categories: semi-empirical models and Computational Aero-Acoustics (CAA) based models.

Semi-empirical noise prediction models divide the wind turbine blade into segments and treat each of these segments as two-dimensional airfoil sections, each acting as an incoherent sound source [54]. The most common noise prediction models of this type are the Brooks, Pope and Marcolini (BPM) model [55], the TNO model [56], and the models proposed by Amiet [57] and by Lowson [58]. These noise prediction models are usually employed in conjunction with noise propagation models. Based on sound ray theory, these noise propagation models provide a set of semi-empirical formulae that account for various effects (e.g., air absorption, terrain, temperature gradients) on the sound propagation. Owing to their simplicity and ease of calculation, this set of semi-empirical methodologies for the wind turbine noise prediction is by far the most widely applied method for engineering applications (for both large modern and small-sized wind turbines). A number of references such as [7], [54], [59]-[66] describe the use and application of the semi-empirical method for wind turbine noise prediction.

Despite its high computational efficiency, semi-empirical noise prediction models do not include the interactions between the sources within the sound source zone because it treats each airfoil section along the blade as an incoherent sound source. Furthermore, semi-empirical noise prediction models are usually used with semi-empirical models for flow field prediction. The detailed unsteady flow field and sound source field

information cannot be obtained through these models for an accurate noise prediction for wind turbines.

Some researchers pair the semi-empirical based acoustic simulation models with the CFD based models for aeroacoustic predictions. Madsen et al. [67] conducted a study focusing on the prediction of low frequency noise for a 5 MW two-bladed turbine with a downwind rotor. This study applied CFD using a finite element method for discretization of the governing equations and used Lowson's [58] theory to relate the sound pressure level (SPL) to the Fourier coefficients for the unsteady aerodynamic forces on the blades. The results showed large variations of sound pressure level in time due to the wake unsteadiness, as well as a considerable increase in the sound pressure level if the blade passing frequency was close to the Strouhal (St) number controlling the vortex shedding from the tower. For an upwind-designed wind turbine, Madsen [68] used a similar method to predict the noise from a 3.6 MW Siemens three-bladed wind turbine and also identified several important turbine design parameters with influence on the low frequency noise. However, the drawback of this method was that for an upwind-designed wind turbine, it cannot take into consideration the effect of the tower on the blade surface forces.

Klug et al. [69] performed the noise prediction for 1 MW class HAWT using BEM theory for the aerodynamic calculation, the Farassat formulation 1A [70] for the discrete noise calculation and the Fukano approach [71]-[73] for broadband noise prediction. The results showed that the frequency band of the discrete noise lay in the infrasound

region with a maximum overall SPL (OASPL) of the discrete noise at about 70 dB; the broadband noise lay within the audible range with an OASPL of about 78 dB. However, the inaccuracy of the aerodynamic flow field calculation can affect the noise prediction results.

By using a more accurate aerodynamic flow field solver, Filios et al. [74] used the three-dimensional low-order panel method with a boundary-layer correction model and the impermeable FW-H formulation for the prediction of noise for the NREL Phase II downwind arranged wind turbine. In this study, relatively good predictive agreement was achieved for the aerodynamic data in spite of the fact that the simulation only included the wind turbine rotor. Furthermore, no acoustic measurements were presented for the validation of the noise predictions made in this study.

As the computational technology continues to advance, some physics-based computational models for both the aerodynamic and aeroacoustic calculations were applied for the wind turbine noise prediction.

Moroianu et al. [75] used a LES solver with an implicit subgrid-scale (SGS) model implemented in the commercial CFD software ANSYS® FLUENT® for the aerodynamic simulation of a three-bladed upwind wind turbine. The acoustic prediction was conducted using the FW-H acoustic analogy method. These investigations found that the acoustic field close to the wind turbine was dominated by the rotation frequency of the blades (blade passing frequency). In the far-field, the spectrum was influenced by the

ground. However, no experimental data was presented to validate their numerical results in this paper.

By using a less computationally demanding flow solver, Tadamasa and Zangeneh [76] conducted a RANS simulation for the noise produced by a wind turbine with the commercial CFD software ANSYS® CFX®. These simulations were conducted for a single blade of the NREL Phase VI two-bladed wind turbine. Both the permeable and impermeable FW-H formulations were employed for the noise calculations. The blade pressure results were shown to agree relatively well with some measurements, but the sound pressure level results were found to decrease smoothly over the whole spectrum of frequencies. This might be due to the time-averaging of the quantities implicit in the RANS model, which filtered out all the small fluctuations that were expected to contribute to the broadband noise.

In order to resolve the flow field surrounding the wind turbine blade, Arakawa et al. [77], [78] used a finer mesh and more computationally demanding flow field and acoustic field solvers for their investigations of two different blade tip shape designs on the noise generation. They used a compressible LES solver and a direct noise simulation for the acoustic prediction in the near-field region. The far-field noise prediction was modeled using the FW-H acoustic analogy methodology. They used this methodology to investigate the WINDMEL III wind turbine which is a two-bladed upwind wind turbine. Owing to the substantial number of grid points (300 million) and the very small time step (2.0×10^{-7} s) used, only one blade was simulated for a total blade rotation of 20.4

degrees. The simulation took 300 CPU hours on the Earth Simulator using 112 processors. The two tested blade tips (the actual wind turbine tip shape and the ogee type tip shape) did not exhibit any difference on the aerodynamic performance. However, the actual tip shape exhibited very high frequency pressure fluctuations which did not appear for the ogee type tip shape. The authors also found that at a distance of 20 m, the use of an ogee type tip shape can reduce the noise level by up to 5 dB at frequencies above 4 kHz.

Similarly, Zhu [79] also used computational demanding flow and acoustic solvers for the NREL 5 MW horizontal axis wind turbine noise prediction. The incompressible/compressible splitting method proposed by Hardin and Pope [80] was applied. The flow field prediction was obtained using the incompressible RANS methodology and the associated acoustic field was determined using the inviscid acoustic equations in the modified form proposed by Shen and Sørensen [81]. High-order spatial and temporal discretization schemes, dispersion-relation-preserving (DRP) and classical Runge-Kutta numerical techniques were employed to solve these acoustic equations. Owing to the tremendous number of grid points (320 million) and the very small time step (1.4×10^{-7} s) used, only one blade was simulated for a total blade rotation of 20.4 degrees in this study. The simulation was carried out using 112 processors and the authors reported that the simulations that they conducted had already reached the limits of the computational capabilities available to them.

Unfortunately, most of the currently available investigations using computational models did not include the wind turbine tower in their simulations, owing to the limited computational resources in these studies. Furthermore, these investigations also did not compare their numerical results with any wind turbine noise measurements. Finally, no noise predictions employing CAA based acoustic models from a full-sized wind turbine have been undertaken to date. The lack of available wind turbine noise data has severely limited the validation of the numerical predictions for the wind turbine noise.

2.3 Review of Acoustic Beamforming Research for Wind Turbine Noise Source Localization

Acoustic beamforming technique is generally an experimental method for NSI that has been applied to a wide range of objects including vehicles, household goods and wind turbines [82], [83]. Its application to wind turbine noise source identification has recently become a popular research area. However, due to the high cost of conducting an acoustic beamforming test, only a few researchers have conducted actual measurements for wind turbine noise source localization.

According to Renewable UK, wind turbines with a swept area up to 200 m^2 and rated power up to 50 kW are classified into micro- and small-sized wind turbines. Wind turbine with a swept area up to 1000 m^2 and a rated power in the range of 50-500 kW are categorized as a medium-sized wind turbine. The wind turbine with larger swept

areas and higher rated powers than medium-sized wind turbines are classified as large-sized wind turbines.

A few researchers conducted acoustic beamforming tests on modern large wind turbines. Buck et al. [84] conducted an acoustic beamforming test on a modified, two-bladed Westinghouse WWG-0600 wind turbine. This turbine has a hub height of 36.4 m and rotor radius of 21.3 m. This is an upwind arrangement wind turbine rated at 600 kW. A traditional frequency domain delay-and-sum (DAS) beamforming algorithm with diagonal elimination in the cross-spectral matrix was used for the signal processing. The acoustic beamforming algorithm included a simplified atmospheric model [85]-[87] which was utilized to compensate for the sound convection. The measuring microphone array consisted of 7 spiral arms each with 9 elements. The microphone array size was roughly 10 m × 10 m. The resulting acoustic maps indicated that noise surrounding the nacelle was the dominant noise source at the low-frequency range and as frequency increased, the blade tip on the downward passing path was observed to be the dominant aeroacoustic noise source.

Ramachandran et al. [88]-[90] examined five different acoustic beamformers when exposed to a single source, multiple incoherent and coherent sources and an oscillating source. The five different acoustic beamforming algorithms were:

1. Frequency domain beamforming (FDBF);
2. DAMAS2 (DMS2);

3. CLEAN-SC (CLSC);
4. Delay and Sum beamforming (DAS); and
5. TIDY.

The experiment employed a 0.72 m diameter microphone array consisting of 24 microphones. It was found that the FDBF, DMS2 and CLSC were limited to a narrowband analysis, whereas the DAS and TIDY could be used for broadband analysis. It was also found that CLSC was the best algorithm for narrowband analysis and that TIDY was the best for broadband analysis. These beamforming algorithms were then applied in a measurement of a General Electric (GE) 1.5 MW wind turbine. This wind turbine has a hub height of 85 m with a rotor diameter of 77 m. The wind turbine rotor has a variable rotor speed of 10.1 to 20.4 rpm. Good agreement with other test results ([63] and [91]) indicated that the compact and mobile microphone array (24 microphones with 0.72 m array diameter) in conjunction with an advanced beamforming algorithm was able to effectively separate both mechanical and aerodynamic noise sources. Furthermore, the authors claimed that this combination can also distinguish the yaw motor noise from the noise emitted by other mechanical components inside the nacelle.

More comprehensive measurements were conducted by Oerlemans et al. [63], [91]-[94] on two modern large wind turbines: a 850 kW GAMESA turbine with a rotor diameter of 58 m and a 2.3 MW GE turbine with a rotor diameter of 94 m. The microphone array used had an elliptical shape with 148 sensors and a size of 16 m × 18 m. The microphone array was placed on the ground at roughly one rotor diameter upwind from the turbine.

The acoustic maps showed that most of the noise was produced by the outer part of the blades during their downward movement. This source pattern which caused the typical swishing noise during the passage of the blades can be explained by trailing edge noise directivity and convective amplification [93]. Small noise production was also observed on both wind turbines when the blades passed the tower.

Since the experimental data suggested that trailing edge noise dominated the noise generation mechanism for modern large wind turbines, Oerlemans et al. [63] conducted a numerical simulation to compare with experimental data. A semi-empirical model for trailing edge noise based on the BPM model [55] was employed to provide the radial noise source distribution on the wind turbine blades. This radial source distribution was then extended with the effects of trailing edge noise directivity and convective amplification, as a function of the rotor azimuth and as perceived by an observer at a given position (microphone array). The calculated rotor noise source distribution was then imported to an array simulation code to yield the simulated acoustic source maps. It was shown that the numerical results agreed very well with the acoustic maps obtained from the experiments. The trailing edge noise directivity function was used to calculate the noise footprint of the wind turbine as a function of the rotor azimuth angle [63]. This footprint showed that the average sound level was lower in the cross-wind direction than in the upwind and downwind directions, but the variation in level was larger (up to 5 dB can be expected) in the cross-wind direction. Later on, a stall noise module was incorporated into the turbine noise model [95] to numerically investigate

the enhanced amplitude modulation (EAM) phenomenon. It was found that as long as the flow over the blade was attached, wind shear had practically no effect on the amplitude modulation. However, if local stall occurred, the resulting noise characteristics can be very similar to the EAM characteristics.

In addition, Oerlemans et al. [92] carried out a field acoustic beamforming measurement to examine the influence of different wind turbine blade designs on the turbine noise emission. The tested wind turbine is a GE 2.3 MW three-bladed wind turbine with one standard blade, one blade with trailing edge serrations and one blade with an optimized airfoil shape. The microphone array was placed at two different locations: one rotor diameter upwind and one rotor diameter downwind from the wind turbine. It was found that at low wind speeds, the downwind measurements exhibited less trailing edge noise reduction than the upwind measurements. It was also found that both modified blades showed a significant trailing edge noise reduction at low frequencies with an average overall noise reduction of 0.5 dB and 3.2 dB for optimized blade and serrated blade, respectively. However, the noise reduction increased for both modified blades with increasing wind speed. Furthermore, the modified blades also showed a noise increase at high frequencies during the upward part of the revolution.

In comparison with the research effort focused on modern large wind turbine noise, far fewer aeroacoustic investigations have been performed for medium- and small-sized wind turbines. Simley [96] designed two microphone arrays for an acoustic beamforming test on two different medium-sized wind turbines. Both wind turbines

have a rated power of 100 kW. One wind turbine, located at the National Wind Technology Center in Boulder, Colorado, has a hub height of 36.4 m and a rotor diameter of 21 m. The other wind turbine, located at the Agricultural Research Service sites in Bushland, Texas, has a hub height of 22.86 m and rotor diameter of 18 m with Blade System Design Study (BSDS) blades [97]. Two acoustic beamformers, the Robust Adaptive Beamforming (RABF) and Multiple Signal Classification (MUSIC), were employed for the signal processing. It was found that wind noise had negligible effect on the performance of the acoustic beamformers. The author suggested that longer test periods of the order of one minute were necessary to average out the atmospheric distortion. The acoustic map at 250 Hz indicated that an inboard blade noise exists between blade azimuth angles of 60 degrees and 120 degrees and again between 210 degrees and 240 degrees and near 0 degree as well. The acoustic map at 1.25 kHz showed that the trailing edge noise near the blade tip was between azimuth angles of 45 degrees and 210 degrees with peaks at 150 degrees and 180 degrees where the peak at 180 degrees was probably due to the unsteady loading from the tower. The author also suggested that the application of a more advanced beamforming algorithm would have improved the test results.

Cho et al. [11] performed acoustic beamforming measurements on a 12% scaled model of the NREL Phase VI wind turbine. The boundary layer transition dot was attached on the blade surface. The scaled wind turbine model was operated at a constant rotating speed of 600 rpm in order to have the same blade tip Mach number as the full scale

wind turbine. A 1 m-diameter microphone array with 144 sensors was placed on the wind tunnel floor. The resulting acoustic maps showed that at certain wind speeds, the position of the dominant noise source moved toward the blade tip as the frequency increased. At wind speeds below the stall wind speed, the noise spectra had similar trends. However, at wind speeds above the stall wind speed, the sound level of the low frequency noise increased.

The Microelectromechanical (MEMS) microphones were employed by Bale et al. [12], [13] to reduce the cost for conducting the acoustic beamforming measurements. Thirty top-ported Knowles Acoustics SPM0408HE5H microphones were assembled into an array on printed circuit boards. Conventional beamforming with diagonal removal using the algorithm reported in [98] was used for the data processing. The tested wind turbine is a three-bladed upwind wind turbine with a 1.3 m rotor diameter. The wind turbine has a 600 W rated power output at a rotating speed of 640 rpm. The test data revealed that at wind speeds of 4.5 m s^{-1} and 5.5 m s^{-1}, the acoustic spectra had a maximum of 12 dB (for 5.5 m s^{-1}) and 5 dB (for 4.5 m s^{-1}) increase over the background levels at frequencies above 3 kHz. The greatest sound pressure level was found to be roughly 120 degrees to 130 degrees in the azimuthal direction from the upward vertical direction. The authors suggested that the mechanism of this type of noise was due to blade trailing edge noise.

Chapter 3

Computational Acoustic Beamforming Method

The computational acoustic beamforming method is described in detail in this chapter. The framework of the CAB method is described in Section 3.1, with a detailed description of the three components that comprise the CAB method provided in Sections 3.2-3.4.

3.1 Computational Acoustic Beamforming Framework

The computational acoustic beamforming method is a numerical method for noise source identification. The CAB method consists of three components: namely, the CFD, acoustic propagation and acoustic beamforming components. The CFD component is used to simulate the unsteady flow field containing the sound sources; the acoustic propagation component is used to simulate the sound propagation and calculate the acoustic signals at specified locations (e.g., microphone locations); and, the acoustic beamforming component is used to generate the acoustic maps using the predicted acoustic (microphone) signals.

A hybrid method is used in the CAB methodology for the simulation of the flow-generated noise. This approach decouples the flow simulations (CFD component) from the acoustic calculations (acoustic propagation component). Aerodynamic properties obtained from the CFD simulation can be used as inputs to the acoustic calculations.

However, any changes in the noise simulation will not affect the flow field calculations. In this way, the same set of data (sound source information) obtained from the CFD simulation can be used for different arrangements of the receivers. The CFD simulation is the most computationally intensive component of the CAB methodology and, as a result, the use of a hybrid method increases the computational efficiency significantly. This is due to the fact that the CAB methodology can be applied to various cases using different microphone arrangements or different microphone array locations without having to redo the CFD calculations. However, the use of this hybrid method in the CAB methodology limits its principal application to flows at low Mach numbers (weakly compressible flows) [99].

In greater detail, Figure 3.1 depicts the various components of the CAB methodology. The transient CFD simulation calculates the flow properties (pressure, velocity, density, etc.) at discretized mesh points in the computational domain. The computational domain contains the sound source data acquisition surfaces required for the acoustic propagation calculation. The flow properties obtained on the acoustic acquisition surfaces are utilized by the acoustic propagation solver to calculate the sound signals at the specified microphone (receiver) locations. The acoustic beamforming component utilizes these calculated acoustic signals to generate the acoustic maps at a prescribed source plane. The resulting acoustic maps embody the information on the sound source locations as seen from the microphone array for a specified range of frequencies or for a specified set of octave bands. In this way, the CAB methodology utilizes the virtual

microphone signals, which are computationally generated from the information provided by the CFD and acoustic propagation components, for the acoustic beamforming calculation. This is in contrast to conventional acoustic beamforming which employs the microphone signals measured in an actual experiment.

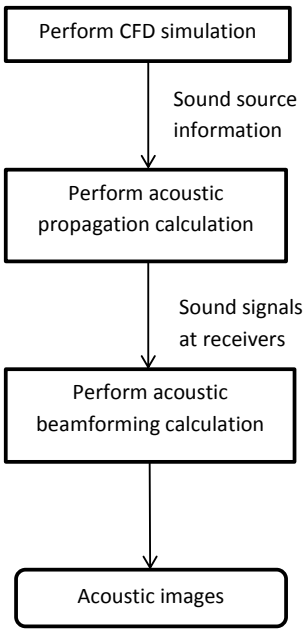

Figure 3.1: Flow chart of the CAB method.

3.2 CFD Component

The CFD component involves conducting the CFD simulations to determine the flow field quantities that embody the sound source information, such as the flow velocity, density and pressure. The CFD simulations are conducted using a commercial CFD package, namely STAR CCM+®.

Different CFD methodology and turbulence models were used for the validation and application cases in this thesis. Section 3.2.1 describes the CFD governing equations and Section 3.2.2 introduces the turbulence models used in the validation and application cases.

3.2.1 CFD Governing Equations

The governing equations for three dimensional, unsteady and compressible Newtonian fluid are the conservation laws of mass, momentum, and energy as shown below. The following assumptions were made:

1. The external forces (gravity and electromagnetic) are neglected;
2. The volume viscosity is zero because all the test cases investigated are in the low-Mach number flow region; and
3. The dynamic viscosity μ is a constant.

The mass conservation equation (also known as the continuity equation) is

$$\frac{\partial \rho}{\partial t} + \frac{\partial}{\partial x_j}(\rho u_j) = 0. \quad (3.1)$$

The momentum conservation equation is

$$\frac{\partial}{\partial t}(\rho u_i) + \frac{\partial}{\partial x_j}(\rho u_i u_j) = -\frac{\partial}{\partial x_i} p + \frac{\partial \sigma_{ij}}{\partial x_j}. \quad (3.2)$$

The energy conservation equation is

$$\frac{\partial}{\partial t}(\rho e_0) + \frac{\partial}{\partial x_j}(\rho u_j e_0) = -\frac{\partial}{\partial x_j}(u_j p) - \frac{\partial}{\partial x_j}(q_j) + \frac{\partial}{\partial x_j}(u_i \sigma_{ij}), \quad (3.3)$$

where σ_{ij} is the viscous stress tensor having the following expression:

$$\sigma_{ij} = 2\mu\left(S_{ij} - \frac{1}{3}\frac{\partial u_k}{\partial x_k}\delta_{ij}\right). \quad (3.4)$$

The rate of strain tensor S_{ij} is defined as

$$S_{ij} = \frac{1}{2}\left(\frac{\partial u_i}{\partial x_j} + \frac{\partial u_j}{\partial x_i}\right). \quad (3.5)$$

In Eq. (3.3), e_0 is the total energy, and $\boldsymbol{q}$ is the heat flux vector. By Fourier's law, the heat flux can be expressed as

$$q_i = -c_k \frac{\partial T}{\partial x_i}, \quad (3.6)$$

where c_k is the thermal conductivity which is treated as a constant.

The ideal gas law is

$$p = \rho R_{specific} T, \quad (3.7)$$

where $R_{specific}$, the specific gas constant, is used for the equation of state in order to close the system of governing equations (Eqs. (3.1)-(3.3)).

When the governing equations (Eqs. (3.1)-(3.3)) are solved in the moving reference frame, the fluid velocities can be transformed from the stationary frame to the rotating frame using

$$v_{r_i} = \omega_i \times r, \tag{3.8}$$

and

$$u_i = u_{r_i} + v_{r_i}, \tag{3.9}$$

where u_{r_i} is the relative velocity, u_i is the absolute velocity and v_{r_i} is the rotational velocity. Substituting Eqs. (3.8) and (3.9) into the governing equations Eqs. (3.1)-(3.3) transforms these equations into the rotational reference frame:

$$\frac{\partial \rho}{\partial t} + \frac{\partial}{\partial x_j}\left(\rho u_{r_j}\right) = 0, \tag{3.10}$$

$$\frac{\partial}{\partial t}\left(\rho u_{r_i}\right) + \frac{\partial}{\partial x_j}\left(\rho u_{r_i} u_{r_j}\right) + \rho\left(2\omega_i \times u_{r_i} + \omega_i \times \omega_i \times r_i\right) = -\frac{\partial}{\partial x_i} p + \frac{\partial \sigma_{r_{ij}}}{\partial x_j}, \tag{3.11}$$

and

$$\frac{\partial}{\partial t}(\rho e_{0_r}) + \frac{\partial}{\partial x_j}\left(\rho u_{r_j} e_{0_r}\right) = -\frac{\partial}{\partial x_j}\left(u_{r_j} p\right) - \frac{\partial}{\partial x_j}(q_j) + \frac{\partial}{\partial x_j}\left(u_{r_i}\sigma_{r_{ij}}\right). \quad (3.12)$$

The additional terms shown in the momentum equation Eq. (3.11) indicate the acceleration of the fluid due to the rotational reference frame. The first and second terms in the third bracket on the left hand side of the Eq. (3.11) represent the Coriolis acceleration and centripetal acceleration, respectively.

This set of equations Eqs. (3.10)-(3.12) are applied when there are rotational moving regions in the computational domain and the multiple reference frame (MRF) method is used. Flow around the moving part is modeled with a steady-state approximation with respect to the moving reference frame. Because the MRF method does not take into account of the relative motion between the moving zone and its adjacent zones, the grid remains fixed during the simulation and the solution provides a snapshot of the flow regime.

To capture the transient effect in the flow with the moving parts, Eqs. (3.1)-(3.3) are resolved on the moving mesh using a sliding mesh technique. For wind turbine flow field application, the mesh inside the moving zone rotates with the wind turbine blades and slides along the interface between the rotating and stationary zones. No mesh regeneration is needed at each time step, but the nodes may not align requiring an interpolation at the interface as a result. In consequence, the rotating interface is normally required to be placed away from the wind turbine blades in order to avoid any

inaccuracies in the determination of the flow field near the turbine due to this interpolation.

3.2.2 Turbulence Closure Methodology

3.2.2.1 RANS Methodology

The Reynolds averaging is the most popular method for dealing with turbulent flows. It provides information on the overall mean flow properties. The idea behind Reynolds averaging is Reynolds decomposition, whereby an instantaneous quantity $\phi(x,t)$ can be decomposed into its time-averaged and fluctuating components as given by

$$\phi(x,t) = \Phi(x) + \phi'(x,t), \tag{3.13}$$

where the average quantity $\Phi(x)$ is defined by

$$\Phi(x) = \overline{\overline{\phi(x,t)}} = \lim_{\tau\to\infty} \frac{1}{\tau} \int_{t}^{t+\tau} \phi(x,t)dt. \tag{3.14}$$

If the average flow varies slowly with time when compared to the integral time scale of the turbulent fluctuations, the definition given in Eq. (3.14) can be replaced by

$$\Phi(x,t) = \overline{\overline{\phi(x,t)}} = \frac{1}{\tau} \int_{t}^{t+\vartheta} \phi(x,t)dt. \tag{3.15}$$

Note that the average of the fluctuating component is zero. For engineering applications, it is assumed that ϑ is much greater than the time scale of the turbulent fluctuations.

Applying the Reynolds average on the governing equations (Eqs. (3.1)-(3.3)) gives the compressible Reynolds-averaged Navier-Stokes equations (also termed the Favre-averaged Navier-Stokes equations) [100]-[102]:

$$\frac{\partial \bar{\bar{\rho}}}{\partial t} + \frac{\partial}{\partial x_j}\left(\bar{\bar{\rho}}\hat{u}_j\right) = 0; \tag{3.16}$$

$$\frac{\partial}{\partial t}\left(\bar{\bar{\rho}}\hat{u}_i\right) + \frac{\partial}{\partial x_j}\left(\bar{\bar{\rho}}\hat{u}_i\hat{u}_j\right) = -\frac{\partial}{\partial x_i}\bar{\bar{p}} + \frac{\partial \bar{\bar{\sigma}}_{ij}}{\partial x_j} + \frac{\partial \tau_{ij}}{\partial x_j}; \tag{3.17}$$

and

$$\begin{aligned}\frac{\partial}{\partial t}\left(\bar{\bar{\rho}}\hat{e}_0\right) + \frac{\partial}{\partial x_j}\left(\bar{\bar{\rho}}\hat{u}_j\left(\hat{e}_0 + \frac{\bar{\bar{p}}}{\bar{\bar{\rho}}}\right)\right) \\ = \frac{\partial}{\partial x_j}\left(\bar{\bar{\sigma}}_{ij}\hat{u}_i + \overline{\overline{\sigma_{ij}u_i^{"}}}\right) \\ - \frac{\partial}{\partial x_j}\left(\bar{\bar{q}}_j + c_p\overline{\overline{\rho u_j^{"}T^{"}}} - \hat{u}_i\tau_{ij} + \frac{1}{2}\overline{\overline{\rho u_i^{"}u_i^{"}u_j^{"}}}\right),\end{aligned} \tag{3.18}$$

where c_p is the heat capacity at constant pressure and $\bar{\bar{\sigma}}_{ij}$ is given by

$$\bar{\bar{\sigma}}_{ij} \approx 2\mu\left(\hat{S}_{ij} - \frac{1}{3}\frac{\partial \hat{u}_k}{\partial x_k}\delta_{ij}\right). \tag{3.19}$$

The dynamic viscosity μ is assumed as a constant in the current work owing to the small temperature changes in the validation cases [103].

The double overbar in Eqs. (3.16)-(3.18) indicates a conventional time-average. The averaging time is assumed to be long compared to the integral time scale of the turbulent fluctuations and short compared to unsteadiness in the mean flow. The hat in Eqs. (3.16)-(3.18) represents the Favre (density-weighted) average which can be expressed in the following format:

$$\hat{\phi} = \frac{\overline{\overline{\rho\phi}}}{\bar{\bar{\rho}}}. \tag{3.20}$$

Note that

$$\phi = \bar{\bar{\phi}} + \phi' = \hat{\phi} + \phi''. \tag{3.21}$$

The equation of state has the following expression:

$$\bar{\bar{p}} = (\gamma - 1)\left[\bar{\bar{\rho}}\hat{e}_0 - \frac{1}{2}\bar{\bar{\rho}}(\hat{u}^2 + \hat{v}^2 + \hat{w}^2) - \bar{\bar{\rho}}k\right], \tag{3.22}$$

where γ is the heat capacity ratio and k is the local turbulent kinetic energy which is given by

$$k = \frac{[(\widehat{u_i^{"}})^2 + (\widehat{v_i^{"}})^2 + (\widehat{w_i^{"}})^2]}{2}. \quad (3.23)$$

In the Favre-averaged equations (Eqs. (3.16)-(3.18)), the terms τ_{ij}, $c_p\overline{\overline{\rho u_j^{"} T^{"}}}$, $\overline{\overline{\sigma_{ij} u_i^{"}}}$, and $\frac{1}{2}\overline{\overline{\rho u_i^{"} u_i^{"} u_j^{"}}}$ need to be modeled. However, most turbulence modeling focuses on the Reynolds stress term $\tau_{ij} \equiv -\overline{\overline{\rho u_i^{"} u_j^{"}}}$. The most common solution to model the Reynolds stress term is Boussinesq's eddy viscosity concept, which assumes, in analogy to the viscous stresses in laminar flows, that the turbulent stresses are proportional to the mean velocity gradient in the form of

$$\tau_{ij} = 2\hat{\mu}_t \left(\hat{S}_{ij} - \frac{1}{3}\frac{\partial \hat{u}_k}{\partial x_k}\delta_{ij}\right), \quad (3.24)$$

where $\hat{\mu}_t$ is the turbulence eddy viscosity. For incompressible flow, the second term in parentheses in Eq. (3.24) vanishes.

Various models have been proposed to solve the turbulence eddy viscosity based on the Boussinesq approximation. These turbulence models can be classified into following four categories:

1. Algebraic (zero-equation) models;
2. One-equation models;
3. Two-equation models; and
4. Second-order closure models.

Among them, two-equation models are the commonly used such as the well-known eddy viscosity models. Three types of two-equation models are introduced in this section: namely, $k-\varepsilon$ two-layer, RNG $k-\varepsilon$ and $k-\omega$ SST turbulence models. The transport equations and the model coefficients are summarized in Appendix I.

The $k-\varepsilon$ two-layer approach was proposed by Rodi [104] to improve the near-wall behavior of the standard $k-\varepsilon$ turbulence model [105], [106]. This approach combined the standard $k-\varepsilon$ model (high Reynolds number turbulence closure) in the outer layer and the one equation model (low Reynolds number turbulence closure) in the near wall region. Several variants of the near wall model have been proposed. In the current work, we will use the Wolfshtein [107] one equation model for the near wall approximation.

The RNG $k-\varepsilon$ model was derived by Yakhot et al. [108] from the instantaneous Navier-Stokes equations using renormalization group theory. The main difference between the standard $k-\varepsilon$ turbulence model and RNG $k-\varepsilon$ turbulence model is the additional term R_ε added to the dissipation rate transport equation which attempts to account for the different scales of motion through changes to the production term.

The $k-\omega$ SST turbulence model was introduced by Menter [109] to deal with the strong freestream sensitivity of the $k-\omega$ turbulence model and to improve the predictions of adverse pressure gradients. It applies the $k-\omega$ turbulence model in the inner region of the boundary layer and uses the $k-\varepsilon$ turbulence models in the free shear flow.

3.2.2.2 LES Methodology

The large eddy simulation (LES) method is receiving increasing attention for high Reynolds number turbulent flows simulation. According to the local isotropy hypothesis of Kolmogorov [110], small scales of the flow are supposed to be more universal and less determined by the boundary conditions than the large ones. This can also be shown in the energy spectrum plot of Figure 3.2 where ϖ represents the wavenumber $\varpi = \frac{2\pi}{\lambda}$ and $E(\varpi)$ indicates the energy level as a function of wavenumber. In LES, the large eddies of the flow (corresponding to large wavelength or small wavenumber) which are dependent on the geometry are resolved explicitly in a transient calculation, whereas the small scales of the flow which are more universal are modeled by using a subgrid-scale model through a spatial filtering process.

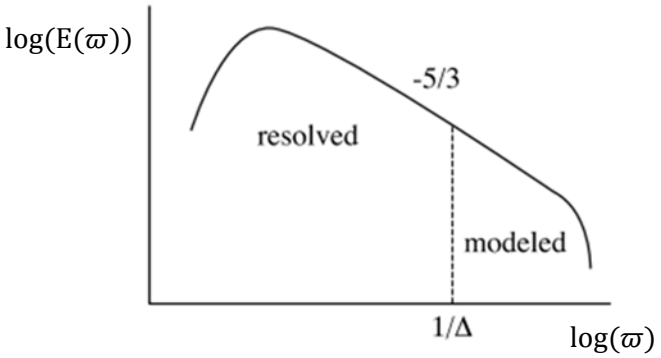

Figure 3.2: Kolomogorov's 5/3 law [111].

The essential idea of LES is the scale separation which separates the flow variables into resolved and unresolved parts [112]. The resolved parts which are represented by eddies large enough to be accurately captured on the grid are explicitly computed in a

transient calculation. The unresolved parts which are represented by small eddies that cannot be resolved on the computational grid are modeled using subgrid-scale models. Most of the subgrid–scale models are based on the Boussinesq approximation to calculate the subgrid-scale quantities using the resolved quantities. The scale separation is achieved by a filtering process which is represented mathematically in physical space as a convolution product of cut-off scales in space and time [113].

The Favre filtering is a common filtering process used in the LES method. The resultant filtered equations look identical to the Favre-averaged unsteady RANS equations (Eqs. (3.16)-(3.18)) which is beneficial in the framework of a RANS/LES coupling computation. However, the turbulent stress tensor, as shown in Eq. (3.19), now represents the subgrid-scale stresses. The turbulence viscosity μ_t in Eq. (3.19) now represents the subgrid-scale turbulent viscosity. The subgrid-scale stresses and subgrid-scale turbulent viscosity are calculated by a subgrid-scale model.

The Smagorinsky subgrid-scale model [114] was used in LES simulations of the NACA 0012 airfoil case in this thesis. Based on the Boussinesq approximation, the Smagorinsky subgrid-scale model provides the following mixing-length type formula for the calculation of subgrid-scale viscosity:

$$\mu_t = \rho \Delta^2 S, \qquad (3.25)$$

where Δ is a length scale which is defined as

$$\Delta = f_v \min\left(\kappa d, C_s V^{\frac{1}{3}}\right), \tag{3.26}$$

where V is the cell volume and d is the wall distance and κ is the Von Karman constant $\kappa = 0.41$. The coefficient C_s has the value of 0.05. f_v is the Van Driest damping function computed as follows [115], [116]:

$$f_v = 1 - \exp\left(-\frac{y^+}{A}\right). \tag{3.27}$$

The damping coefficient A has the default value of 25. The dimensionless wall distance y^+ is defined as

$$y^+ = \frac{u^* d}{\nu}, \tag{3.28}$$

where u^* is the friction velocity computed from the instantaneous wall shear stress at the nearest wall face and ν is the kinematic viscosity.

3.2.2.3 DDES Methodology

Detached-eddy simulation (DES) was first proposed in 1997 and first used in 1999 [117]. The initial motivation was to create a methodology to address the challenge of massively separated flows at high Reynolds numbers. The concept of the DES is to use the LES methodology (resolved turbulence) in the outer region and the RANS methodology in the near-wall region. In this way, the hybrid RANS/LES methodology

combines the computational efficiency of RANS for modeling the flow in the near-wall regions of a solid surface with the predictive accuracy of LES for simulating the large-scale turbulent flow structures in regions away from a solid surface.

However, for the wall bounded flows with thick boundary layers and small separation regions, the grid spacing parallel to the wall is usually fine enough for DES to activate the LES branch. But in reality, the grid near the wall region is not fine enough to capture all the velocity fluctuations. Moreover, the eddy viscosity will be reduced as well as the modeled Reynolds stress, without the introduction of resolved stresses to restore the balance. This phenomena is called modeled stress depletion (MSD) [118]. A consequence of MSD is the grid-induced separation (GIS) which causes early separation in the DES solution [119].

To resolve the MSD and GIS issues in DES, Menter and Kuntz [120] proposed a solution called shielding, in which the DES limiter is disabled as long as the flow is recognized as a boundary layer. Similarly, Spalart et al. [121] introduced a blending function given by Eq. (3.29) below in DES to ensure that the transition from RANS to LES is independent of grid spacing. This improved version of DES is called delayed-detached eddy simulation (DDES).

The characteristic length scale $\tilde{d}$ in DDES is defined by

$$\tilde{d} = d - f_d \max(0, d - C_{DES}\Lambda), \qquad (3.29)$$

where d is the distance to the wall and Λ is the maximum computational cell dimension in the x-, y- and z- directions. The empirical constant C_{DES} in Eq. (3.29) has a value of 0.65. f_d takes the form of

$$f_d = 1 - \tanh[(8r_d)^3], \qquad r_d = \frac{\nu_t + \nu}{\left(\frac{\partial \hat{u}_i}{\partial x_j}\frac{\partial \hat{u}_i}{\partial x_j}\right)^{1/2} \kappa^2 d^2}, \tag{3.30}$$

where υ and υ_t are the molecular and turbulent kinematic viscosities, respectively.

The one-equation Spalart-Allmaras (S-A) turbulence model [118] is used with the DDES methodology. The transport equation and the model coefficients are listed in Appendix II.

3.2.2.4 Wall Treatment

The most reliable way to resolve the thin near-wall sublayer is to use a fine grid and a low-Reynolds number turbulence model. However, this can be very computationally expensive especially for the 3-D calculations. The traditional industrial solution is to use wall functions to model the near wall region where viscous effects become important.

For the coarse mesh adopted in most of the industrial applications, the standard wall function is applied when the centroid of the wall adjacent cell lies within the log-law region of the boundary layer. Within this log-law region,

$$\frac{u}{u^*} = \frac{1}{\kappa}\ln E\left(\frac{\rho u^* d}{\mu}\right), \tag{3.31}$$

where u is the velocity parallel to the wall and the model constant $E = 9.793$.

Since the standard wall function assumes that the near-wall node lies in the fully-turbulent log-law region, if the near-wall node lies in the viscous sublayer, the use of this wall function will result in deterioration in the solution accuracy. Furthermore, when the near-wall flows are subjected to severe pressure gradients or in strong non-equilibrium, the solution from the standard wall function is likely not to be reliable.

In order to have a near-wall model which possesses the accuracy for standard wall-function mesh while at the same time not reducing the accuracy for fine near-wall mesh, an all y^+ wall treatment was used. In the region near the wall, the normalized streamwise velocity profile in the viscous and turbulent boundary layer is given by ($u^+ \stackrel{\text{def}}{=} U/u^*$)

$$u^+ = \frac{1}{\kappa}\ln(1+\kappa y^+) + C\left[1 - \exp\left(-\frac{y^+}{D}\right) - \frac{y^+}{D}\exp(-\mathrm{b}y^+)\right], \tag{3.32}$$

where

$$y^+ \stackrel{\text{def}}{=} u^* d/\nu\,, \qquad D = y_m^+, \tag{3.33}$$

$$C = \frac{1}{\kappa}\ln\left(\frac{E'}{\kappa}\right), \qquad b = \frac{1}{2}\left(\frac{D\kappa}{C} + \frac{1}{D}\right),$$

$$E' = \frac{E}{\xi}, \qquad E = 9.0.$$

Here, y_m^+ is the point where the viscous sublayer intersects the log-law layer. This point is determined using Newtonian iteration. ξ is the roughness function which modifies the log-law coefficient E [122]. This formulation for the wall treatment uses Reichardt's law [123] for the calculation of the source term in the discretization of the momentum transport equation at the wall cells. For a coarse mesh where the mesh point closest to the wall lies in the region $y^+ \geq 30$, the term in the square brackets in Eq. (3.32) tends to unity and Eq. (3.32) in this case reduces to the standard logarithmic law of the wall (referred to as the high y^+ wall treatment). Alternatively, for a fine mesh where the mesh point closest to the wall lies in the region $y^+ \approx 1$, Eq. (3.32) resolves the properties of the flow all the way down to the wall (referred to as the low y^+ wall treatment). When y^+ falls within the buffer layer, this method provides more realistic predictions of the flow than either the low y^+ or the high y^+ wall treatments.

3.3 Acoustic Propagation Component

The sound source information provided by the CFD component is used by the acoustic propagation component to calculate the sound signals at a set of prescribed locations for the microphone. The acoustic propagation component was conducted using an in-

house code that implements the FW-H integral method [124] for computational aeroacoustics.

The original FW-H formulation utilized generalized functions to recast the continuity and momentum transport equations into the form of an inhomogeneous wave equation. This formulation includes the effects of very general types of surfaces and motions in the turbulent flow field for the generation of noise. To realize the advantages of the FW-H equation, an integral formulation of the equation can be obtained by convolving the FW-H partial differential equation with the free-space Green's function.

In this section, three FW-H integral formulations, namely, the permeable formulation, the impermeable formulation and the impermeable formulation for static sources, which are used in the validation cases in this thesis, are explained below.

The most general form of the FW-H integral formulation is the permeable formulation which has the following form:

$$p'(\boldsymbol{x},t) = p'_T(\boldsymbol{x},t) + p'_L(\boldsymbol{x},t), \tag{3.34}$$

where

(3.35)

$$4\pi p_T'(\boldsymbol{x},t) = \int_{f=0}\left[\frac{\rho_0\left(\dot{U}_n + U_{\dot{n}}\right)}{r(1-M_r)^2}\right]_{ret} dS + \int_{f=0}\left[\frac{\rho_0 U_n\left(r\dot{M}_r + c(M_r - M^2)\right)}{r^2(1-M_r)^3}\right]_{ret} dS,$$

and

(3.36)

$$4\pi p_L'(\boldsymbol{x},t) = \frac{1}{c}\int_{f=0}\left[\frac{\dot{L}_r}{r(1-M_r)^2}\right]_{ret} dS + \int_{f=0}\left[\frac{L_r - L_M}{r^2(1-M_r)^2}\right]_{ret} dS + \frac{1}{c}\int_{f=0}\left[\frac{L_r\left(r\dot{M}_r + c(M_r - M^2)\right)}{r^2(1-M_r)^3}\right]_{ret} dS.$$

Here,

(3.37)

$$L_r = L_i r_i, \quad L_M = L_i M_i, \quad U_n = U_i n_i, \qquad U_{\dot{n}} = U_i \dot{n}_i, \quad M_r = M_i r_i,$$

(3.38)

$$U_i = \left(1 - \frac{\rho}{\rho_0}\right)v_i + \frac{\rho u_i}{\rho_0}, \qquad M_i = \frac{v_i}{c}, \qquad L_i = p'\delta_{ij}n_j + \rho u_i(u_n - v_n),$$

where n_i is the i-th component of the unit outward vector normal to the integration surface and $f = 0$ represents the surfaces surrounding the permeable domain of the

computational domain. The descriptor “permeable” used in relation to this equation refers to the fact that the surface can be placed outside the solid body, allowing the fluid to flow through it. Furthermore, r_i is the i-th component of the unit radial vector $\frac{(\boldsymbol{x}-\boldsymbol{y})}{r}$ where $(\boldsymbol{x},t)$ and $(\boldsymbol{y},\tau)$ are the receptor and source space-time variables, respectively. The i-th component of the velocity v at the points on the integration surface is denoted by v_i, and u_i is the i-th component of the velocity u at points in the local fluid. The i-th component of Mach number of a point on the boundary surface is denoted by $M_i = \frac{v_i}{c}$; v_n is the local normal velocity of the integration surface; and, u_n is the local fluid velocity in the direction normal to the boundary surface. The dots over the quantities denote temporal derivatives with respect to the source time τ. The subscript ret indicates that the quantity is evaluated at the retarded time $\tau = t - r/c$, and the subscripts T and L denote the thicknessand loading noise, respectively.

When the permeable integration surface coincides with the solid surface, the body and fluid velocities are related by $u = v$ and the impermeable formulation of the FW-H equation is obtained. Eqs. (3.34)-(3.36) reduce to the following simpler form:

$$p'(\boldsymbol{x},t) = p'_T(\boldsymbol{x},t) + p'_L(\boldsymbol{x},t), \qquad (3.39)$$

where

$$4\pi p_T'(\boldsymbol{x},t) = \int_{f=0}\left[\frac{\rho_0(\dot{v}_n + v_{\dot{n}})}{r(1-M_r)^2}\right]_{ret} dS + \int_{f=0}\left[\frac{\rho_0 v_n\left(r\dot{M}_r + c(M_r - M^2)\right)}{r^2(1-M_r)^3}\right]_{ret} dS, \quad (3.40)$$

and

$$4\pi p_L'(\boldsymbol{x},t) = \frac{1}{c}\int_{f=0}\left[\frac{\dot{L}_r}{r(1-M_r)^2}\right]_{ret} dS + \int_{f=0}\left[\frac{L_r - L_M}{r^2(1-M_r)^2}\right]_{ret} dS + \frac{1}{c}\int_{f=0}\left[\frac{L_r\left(r\dot{M}_r + c(M_r - M^2)\right)}{r^2(1-M_r)^3}\right]_{ret} dS. \quad (3.41)$$

For wind turbine noise calculation, both the permeable and impermeable formulations of the FW-H equation were used to evaluate the SPL spectra at the far-field receivers. To use the permeable FW-H formulation, the integration surface is chosen to enclose the wind turbine rotor and part of the hub. The sound source data such as velocity and pressure, as well as the mesh data are stored on the permeable integration surface during the CFD simulation and subsequently imported into the FW-H acoustic solver to calculate the signals at the microphones. To use the impermeable FW-H formulation, the integration surface is chosen to coincide with the blade surface and rotates with the

blade. At each time step, the sound source data, mesh data as well as the turbine blade surface coordinates need to be stored on the impermeable integration surface and imported subsequently into the FW-H acoustic solver for the sound calculation. The impermeable FW-H acoustic calculation requires more storage space compared with the permeable FW-H acoustic calculation for the wind turbine acoustic calculation.

By further assuming a static sound source, where the relation $u = v = 0$ can be used to simplify the impermeable formulation, Eqs. (3.39)-(3.41) reduce to

$$4\pi p_L'(\boldsymbol{x}, t) = \int_{f=0} [\frac{\dot{p} cos\theta}{cr}]_{ret} dS + \int_{f=0} [\frac{p cos\theta}{r^2}]_{ret} dS. \quad (3.42)$$

Here p is the gauge pressure and θ is the local angle between the normal to the surface and the radial direction $\boldsymbol{r}$ at the emission time, $cos\theta = n_i r_i$.

The above equation shows the dipole type of noise resulting from the uneven loading forces on the stationary solid body [125]. This formulation has been used in validation cases of flow over the tandem cylinders case and flow over the NACA 0012 airfoil case.

Two schemes were used for approximation of the time derivative terms in all three formulations of the FW-H equation. They are the central differencing scheme (CDS) and Stirling scheme [126]. The numerical formulations of these two schemes are shown below:

$$\dot{p}_{ret} = \left[\frac{p_{\tau+1} - p_{\tau-1}}{2\tau}\right], \tag{3.43}$$

$$\dot{p}_{ret} = \left[\frac{p_{\tau+1} - p_{\tau-1}}{2\tau}\right] + \frac{\Delta\tau}{\tau}[p_{\tau+1} - 2p_{\tau} + p_{\tau-1}] + \frac{[3\Delta\tau^2 - 1][p_{\tau+1} - 3p_{\tau} + 3p_{\tau-1} - p_{\tau-2}]}{12\tau}. \tag{3.44}$$

The influence of these two schemes on the sound spectra and acoustic maps is compared for the WINPhase 10 wind turbine and NACA 0012 airfoil trailing edge noise cases.

3.4 Acoustic Beamforming Component

The acoustic beamforming calculation takes the sound signals calculated by the acoustic propagation component to generate the acoustic maps for the identification of the possible sound sources. Different acoustic beamforming algorithms are implemented in the in-house acoustic beamforming code and two microphone array geometries are used for the WINPhase 10 wind turbine and NACA 0012 airfoil trailing edge noise cases.

3.4.1 Acoustic Beamforming Algorithm

The work reported herein uses the time domain DAS beamformer for the acoustic beamforming calculation in the CAB method. The principle behind DAS beamforming is the constructive and destructive interference of sound waves. It uses time of arrival (TOA) to either amplify or attenuate the signals. Figure 3.3 shows a simple schematic

figure of the DAS beamformer. The TOA describes the time taken for a wave front to reach each microphone. Assuming a specific angle of incidence for the plane wave, the TOA is different for each microphone in the array. The DAS beamformer will delay the signals to compensate for the differences in the TOA at each microphone. When these signals are summed, the resultant total signal gives a constructive interference of the plane wave from the microphone array. On the other hand, the signals from the directions other than the given angle of incidence will result in destructive interference.

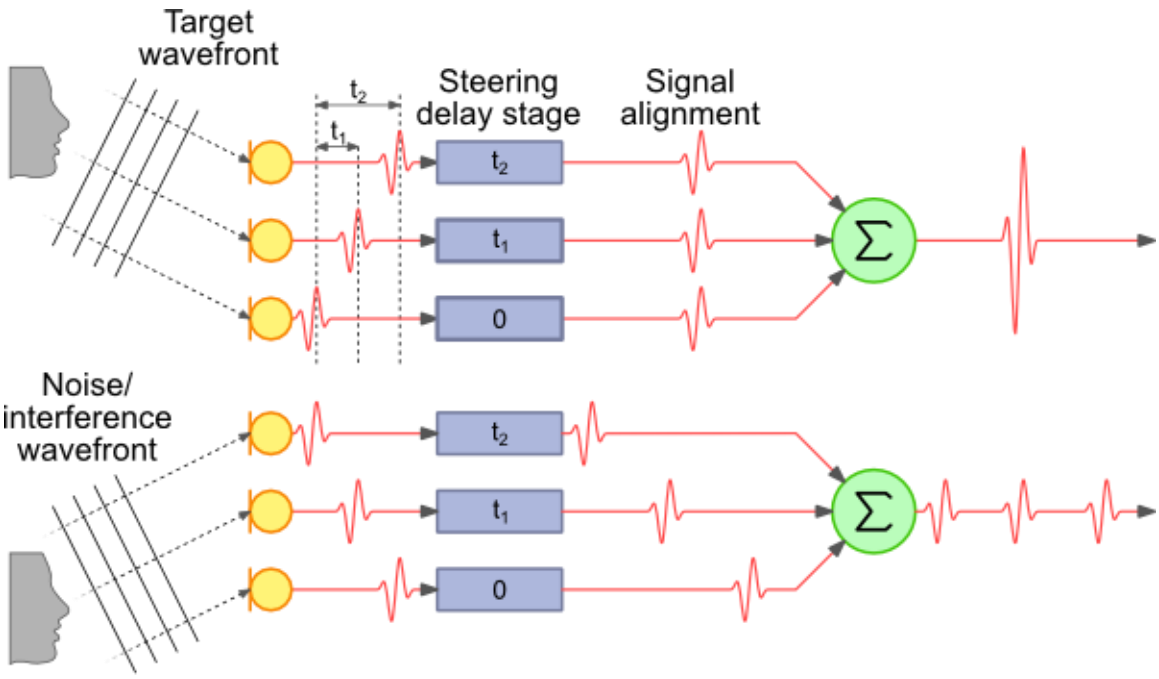

Figure 3.3: A schematic sketch of delay-and-sum beamforming algorithm [127].

3.4.1.1 DAS Beamformer for Plane Wave Incidence

Consider a planar array of M microphones at locations $\vec{r}_m$ ($m = 1,2,\dots,M$). For convenience, we place the array phase center at the origin and it is assumed that a

plane wave approaches the microphone array from direction $\boldsymbol{\psi}$ as shown in Figure 3.4 (a). The time-domain DAS beamformer output is given by,

$$\frac{1}{M}\sum_{m=0}^{M-1}\vec{r}_m = \vec{0}, \tag{3.45}$$

$$b(\boldsymbol{\psi}, t) = \sum_{m=1}^{M} w_m p_m(t - \Delta_m) \tag{3.46}$$

where w_m is the weighting or shading coefficient for each microphone's signal (uniform weight is used in this thesis), p_m is the measured pressure signals at each microphone, Δ_m is the time delay at each microphone for a select direction characterized by a unit vector $\boldsymbol{\psi}$**.** This time delay is determined as

$$\Delta_m = \frac{\boldsymbol{\psi} \cdot \boldsymbol{r_m}}{c}, \tag{3.47}$$

where c is the speed of sound. As the direction unit vector $\boldsymbol{\psi}$ changes, the time delay for each microphone will be different. The objective is to apply these time delays to each microphone for a given direction $\boldsymbol{\psi}$ and then sum up the individual signals from each microphone. The results exhibit the directional sensitivity of the microphone array as shown in Figure 3.4 (b) which clearly shows a main lobe in the focused direction and weaker side lobes in the other directions. It is seen that a small maximum side-lobe level (MSL) is essential for a good acoustic beamformer and array design.

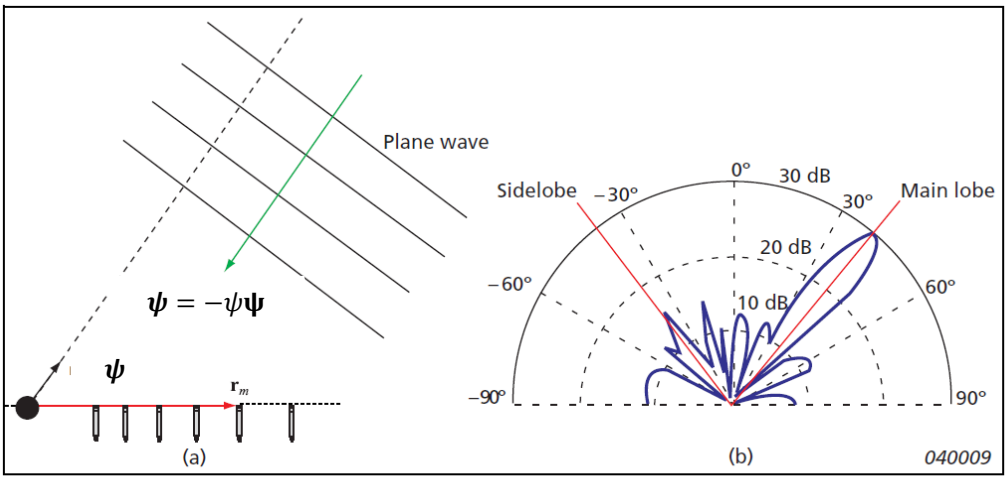

Figure 3.4: (a) A plane wave incident from the focus direction to a microphone array and (b) the directional sensitivity of the array [128].

3.4.1.2 DAS Beamformer for Spherical Wave Incidence

Eqs. (3.46) and (3.47) are employed when the incident wave is a plane wave or when the microphone array is placed in the far field of the sound radiation where the plane wave assumption is satisfied. If the incident wave is spherical or the microphone array is placed in the near and/or transition regions of the sound source, Eqs. (3.46) and (3.47) cannot be used for the beamforming. In this case, it is necessary to use an acoustic beamformer for spherical wave incidence described as follows:

$$b(t) = \sum_{m=1}^{M} w_m p_m\left(t - \Delta_{mspherical}\right), \qquad (3.48)$$

where the time delay for spherical wave incidence $\Delta_{mspherical}$ is given by

$$\Delta_{mspherical} = \frac{s - s_m}{c}, \tag{3.49}$$

where s is the distance between the assumed source and the microphone array center and s_m is the distance between the assumed source and the microphone m. The spherical wave incidence formulation utilizes the actual wave travel distance to calculate the time delays for each microphone, whereas the plane wave incidence formulation uses the steering direction to calculate the time delays among the microphones.

3.4.1.3 Diagonal Removal Technique for DAS Beamformer

The diagonal removal technique, which is widely used to improve the signal-to-noise ratio (SNR) for large microphone arrays mounted on wind tunnel wall surfaces (e.g., for the removal of turbulent boundary layer wall-pressure fluctuations) [129]-[134] has been implemented in our in-house acoustic beamforming code. The DAS beamformer with diagonal removal is given by

$$\mathrm{b}(\vartheta_i) = \left\langle \left[\sum_{m=1}^{M} p_m(t - \Delta_{im}) \right]^2 + \sum_{m=1}^{M} p_m^2(t - \Delta_{im}) \right\rangle, \tag{3.50}$$

where ϑ_i represents grid point i at the source plane, Δ_{im} is the propagation time from source plane grid point i to microphone m, for plane wave incidence, Δ_{im} is given by Eq. (3.47); For spherical wave incidence, Δ_{im} is given by Eq. (3.49). Here $\langle \quad \rangle$ indicates a time averaging operation.

The inclusion of the diagonal removal technique can substantially improve the appearance of the acoustic maps, but sometimes it also causes problems. Researchers reported that when focusing on a spatially extended sound source, the use of the diagonal removal technique yielded unreliable peak levels on the resultant acoustic maps [16], [17]. Moreover, they also reported that the employment of the diagonal removal caused negative array output power at some points on the acoustic maps when steering away from the sound sources. In addition, researchers also reported that the use of the diagonal removal technique did not improve the dynamic range for the acoustic maps at a frequency of 2 kHz, although a considerable improvement was observed at a frequency of 8 kHz [18].

In this thesis, the diagonal removal technique was included as an option in the acoustic beamforming code. This option was used for simple cases such as the monopole sound source validation case. This option was also used for the NACA 0012 trailing edge noise validation case in order to quantify the influence of the diagonal removal technique on the resultant acoustic maps. However, the diagonal removal technique was not used for the more complicated small wind turbine noise case.

3.4.2 Microphone Arrays

Microphone arrays used for acoustic beamforming measurement can be classified into two categories: regular arrays and irregular arrays.

Examples of regular array are the one dimensional uniform line array (a linear array with equidistant microphone spacing) and the two dimensional grid and cross arrays shown in Figure 3.5. The major limitation of regular arrays is the spatial aliasing which is introduced by the repeated sample spacing. This aliasing creates false sources on the source plane also known as ghost images.

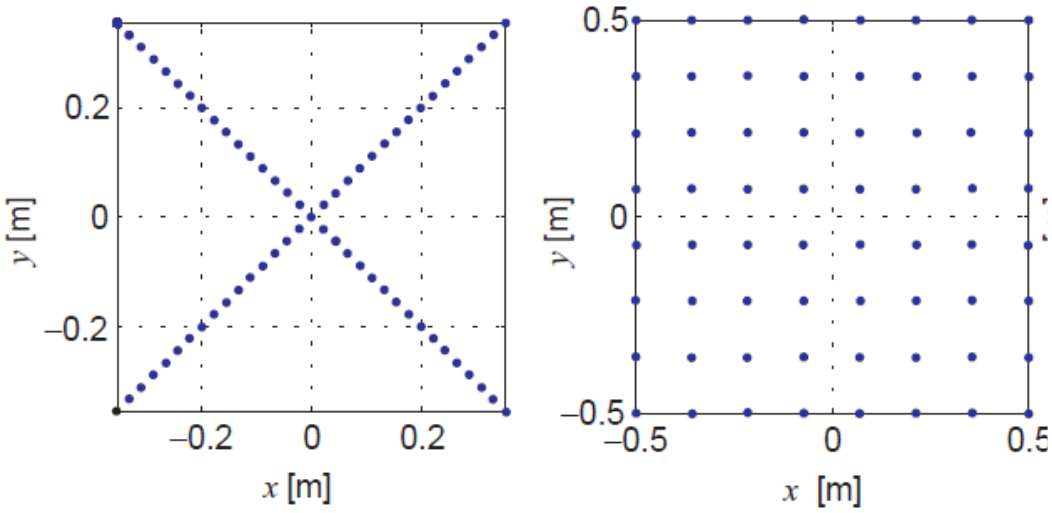

Figure 3.5: Regular microphone array examples: cross array (left) and grid array (right) [128].

One way to avoid the spatial aliasing is to change the array pattern to be non-redundant [128]. A non-redundant array is an array such that the vector between any two microphone positions on the array is always different. Non-redundant arrays usually have irregular or random geometry.

Generally speaking, irregular array designs outperform regular array designs. However, the array geometric parameters to the array MSL exhibit highly erratic behavior during

the microphone array design stage. Furthermore, different beamforming algorithms also respond differently to different array designs.

This thesis uses two irregular microphone arrays for validation and application of the CAB method. These are the Archimedean spiral array and the star array as shown in Figure 3.6. The Archimedean spiral array has 66 microphones and the microphone position coordinates are described by

$$\begin{cases} x(\varphi) = \dfrac{\alpha\varphi}{2\pi}\cos(\varphi) \\ y(\varphi) = \dfrac{\alpha\varphi}{2\pi}\sin(\varphi) \end{cases} \tag{3.51}$$

with $\alpha = 0.2$. Here, φ varies from 0 to 2π. The star array has 63 microphones arranged along 7 arms with 9 microphones per arm. The inside and outside diameters for the star array are 0.25 m and 1.5 m as shown in Figure 3.6. The sizes of these two arrays were changed in order to match the array dimensions used in the experiment, whereas the patterns and the number of microphones were kept the same.

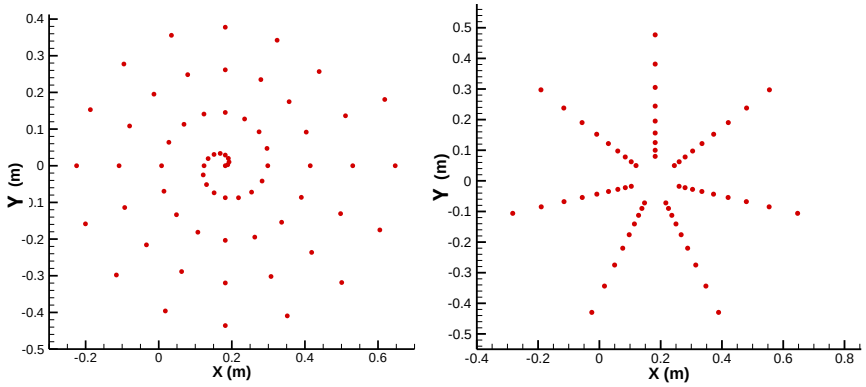

Figure 3.6: Two irregular microphone arrays used in this thesis: Archimedean spiral array (left) and star array (right).

Chapter 4

Validation of the Computational Acoustic Beamforming Method—Component Level

This chapter presents five test cases in order to validate each of the three components comprising the CAB method. The validation cases for the CFD, acoustic propagation and acoustic beamforming components are presented in Sections 4.1, 4.2 and 4.3, respectively.

The validation of the CFD component for the wind turbine flow field simulation is described in Section 4.1. The CFD solver used to simulate the flow field of the wind turbine is applied to two small HAWTs: the Fortis Montana and the WINPhase 10. The wind tunnel experimental data for the Fortis Montana wind turbine and the field measurement data for the WINPhase 10 wind turbine were compared with the numerical results in terms of the power output from the wind turbines. Good agreement was obtained between the numerical results and the test data which implied that the CFD methodology used herein is capable of predicting the wind turbine aerodynamic forces accurately.

The validation of the acoustic propagation component is documented in Section 4.2. Three formulations of the FW-H equation were examined using two different validation cases. The case of the flow over two circular cylinders in tandem was used to validate

the impermeable formulation of FW-H equation for a static sound source. The WINPhase 10 wind turbine case was used to validate both the impermeable and the permeable formulations of the FW-H equation. The numerical predictions agreed well with the wind tunnel data from the tandem cylinders case and the field measurement data from the wind turbine case. These results provide confirmation that the predictions of the SPL at the receiver locations using the FW-H acoustic code are correct.

The validation of the acoustic beamforming component is described in Section 4.3 for a case involving a single frequency sound source. Both near-field and far-field beamformers, as well as the diagonal removal technique, were validated using this test case. Good agreement was realized with the theory and some experimental results, providing confidence that the acoustic maps generated by the acoustic beamformer are correct.

4.1 CFD Component Validation for Wind Turbine Flow Field Simulation

A literature search suggested employing a DDES type of model in conjunction with the S-A turbulence closure scheme for the wind turbine aerodynamic simulation [35], [135]. This numerical framework was used for the flow field simulations associated with the two small HAWTs.

4.1.1 Fortis Montana Wind Turbine Validation Case

The Fortis Montana is a 5.8 kW permanent magnet small horizontal axis wind turbine. The wind turbine rotor has a diameter of 5.03 m and a swept area of 19.87 m^2. The approximate exposed area of the hub and mast was 0.18 m^2 during the experimental testing. The blade chord at 75% of the blade length was 0.2135 m. The experimental testing of the Fortis Montana 5.8 kW wind turbine was conducted at the 9 m × 9 m National Research Council Canada wind tunnel. The forces acting on the wind turbine were measured using a mass balance methodology. The details of the experiment settings can be found in [136].

4.1.1.1 Geometry and Mesh

The computational domain consists of two sub-domains: (a) the cylindrical rotating sub-domain surrounding the rotor and (b) the rectangular stationary sub-domain representing the external flow as shown in Figure 4.1. The length of the computational domain extends from $1D$ (D is the rotor diameter) upwind to $3D$ downwind of the wind turbine. The computational domain dimension is $2.5D \times 2.5D \times 4D$.

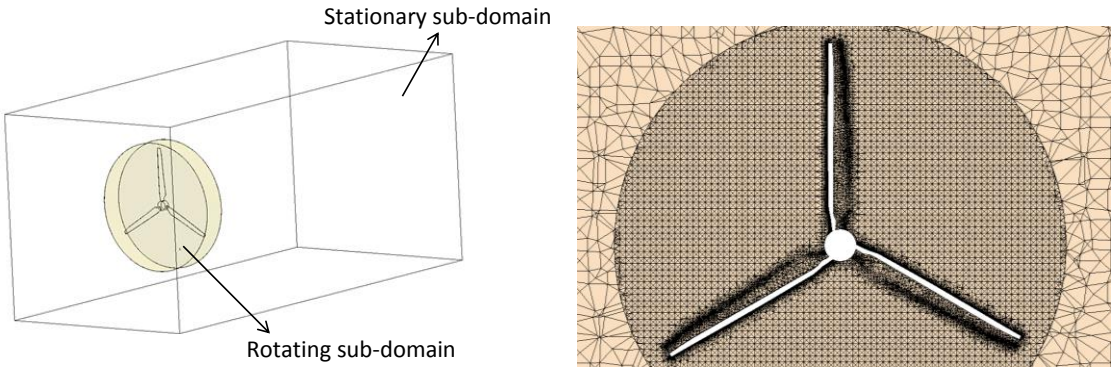

Figure 4.1: Fortis Montana wind turbine computational domain (left) and tetrahedral mesh used for CFD simulation (right).

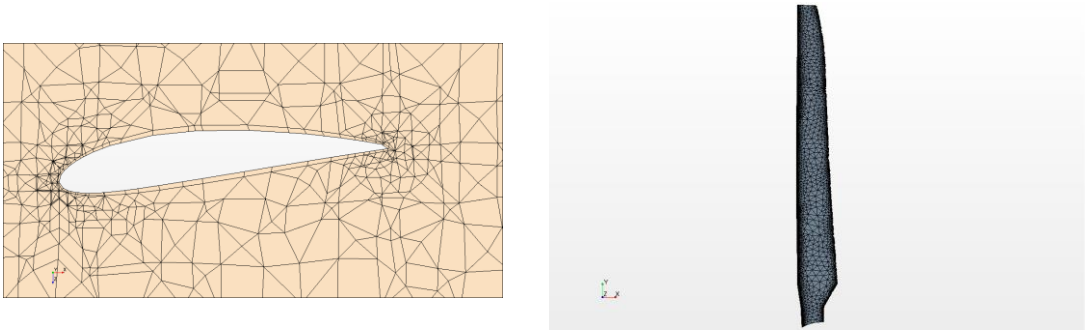

(a) (b)

Figure 4.2: Tetrahedral mesh used surrounding the Fortis Montana wind turbine blade.

An unstructured grid consisting of 1.31 million tetrahedral cells were clustered around the rotor and hub in the rotating sub-domain. A total of 1.48 million tetrahedral cells for whole computational domain (comprising the rotating and stationary sub-domains) was created with ANSYS® DesignModeler®. One layer of prismatic cells was generated surrounding the blade as shown in Figure 4.2 (a), having cell centroids with normalized wall-normal distances y^+ in the range of 30 to 200. Figure 4.2 (b) displays the computational mesh used to represent the blade. A higher-resolution grid was

generated surrounding the turbine blade in the vicinity of both the blade leading edge and trailing edge. Due to the limitation of computational resources available to the author, the computational grid shown here representing the turbine rotor in the rotating sub-domain and the surrounding air flow of the wind tunnel in the stationary sub-domain constituted a relatively coarse-grid representation for the problem.

4.1.1.2 CFD Settings and Boundary Conditions

The simulations of the flow field were undertaken using ANSYS® Fluent® 13.0. A pressure-based solver was used for the incompressible flow calculation. The simulation employed DDES computational strategies with the one-equation S-A turbulence model.

The three-dimensional unsteady N-S equations were solved using a cell-centered finite volume method. A least-squares cell-based scheme was chosen for the gradient approximation of all quantities used in the discretization of the governing equations. A first-order upwind scheme was used to approximate the convective term in the modified turbulence viscosity transport equation in the S-A model. A bounded central differencing scheme was used in DDES for discretization of the convective term in the momentum transport equation. All the diffusion terms in the transport equations were discretized using a central differencing scheme. A pressure-weighted interpolation scheme was used to estimate the pressure values at the cell faces from their values at the cell centroids. A second-order implicit scheme was chosen for the time marching algorithm with a maximum of 50 iterations permitted for each time step. A fixed time step of 0.0001 s was chosen to keep the average Courant-Friedrichs-Lewy (CFL) number

within the computational domain below a value of 2. The iterative scheme used here to enforce mass conservation through the pressure-velocity coupling was the Semi-Implicit Method for Pressure-Linked Equations (SIMPLE).

A uniform (nominal) mean velocity $U_\infty = 7\ \mathrm{m\ s^{-1}}$ was prescribed at the inlet of the computational domain. For the specification of the turbulence at the inlet boundary, the turbulence intensity and the dissipation length scale for turbulence were prescribed according to the experimental data and the mixing-length assumption. The pressure at the outlet boundaries of the domain was set to atmospheric pressure. The wind turbine blade surfaces were treated as no-slip smooth walls.

4.1.1.3 Flow Field Results and Analysis

Figure 4.3 exhibits the predicted power coefficient c_{Power} obtained from DDES calculation in comparison with that obtained from the wind tunnel measurements for various values of TSRs. The definitions of TSR and power coefficient are

$$\mathrm{TSR} = \frac{\omega_{WT} R}{v_{wind}}, \tag{4.1}$$

and

$$c_{Power} = \frac{P_{WT}}{\frac{1}{2}\rho A_{WT} {v_{wind}}^3}, \tag{4.2}$$

where ω_{WT} is the wind turbine rotor rotational speed in radians per second, R and A_{WT} are the rotor radius and swept area of the wind turbine respectively, v_{wind} is the incoming wind speed and P_{WT} is the power generated by the wind turbine.

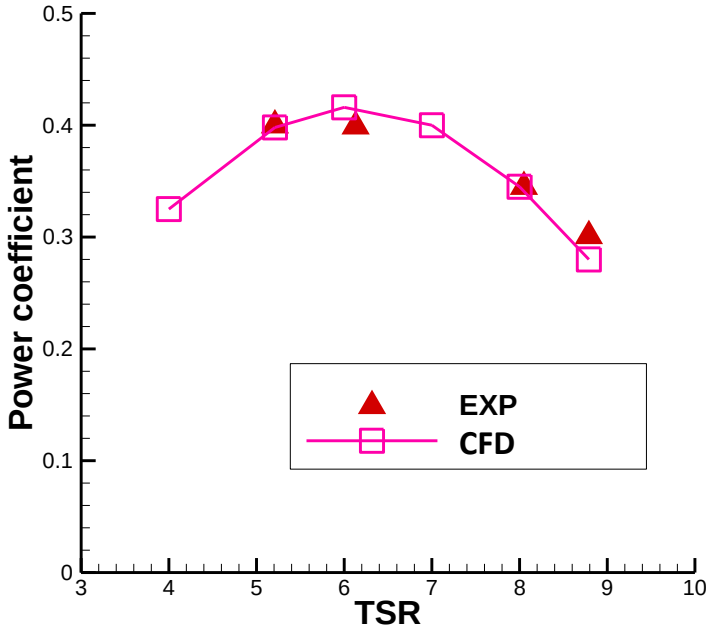

Figure 4.3: Fortis Montana wind turbine power comparison.

The predicted c_{Power} provided by the DDES simulations agreed very well with the wind tunnel experimental data. Note that the numerical results slightly over-predicted c_{Power} at TSR = 6, whereas it slightly under-predicted c_{Power} at TSR = 8.79.

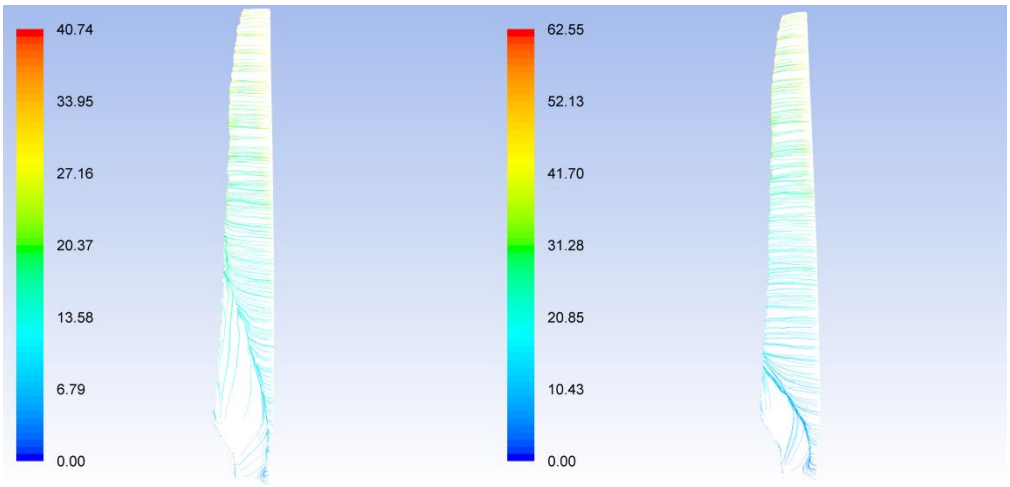

Figure 4.4: Blade oil flow pathlines at TSR = 5.21 (left) and TSR = 7 (right).

Figure 4.4 displays blade oil flow pathlines for different TSR values using DDES method. The color legend for the plots of the flow pathlines encodes the magnitude of the absolute velocity (in m s^{-1}). At TSR = 5.21, the AOA at the blade root area was relatively high in comparison with the blade tip area. This resulted in the flow separation around the blade root area as shown in the left plot in Figure 4.4. As the TSR increased to a value of 7, the AOA began to decrease and the resulting aerodynamics was associated with a more pronounced attached flow field surrounding the blade, leading to a smaller separation zone in the root area of the blade as shown in the right plot in Figure 4.4. However, as shown in Figure 4.3, the predicted wind power gave similar values at these two TSR values because the separation zone is located close to the blade root area where the increasing size of the separation zone does not play a significant role in the wind turbine power output. On the other hand, with further increases in the TSR (e.g., at TSR = 8.79), the AOA decreases and the lift generated by the blade decreases as a

consequence, resulting in a reduced power output from the wind turbine as seen in Figure 4.3.

Strictly speaking, the computational mesh used for the DDES simulations in this study is still too coarse to provide a true scale-resolving turbulent fluid flow simulation around the wind turbine. However, despite this limitation, the accuracy in characterization of the aerodynamic performance of a wind turbine using a coarse resolution DDES simulation methodology appears to provide a sufficient accuracy and a relatively low computational burden that it can be used in routine industrial and engineering applications. For future work, the use of a finer mesh together with the sliding mesh methodology and various DDES turbulence models will need to be investigated in order to support the conclusions drawn herein based on the present preliminary coarse-grid calculations.

4.1.2 WINPhase 10 Wind Turbine Validation Case

The WINPhase 10 wind turbine is a small commercial three-bladed horizontal axis wind turbine with an upwind arrangement. The WINPhase 10 wind turbine has a rated power of 10 kW at a rotor speed of 150 rpm and incoming wind speed of 11 m s^{-1}. The diameter of the rotor for this small wind turbine is 10 m and the height of the tower is 20 m. The field measurements of the wind turbine power output were conducted by the wind turbine manufacturer and the measurement data were obtained from the manufacturer WINPhase Energy Inc. (pers. comm.).

4.1.2.1 Geometry and Mesh

The wind turbine blade geometry was obtained from the wind turbine manufacturer. The rest of the wind turbine geometry (the hub and tower) was generated using the commercial CFD software package STAR CCM+® v9.0. The mesh generation and the flow simulation were also undertaken using the software STAR CCM+®.

Figure 4.5 shows the computational domain used for the aerodynamic simulation of the full size WINPhase 10 wind turbine. This configuration included three sub-domains, namely, a permeable sub-domain, a rotating sub-domain and a stationary sub-domain. The permeable sub-domain included the rotor and rotates with the rotating sub-domain at the same speed. The rotating sub-domain was placed away from the wind turbine blades to avoid the inaccuracies in the determination of the flow field near the turbine due to the interpolation at the interface between the rotating and stationary domains when using the sliding mesh technique. A smaller sub-domain (namely, the permeable sub-domain) was generated close to the wind turbine rotor for the sound source data acquisition. This strategy allowed a relatively fine resolution of the flow within the integration surface.

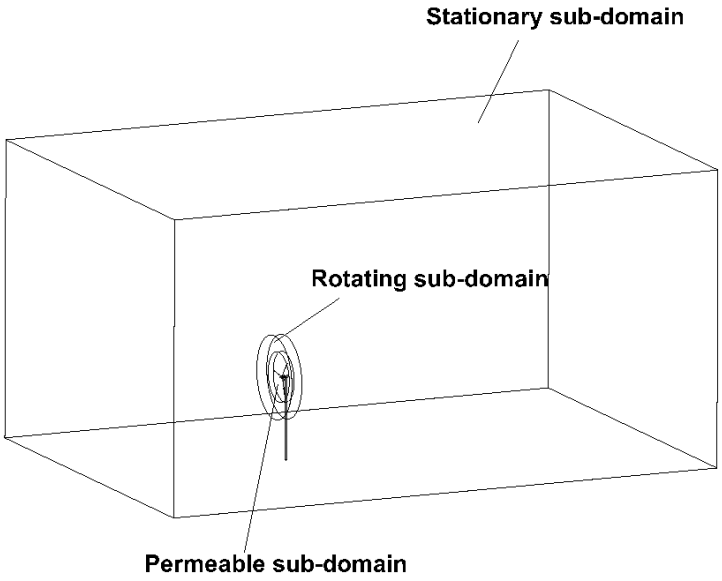

Figure 4.5: Computational domain for WINPhase 10 wind turbine CFD simulation. The computational domain consists of a rotating sub-domain, a permeable sub-domain, and a stationary sub-domain.

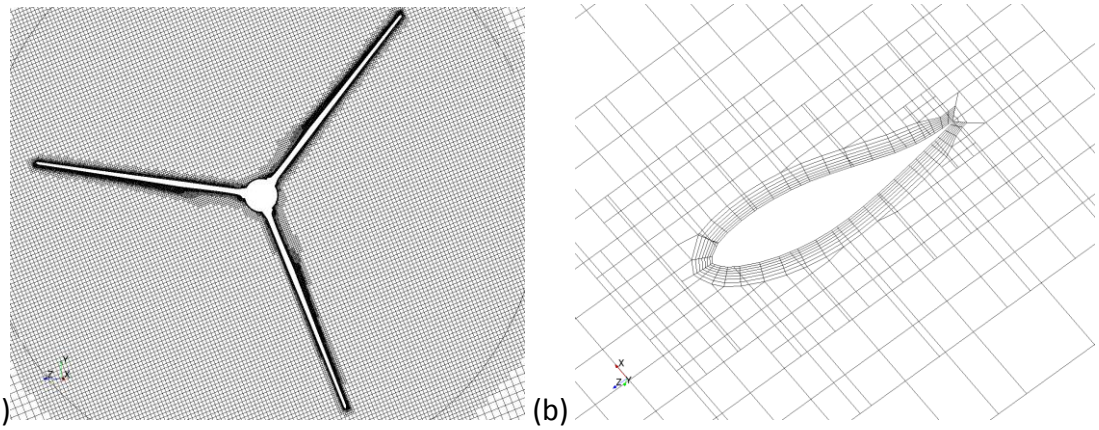

Figure 4.6: Depiction of the mesh in the computational domain: (a) front view of the blades and (b) region surrounding a turbine blade.

The computational domain had dimensions of $14D$ along the wind direction with $4.5D$ upstream of the wind turbine and $9.5D$ downstream of the wind turbine, $9.6D$ in the

crosswind direction and $7D$ from the base of the wind turbine tower to the top of the computational domain. Seven prism layers were applied around the blade as shown in Figure 4.6. The mesh consists of more than 1.6 million cells inside the permeable sub-domain and a total of 4.34 million cells in the whole computational domain.

4.1.2.2 CFD Settings and Boundary Conditions

The CFD settings were the same as summarized for the Fortis Montana wind turbine validation case. The boundary conditions were different. A set of reference wind speeds in the range from 9 m s^{-1} to 11 m s^{-1} with a one-seventh power-law dependence on height above the ground surface was used to prescribe the wind speed profile at the computational domain inlet. More specifically, the one-seventh power-law wind speed profile has the following form:

$$\frac{v_{wind}}{v_{ref}} = (\frac{y_{WT}}{y_{ref}})^{1/7}, \quad (4.3)$$

where v_{ref} and y_{ref} represent the reference velocity and reference height, respectively. In the WINPhase 10 wind turbine simulations, the reference height was chosen as the wind turbine hub height (viz., $y_{ref} = 20\ m$). A fix time step of 0.0001 s is applied for all the simulations. The turbulence viscosity ratio was set to a value of 10 at the inlet boundary for all simulations. The pressure at the domain outlet boundary was set to the atmospheric pressure. The surfaces of the wind turbine rotor and tower were treated as no-slip smooth walls.

4.1.2.3 Flow Field Results and Analysis

Figure 4.7 compares the power curves obtained from the numerical simulation with corresponding experimental data for a range of TSR values. It is noted that the experimental data used for comparison here were obtained from full-scale wind turbine field measurements, rather than from a well-controlled wind-tunnel study. The error bars shown in Figure 4.7 only reflect the uncertainty of the generator efficiency. Other sources of uncertainty such as the inflow turbulence and the terrain conditions were very difficult to quantify in the current set of experimental data. Considering the numerical simulations were performed in an idealized environment with fewer disturbances than were presented in the actual field measurements, it is expected that the power prediction from our simulations should be higher than the power measured in the field experiments where numerous environmental factors would have resulted in power losses. Hence, in view of this consideration, the DDES results, which sat at the upper limit of the field test data range, give a reasonable prediction of the power output of this wind turbine.

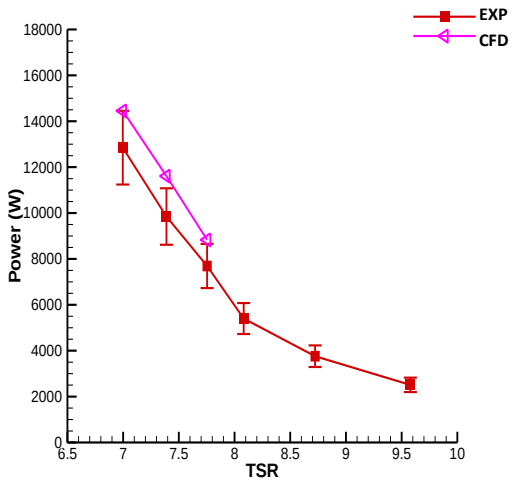

Figure 4.7: WINPhase 10 wind turbine power predictions compared with field measurement data.

The predictions for moments on the three wind turbine blades (as well as the total moment on all the blades) obtained from the unsteady DDES simulations are shown in Figure 4.8. A careful perusal of Figure 4.8 shows that the important transient effect is properly captured by the DDES method with the sliding mesh technique.

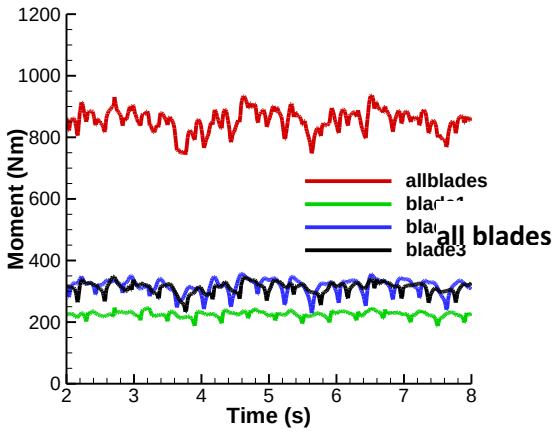

Figure 4.8: Calculated moment on the three wind turbine blades (as well as on all three blades) at $v_{ref} = 11\ \mathrm{m\ s^{-1}}$ at hub height.

Figure 4.9 exhibits the complex and unsteady vortical motions in the flow in the vicinity of a wind turbine by showing the iso-surface of Q criterion where $Q = 1$. It is clearly seen that the DDES simulation captures the well-defined tip vortices and mid-span vortices that are shed from the wind turbine blades. Interestingly, the advection of the tip vortices downstream of the wind turbine, as well as their interaction with the tower is evident on a careful examination of Figure 4.9.

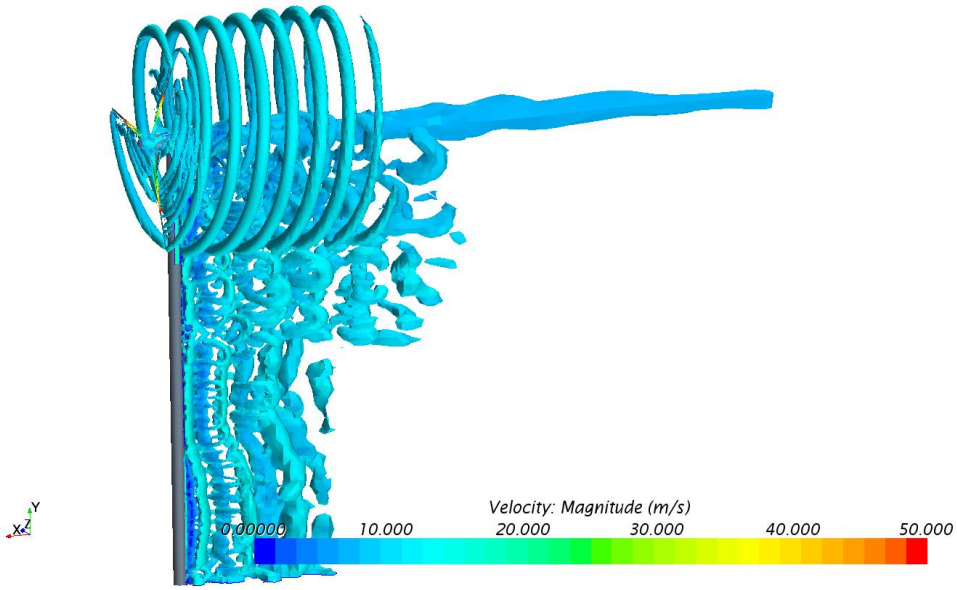

Figure 4.9: Vortices shed from the blades and tower of WINPhase 10 wind turbine at $v_{ref} = 11\ \mathrm{m\ s^{-1}}$ at hub height.

4.2 Acoustic Propagation Component Validation for Wind Turbine Acoustic Field Simulation

Three formulations are included in the acoustic propagation calculation, the impermeable formulation for a static source, the impermeable formulation for a moving

source and the permeable formulation of the FW-H equation. The tandem cylinders case was selected to validate the impermeable formulation for a static source and the WINPhase 10 wind turbine case was used to validate the impermeable formulation for a moving source and the permeable formulation of the FW-H equation.

4.2.1 Flow over Tandem Cylinders Validation Case

The calculation of this test case utilized the standard unsteady Reynolds Averaged Navier-Stokes (URANS) methodology in conjunction with the RNG $k-\varepsilon$ turbulence model. The experimental data used for the validation here were obtained from the Basic Aerodynamic Research Tunnel (BART) and Quiet Flow Facility (QFF) at NASA Langley Research Center. These measurement data included steady surface pressure, detailed off-surface measurements of the flow field using PIV, hot-wire measurements in the wake of the rear cylinder, unsteady surface pressure data and the radiated noise. A trip was used on the upstream cylinder during the test to ensure a fully turbulent shedding process and simulated the effects of a high Reynolds number flow. The detailed settings and methodology used during the experiment are documented in [137].

Because the flow field simulation needs to be conducted before the acoustic calculation can take place, the accuracy of the CFD simulation is crucial for the validation of the acoustic solver. As a consequence, the predictive accuracy of the CFD results are documented in this section to ensure that the sound source information provided by these results to the subsequent acoustic solver are reasonable.

4.2.1.1 Geometry and Mesh

Figure 4.10 illustrates the geometry of the tandem cylinders computational domain. D_{cy} represents the diameter of the cylinders where $D_{cy} = 0.05715\ \mathrm{m}$. The separation distance between the two cylinders is $3.7D_{cy}$.

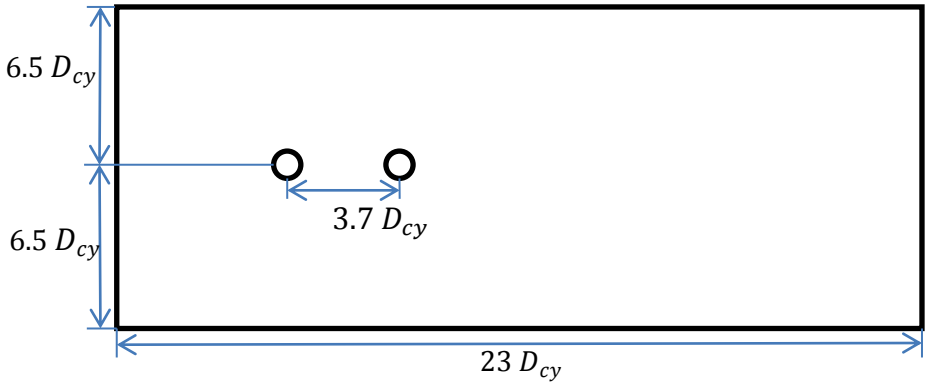

Figure 4.10: Computational domain for tandem cylinders CFD simulation.

Figure 4.11 shows the mesh on the computational domain and the area surrounding the cylinders. A structured grid consisting of 112,890 cells were generated using Ansys® DesignModeler®.

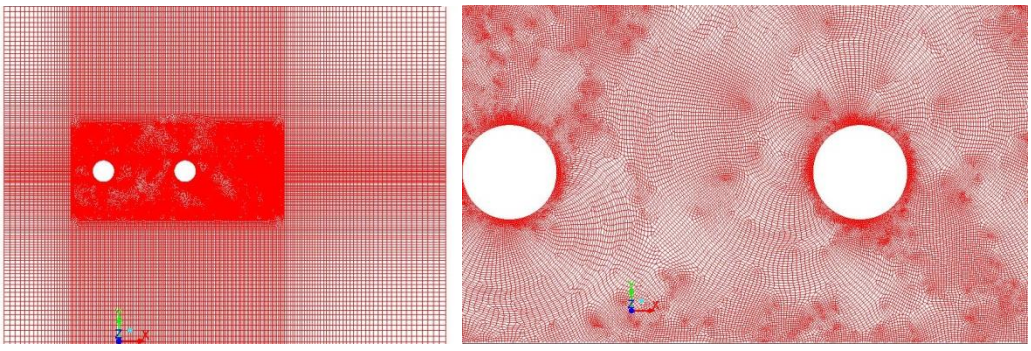

Figure 4.11: Mesh for tandem cylinders CFD simulation.

4.2.1.2 CFD Settings and Boundary Conditions

The unsteady RANS simulation of the flow field was undertaken using the commercial software ANSYS® Fluent®. A pressure-based solver was used for the incompressible flow calculation. The unsteady RANS calculation used the RNG $k-\varepsilon$ turbulence model with a standard wall function. A least-squares cell-based scheme was chosen for the gradient approximation of all quantities used in the discretization of the governing equations. A second-order upwind scheme was employed for discretization of the convective term in the momentum transport equation. A central differencing scheme was employed for the discretization of the diffusion terms in turbulence transport equations. A pressure-weighted interpolation scheme was used to estimate the pressure values at the cell faces from their values at the cell centroids. A second-order implicit scheme was chosen for the time marching algorithm with a maximum of 50 iterations permitted for each time step. The SIMPLE scheme was used here to enforce mass conservation through the pressure-velocity coupling.

Air properties at 21°C were used during the calculation. The Reynolds number based on cylinder diameter is $Re = 1.66\times10^{5}$. The non-dimensional time step is $t^{*} = 7\times10^{-4}$ where t^{*} is defined as $t^{*} = tU_{ref}/D_{cy}$ where t is the dimensional time step, and U_{ref} and D_{cy} represent the computational domain inlet velocity and the cylinder diameter, respectively.

A uniform velocity distribution was applied at the inlet of the computational domain with an inlet Mach number of $Ma = 0.128$. The pressure at the outlet boundary of the

domain was set to atmospheric pressure. The cylinder surface was treated as a no-slip smooth wall. The top and bottom boundaries of the computational domain were treated as symmetry planes.

4.2.1.3 Flow Field Results and Analysis

Figure 4.12 compares the lift and drag coefficients (c_l and c_d) of the downstream cylinder with numerical results reported in the reference [138] which also used a URANS methodology to simulate the tandem cylinders flow field. Both c_l and c_d in Figure 4.12 show the periodic structures which indicate that the flow has reached a quasi-steady state.

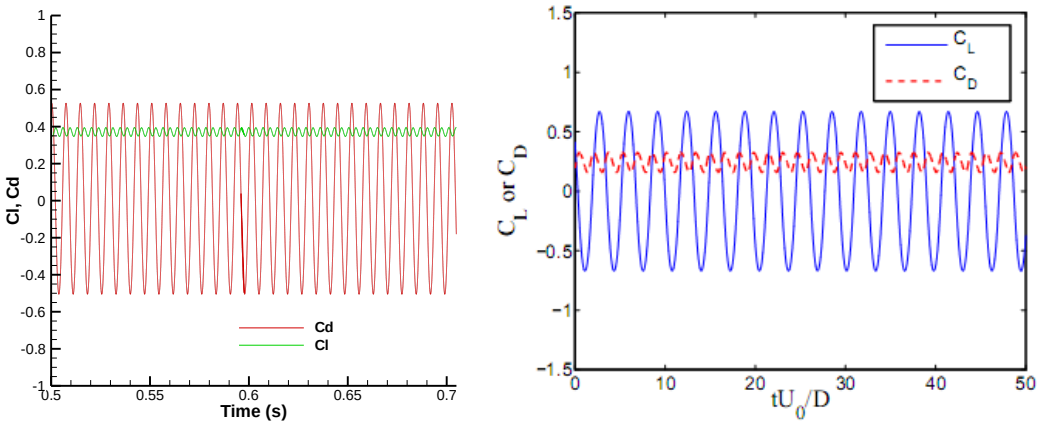

Figure 4.12: Lift and drag coefficients for downstream cylinder of current simulation (left) and numerical results reported in [138] (right).

Figures 4.13 and 4.14 show a comparison of the predictions of the mean surface pressure coefficient as a function of angular coordinates with some experimental data obtained from the BART and QFF. Both predictions and measurements show a

distribution that is symmetric with two prominent suction peaks. The effect of the boundary-layer trips on the front cylinder from BART experimental data is shown in Figure 4.13 at angular locations near $\theta_{cy} = 50°$ and $\theta_{cy} = 310°$, respectively.

For the upstream cylinder, the overall comparison of the predicted pressure coefficient with the measured pressure coefficient is good as is evident in Figure 4.13. The numerical prediction over-predicts the magnitude of pressure coefficient and predicts the location of the suction peaks further downstream. Computed base pressure towards the back portion of the cylinder is a bit higher than the measurements obtained from both experimental data sets.

For the downstream cylinder, good agreement with the experimental data is shown in Figure 4.14. The magnitude of the suction peaks is over-predicted. However, good agreement is attained for the base region with the QFF data. There is poor agreement at the stagnation region which is due to an over estimation of the mean streamwise flow velocity downstream of the upstream cylinder in the simulation.

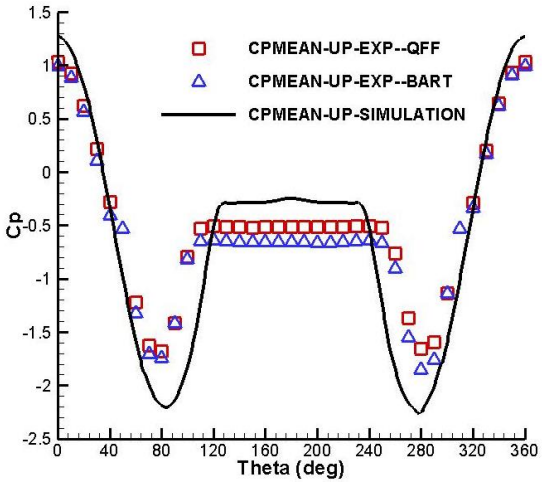

Figure 4.13: Mean surface pressure comparison for upstream cylinder.

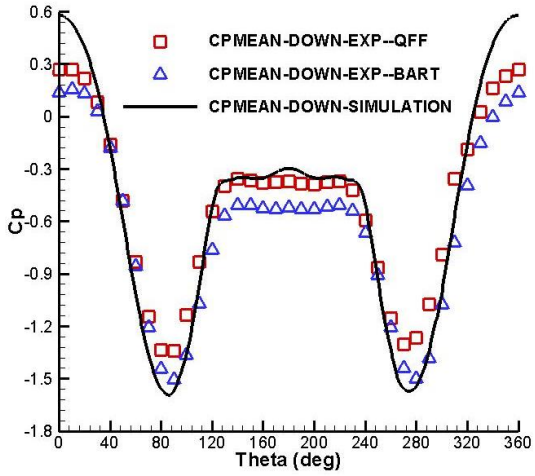

Figure 4.14: Mean surface pressure comparison for downstream cylinder.

Figures 4.15 and 4.16 exhibit the root-mean-square (RMS) surface pressure coefficient for the upstream and downstream cylinders, respectively. The simulation reproduces overall trends, but significantly under-predicts the peak amplitudes on both the upstream and downstream cylinders. The simulation results also under-predicts the fluctuation amplitude in the base regions of both cylinders.

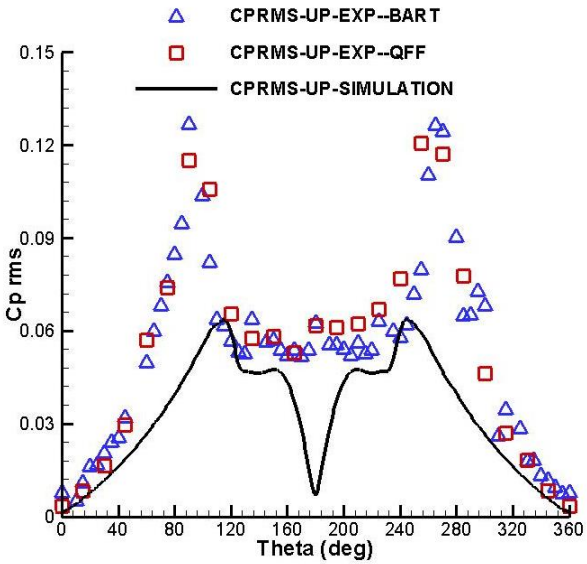

Figure 4.15: RMS surface pressure comparison for upstream cylinder.

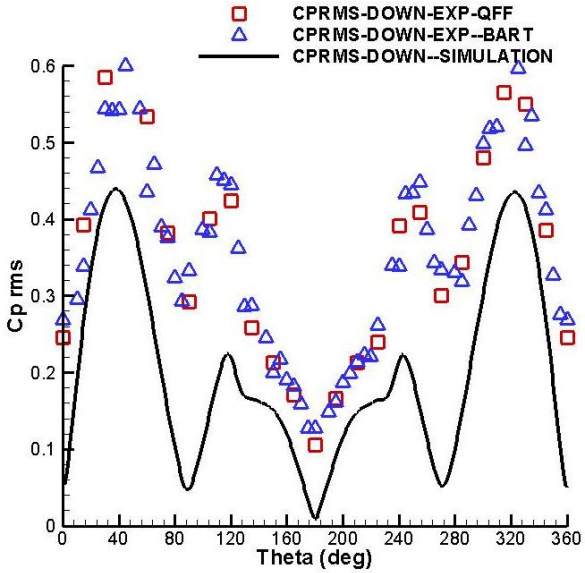

Figure 4.16: RMS surface pressure comparison for downstream cylinder.

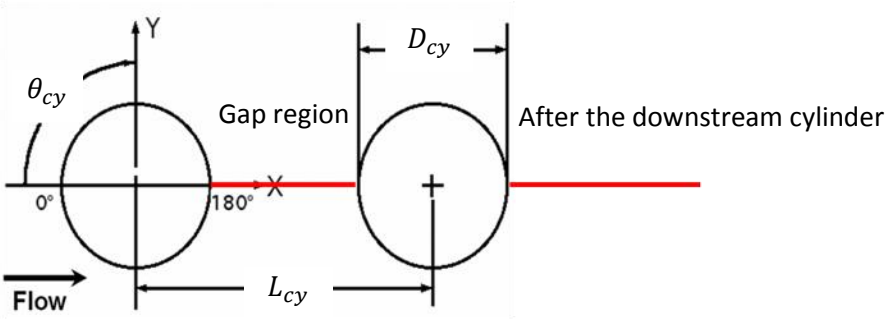

Figure 4.17: Sketch of the two regions used for the comparison between the predicted and measured mean velocity: namely, the gap region lying between the two cylinders and the region lying downstream of the downstream cylinder [137].

Figure 4.17 shows the sketch of two regions used for the comparison between the predicted and measured mean velocity. Figure 4.18 and Figure 4.19 show the comparisons of the mean velocity in these two regions with the experimental data obtained from the NASA BART facility. The mean velocity has been normalized with the free stream velocity (U_{ref}) in Figure 4.18 and Figure 4.19.

It can be seen in Figure 4.18 that the length of the recirculation bubble in the wake of the upstream cylinder is reasonably well predicted. However, the mean velocity downstream at $x/D_{cy} = 1.1$ is over-predicted, resulting from too high of an entrainment rate of free-stream flow into the gap region. This results in an over-prediction of the mean stagnation region surface pressure on the downstream cylinder as shown in Figure 4.14. The reason for this behavior in the URANS simulation is most probably linked to the incorrect prediction of the Reynolds stress, which distorts the recirculation bubble shape. In the tandem cylinders case, this effect did not change the length of the recirculation bubble, but constrains its width [138]. A similar effect is

responsible for the distortion of the recirculation bubble in the wake of the downstream cylinder as well. Figure 4.19 shows a comparison of the predicted and measured mean velocity in the region downstream of the downstream cylinder. Overall, it is seen that the mean velocity in this region is under-predicted.

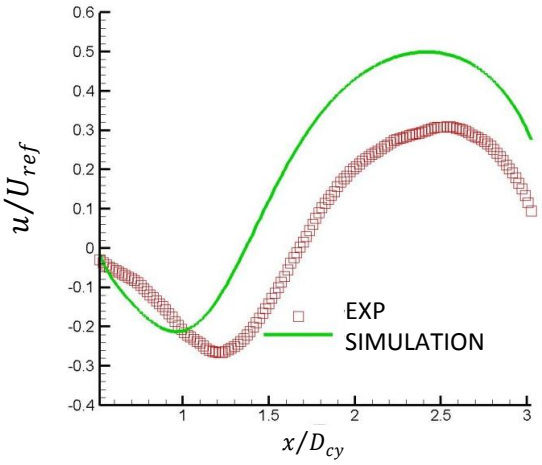

Figure 4.18: Mean velocity comparison in the gap region.

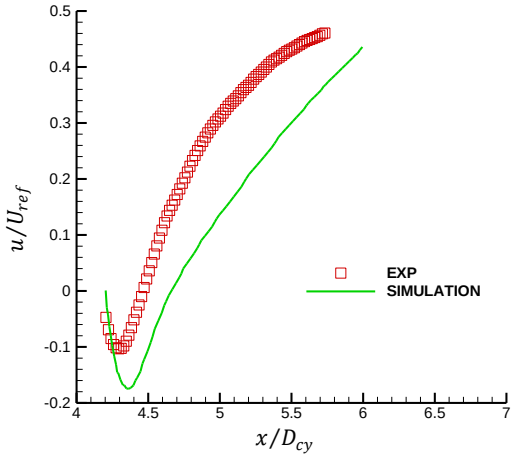

Figure 4.19: Mean velocity comparison in the region after the downstream cylinder.

The locations at which measurements of the power spectral density (PSD) of the unsteady surface pressure are conducted are shown in Figure 4.20. The predicted PSD of the unsteady surface pressure at these azimuthal locations on the upstream and downstream cylinders is compared with the corresponding experimental data in Figure 4.21 and Figure 4.22. The predicted results are extremely tonal in nature, in contrast to the experimental results. The numerical predictions recreate harmonics as seen in the experimental data for the measurement locations on both the upstream and downstream cylinders. The frequency of the first peak at both these locations is in good agreement with the experimental data but the amplitude is slightly over-predicted in the numerical prediction.

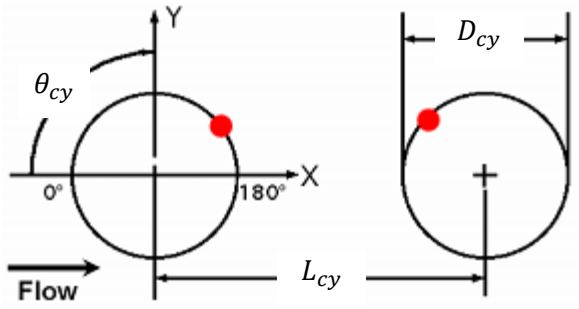

Figure 4.20: Sketch showing the measurement locations for PSD of unsteady surface pressure calculation [137].

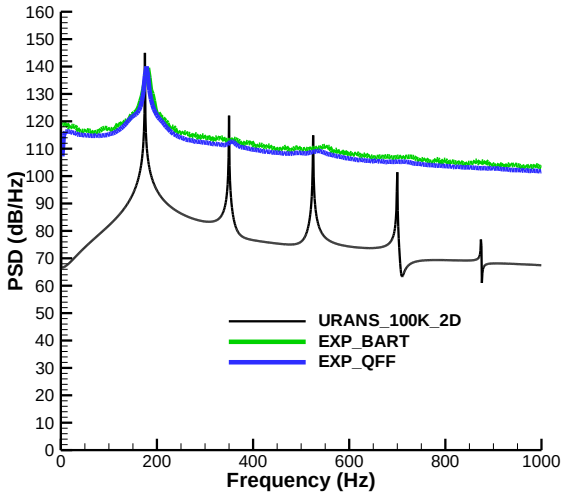

Figure 4.21: PSD of surface pressure at an azimuthal location on the upstream cylinder.

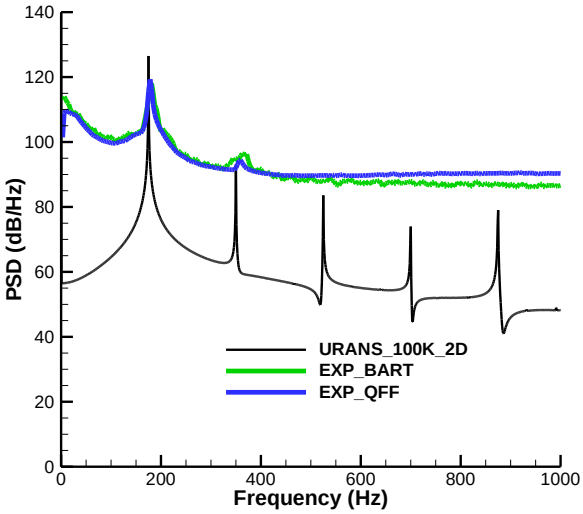

Figure 4.22: PSD of surface pressure at an azimuthal location on the downstream cylinder.

A comparison between the predicted and the measured instantaneous spanwise vorticity is shown in Figure 4.23. The experimental results show vortical structures on two scales. As the shear layers form from the separation zones on the cylinder surfaces, Kelvin-Helmholtz (K-H) instabilities create small vortex structures. These eventually

influence each other in a pairing process to form larger vortex structures more commonly associated with a Von Karman street. It is interesting and important to note that the larger scale structures consist of well-defined smaller vortical structures that appear to have their origin in the K-H instability that occurs in the earlier shear layer.

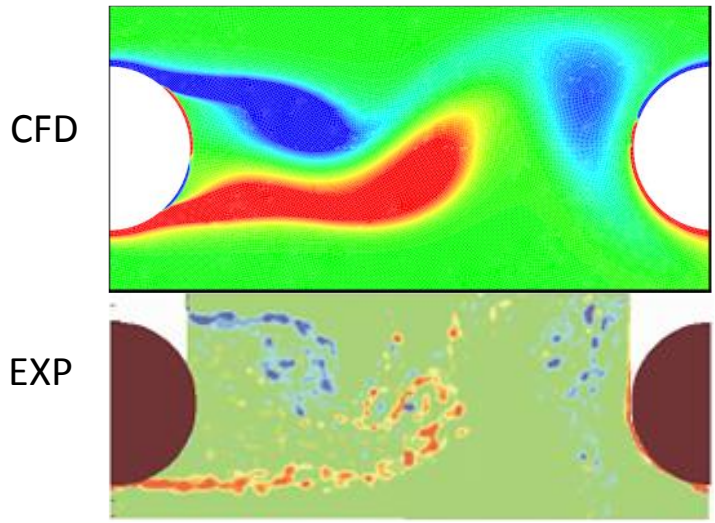

Figure 4.23: Instantaneous spanwise vorticity comparison in the gap region between the two cylinders.

The computed vorticity shows only larger scale vortical structures and they are of the same scale and magnitude as those in the experiment. The turbulence model used in the URANS simulation does not allow a resolution of the fluctuations associated with the K-H instability and other small scale turbulence effects. This result illustrates why the URANS surface pressures and forces are so tonal in nature as seen in Figure 4.21 and Figure 4.22. With the finer scale structures modeled, only the larger scale, smoothly varying velocity field are properly resolved in the simulation.

4.2.1.4 Acoustic Calculation Settings

The impermeable formulation of the FW-H equation was employed for the noise prediction of flow over the tandem cylinders (corresponding to a static sound source). The noise data were acquired on the surfaces of the two cylinders at a sampling frequency of 1000 kHz for a time interval of 0.2 s. The Stirling scheme was applied for the discretization of the time derivatives in this formulation. Three microphones are placed in far field of the radiating sound source as shown in Figure 4.24.

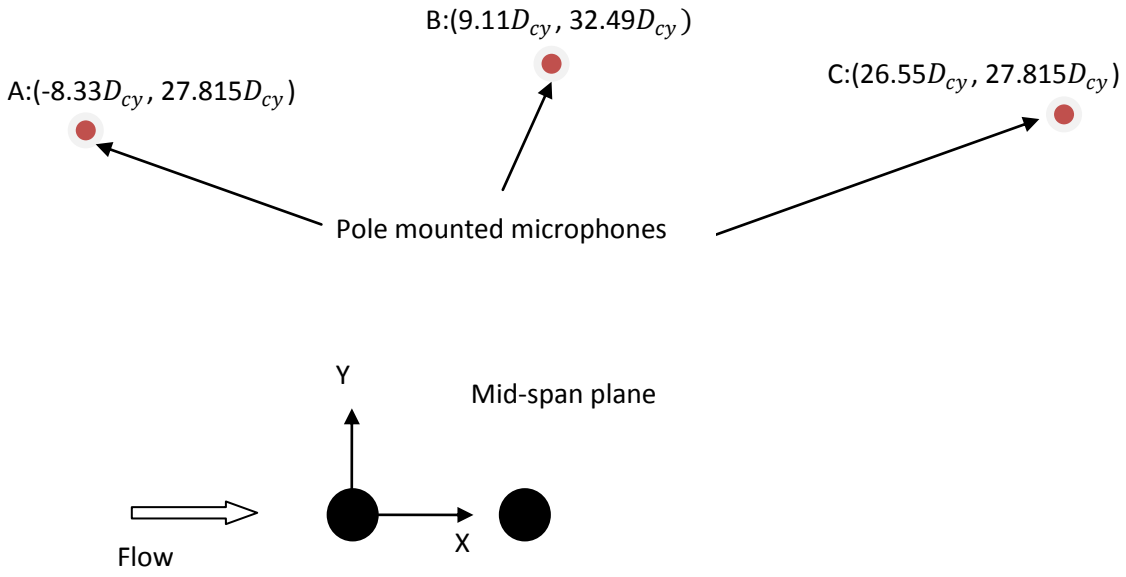

Figure 4.24: Sketch of the microphone locations in experiment conducted in the QFF (not to scale).

4.2.1.5 Acoustic Field Results and Analysis

Figure 4.25 to Figure 4.27 compare the numerical results with the experimental data obtained from QFF for the power spectral density of the acoustic sound levels at three microphone locations shown in Figure 4.24. A comparison between the numerical results and experimental data on these three microphone locations exhibits a number of similarities. The peak magnitude and frequency are well predicted. The locations of the frequencies of the harmonics are predicted accurately, but the magnitude of the first three harmonics is over predicted whereas the magnitude of the fourth harmonic is under predicted. Furthermore, the broadband noise level is under predicted, resulting in a very tonal characteristic for the spectrum measured at the three locations. The reason might be due to the implicit time-averaging of the quantities predicted by the URANS model as discussed in Section 4.2.1.3, which filters out all the small-scale fluctuations that are expected to contribute to the broadband noise. In order to improve the broadband component prediction in the SPL spectrum, a more computational demanding LES solver can be used. The numerical results using the LES solver are summarized in [137].

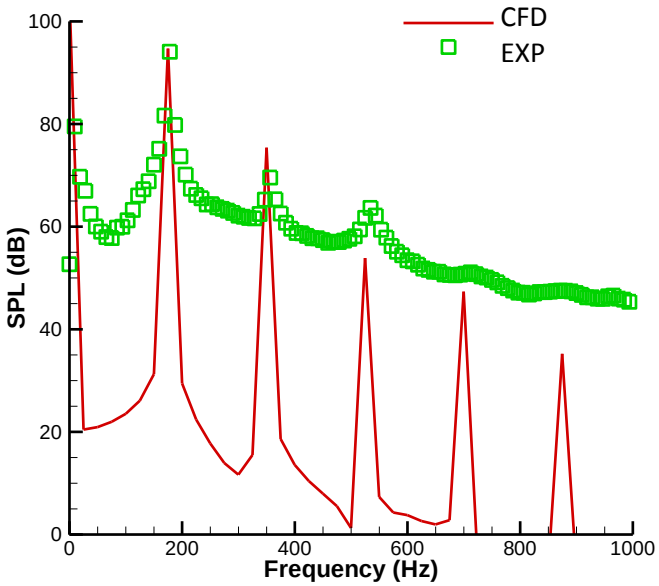

Figure 4.25: The predicted and experimental SPL of the acoustic signal at microphone A (cf. Figure 4.24).

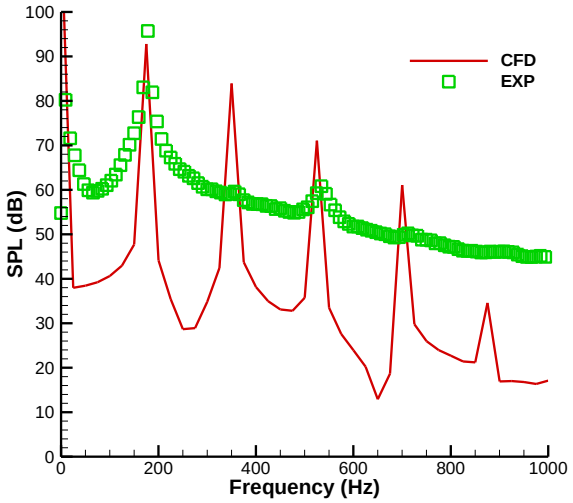

Figure 4.26: The predicted and experimental SPL of the acoustic signal at microphone B (cf. Figure 4.24).

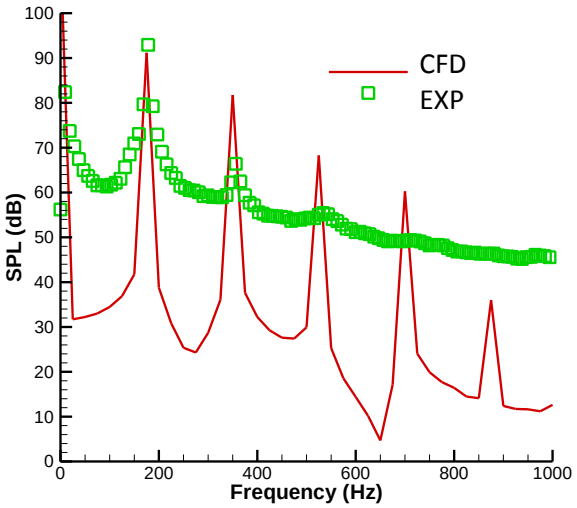

Figure 4.27: The predicted and experimental SPL of the acoustic signal at microphone C (cf. Figure 4.24).

The thickness and loading terms for the FW-H impermeable formulation are plotted for microphone location A in Figure 4.28. According to acoustic theory, the noise generation mechanism for the flow over tandem cylinders is due to the unsteady loadings applied on the cylinder surfaces. As a consequence, the thickness term in the FW-H equation should result in very small contributions to the noise level. Indeed, Figure 4.28 shows that the thickness term is roughly zero at microphone A, which indicates that thickness noise is not the main sound generation mechanism for the tandem cylinders case. On the other hand, the loading term which provides the main contribution to the SPL exhibits a periodic structure. This periodic structure is consistent with the characteristic tonal shape evident in the spectrum at microphone A exhibited in Figure 4.25. The sound pressure at microphones B and C have similar behaviors as is evident on a perusal of Figure 4.26 and Figure 4.27.

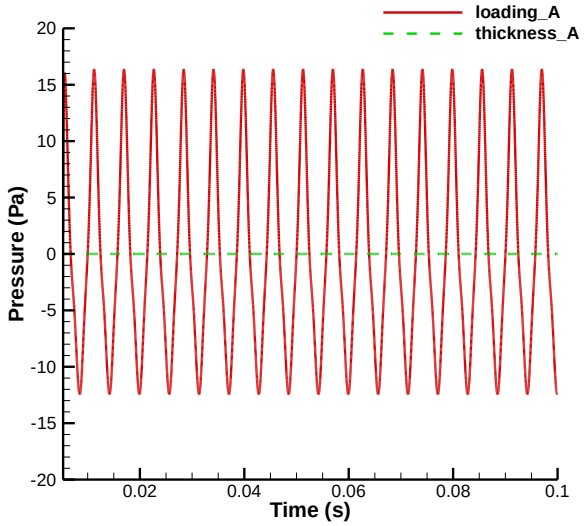

Figure 4.28: Thickness and loading terms calculated by the FW-H acoustic solver at microphone A for tandem cylinders case.

4.2.2 WINPhase 10 Wind Turbine Validation Case

4.2.2.1 Acoustic Calculation Settings

Two formulations of the FW-H equation were used for noise prediction for this small wind turbine: namely, the impermeable and permeable formulations. The impermeable formulation utilizes the acoustic data obtained on various impenetrable surfaces associated with the wind turbine such as the three wind turbine blades and the nacelle. The permeable formulation utilizes the noise data on the permeable surfaces which encloses the permeable domain as shown in Figure 4.5.

Two discretization schemes were employed to approximate the time derivatives in both formulations. They are the CDS and Stirling schemes as described in Section 3.3.5. The

data sampling frequency was 10 kHz and the sampling period consisted of three to six complete revolutions of the wind turbine blades.

For the field measurements, one microphone was placed at the wind turbine reference point in accordance with the AWEA [3] and IEC [1] standards as illustrated in Figure 4.29. To compare the numerical predictions with the field measurement data, an A-weighting followed by one-third octave band averaging, were applied to the predicted SPL spectra. The A-weighting function and the determination of the center frequencies and higher and lower frequency boundaries (the band width) that define each one-third octave band can be found in reference [139]. An arithmetical average is used to calculate the averaged A-weighted SPL within each one-third octave band.

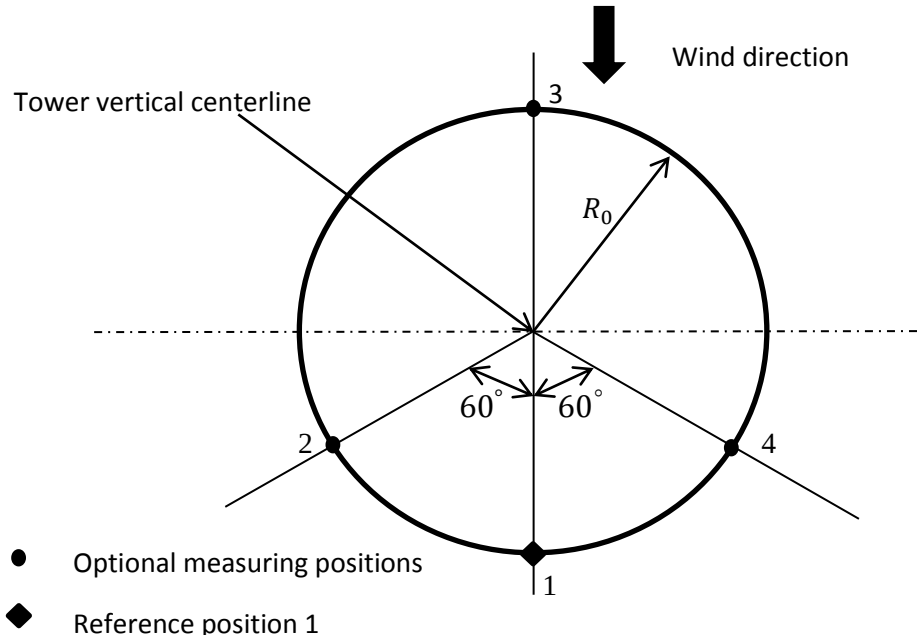

Figure 4.29: Standard configuration for microphone measurement positions (plan view).

4.2.2.2 Acoustic Field Results and Analysis

Figure 4.30 compares the predicted spectra for the A-weighted sound pressure level (SPLA) for the one-third octave band at the reference location with the associated field measurements. The predictions were obtained using both the STAR-CCM+® acoustic module and our in-house acoustic code. Both of these numerical predictions for the magnitude of the SPLA at the one-third octave band (red and blue bars for, respectively, the STAR-CCM+® and the in-house code results) agree very well with each other over the range of frequencies considered. Furthermore, it is seen these predictions agree well with the experimental measurements of the SPLA magnitude at the one-third octave band (black bars). Finally, the narrow-band spectra of the SPLA predicted using the STAR-CCM+® acoustic module (red continuous curve in Figure 4.30) and using the in-house acoustic code (blue continuous curve in Figure 4.30) are seen to agree well with each other. The results of Figure 4.30 provide some verification and validation that our in-house FW-H code is providing correct predictions for the wind turbine noise.

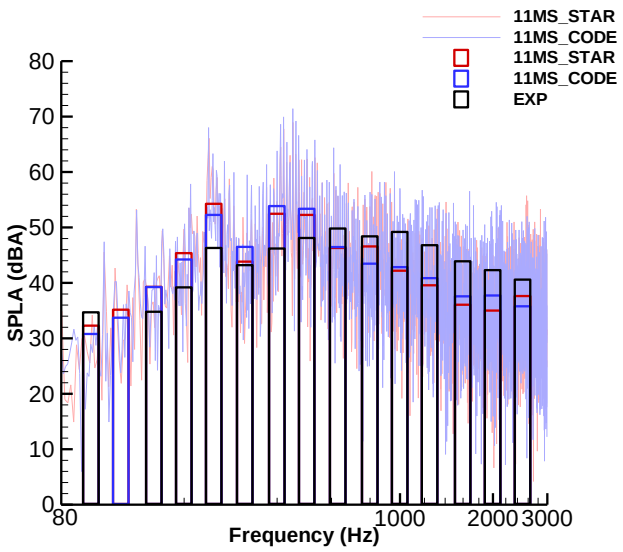

Figure 4.30: Spectra of the A-weighted sound pressure level (SPLA) predicted at $v_{ref} = 11.0\ \mathrm{m\ s^{-1}}$ at hub height. The predicted results are compared with some experimental data (EXP). The continuous lines correspond to the narrow-band SPLA and the bars denote the magnitude of the one-third octave band SPLA. The red and blue continuous lines and bars correspond to the predicted results obtained, respectively, using the STAR-CCM+® acoustic module and the in-house acoustic code. The black bars correspond to experimental data for the magnitude of the SPLA at the one-third octave band.

Figure 4.31 compares the field measurements with various predictions of the SPLA at the one-third octave band obtained from simulation data sets that include an integral number of revolutions of the wind turbine blades. This number ranges from three to six complete revolutions of the wind turbine blades. A perusal of Figure 4.31 allows one to determine the influence of using different numbers of revolutions of the turbine blades on the estimation of the SPLA at the one-third octave band. As more complete revolutions of the wind turbine blades are used for the estimation of the magnitude of the A-weighted SPL at the one-third octave band, the shape of the distribution (spectra) of the SPLA does not change as a function of the frequency, but it is seen that the

overall magnitude of the SPLA at the one-third octave band at any fixed frequency is reduced. This may be the result of the numerical dissipation inherent in the second-order scheme used for the discretization of the convective terms in the momentum transport equations (used in the aerodynamic simulations), which might not affect the overall flow field but have an impact on the acoustic field since the acoustic energy is only a small fraction of the energy contained in the flow field. Given the computational resources available to us, simulated data sets obtained from three complete revolutions of the wind turbine blades have been used for the calculation of the results reported in the remainder of this thesis (unless otherwise indicated).

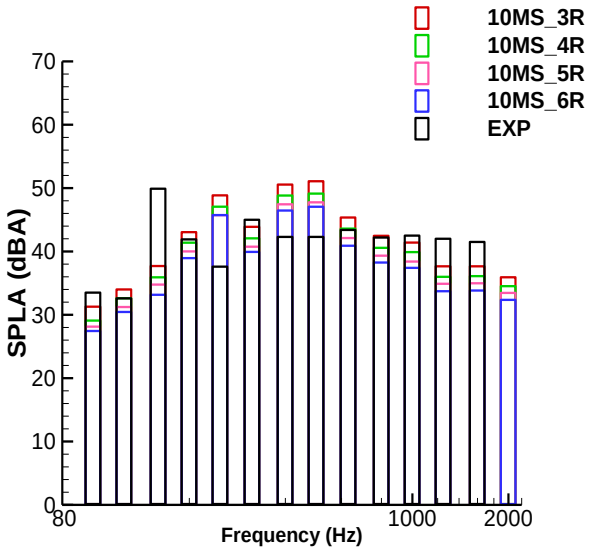

Figure 4.31: Spectra of A-weighted sound pressure level (SPLA) at the one-third octave band at $v_{ref} = 10.0\ \mathrm{m\,s^{-1}}$ at hub height. The magnitudes (indicated by the height of the bars) of the predicted SPLA at the one-third octave band are compared with some experimental measurements (EXP). The predictions of the magnitude of the SPLA at the one-third octave band were obtained using simulated data sets that involved an integral number of revolutions of the wind turbine blades (red bar: 3 revolutions; green bar: 4 revolutions; pink bar: 5 revolutions; blue bar: 6 revolutions). These various predicted magnitudes can be compared to the experimental measurements (black bar).

Two different discretization schemes, namely the CDS and the Stirling scheme, have been used to approximate the time derivatives in FW-H permeable formulation. Figure 4.32 to Figure 4.34 exhibit the A-weighted SPL spectra at three different reference velocities (at hub height), namely, $v_{ref} = 9\ \mathrm{m\ s^{-1}}$, $v_{ref} = 10\ \mathrm{m\ s^{-1}}$, and $v_{ref} = 11\ \mathrm{m\ s^{-1}}$. It is seen from Figure 4.32 to Figure 4.34 that the results obtained from the CDS and the Stirling schemes are comparable, except for frequencies above approximately 1000 Hz. At these higher frequencies, it is noted that the higher-order Stirling scheme yields slightly better predictions of the magnitude of the SPLA at the one-third octave band than those obtained using the CDS (as compared to the available experimental measurements of this quantity). Overall, it is assessed that both the CDS and Stirling schemes result in predictions of the wind turbine noise levels that are in good agreement with the corresponding experimental measurements at the three wind speeds tested. Nevertheless, the broadband wind turbine noise level above 1000 Hz appears to be under-predicted. This may be the result of the numerical dissipation (as mentioned above) inherent in the discretization of the convective terms in the momentum transport equation (viz., in the CFD simulations that provide the input data needed for the subsequent acoustic predictions).

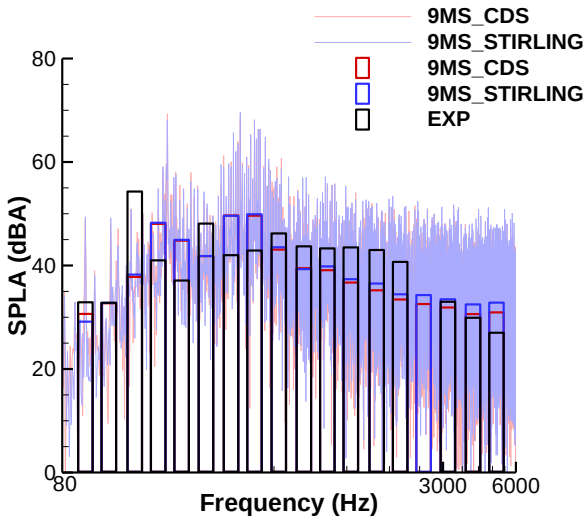

Figure 4.32: Spectra of the A-weighted sound pressure level (SPLA) at $v_{ref} = 9.0\ \mathrm{m\,s^{-1}}$ at hub height. The continuous lines show the narrowband spectra of the SPLA obtained using two different discretization schemes for the time derivative in the FW-H equation (red line: central difference scheme; blue line: Stirling scheme). The bars correspond to the magnitude of the SPLA averaged over one-third octave bands (red bar: central differencing scheme; blue bar: Stirling scheme; black bar: experimental data (EXP)).

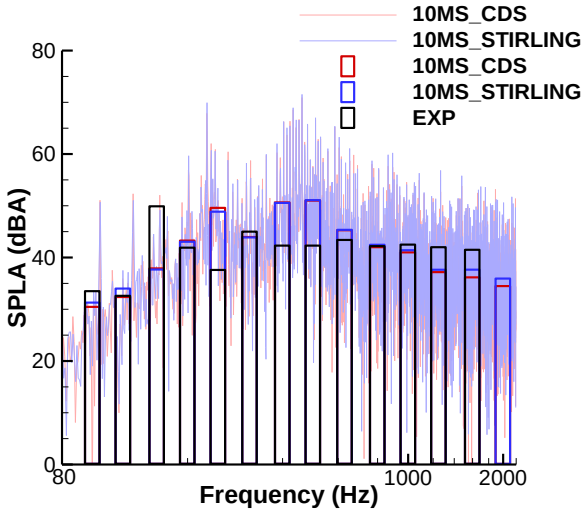

Figure 4.33: Spectra of the A-weighted sound pressure level (SPLA) at $v_{ref} = 10.0\ \mathrm{m\,s^{-1}}$ at hub height.The continuous lines show the narrowband spectra of the SPLA obtained using two different discretization schemes for the time derivative in the FW-H equation (red line: central difference scheme; blue line: Stirling scheme). The bars correspond to the magnitude of the SPLA averaged over one-third octave bands (red bar: central differencing scheme; blue bar: Stirling scheme; black bar: experimental data (EXP)).

Next, we consider the differences between using the impermeable and permeable formulations of the FW-H equations for the acoustic predictions. The sound source data acquisition surface for the impermeable formulation of the FW-H equation coincides with the wind turbine blade surfaces. The comparison of the permeable and impermeable FW-H formulations for wind turbine noise prediction is shown in Figure 4.35. In these simulations, only one revolution of the wind turbine blades was used for the determination of the A-weighted SPL owing to the very large disk storage required to archive the data (e.g., nearly 100 GB of data were exported from the simulation of one revolution of the wind turbine blades for the impermeable FW-H formulation). The results from the impermeable and permeable formulations of the FW-H equation give similar spectra for the SPLA in terms of their overall shape at frequencies below 1000 Hz. However, it is seen that the SPLA levels at frequencies below 1000 Hz are smaller for the impermeable formulation of the FW-H equation as compared to those for the permeable formulation. Moreover, for frequencies above 1000 Hz, it is seen from Figure 4.35 that the impermeable formulation of the FW-H equation predicts sound pressure levels that are significantly smaller than those predicted using the permeable formulation, and this difference is seen to increase with increasing frequency above 1000 Hz. The permeable formulation of the FW-H equation gives predictions for the magnitude of the SPLA at the one-third octave band that agree well with the experimental measurements. The differences in the predictions provided by the impermeable and permeable formulations of the FW-H equation can be attributed to the quadrupole sources which were included within the permeable surface and which

contributed significantly to the broadband noise at frequencies above 1000 Hz. A perusal of Figure 4.35 also suggests that the blade self-noise provides an important contribution to the sound pressure level in the range of frequencies between approximately 250 Hz and 1000 Hz. This is consistent with similar observations obtained in some experimental measurements [63].

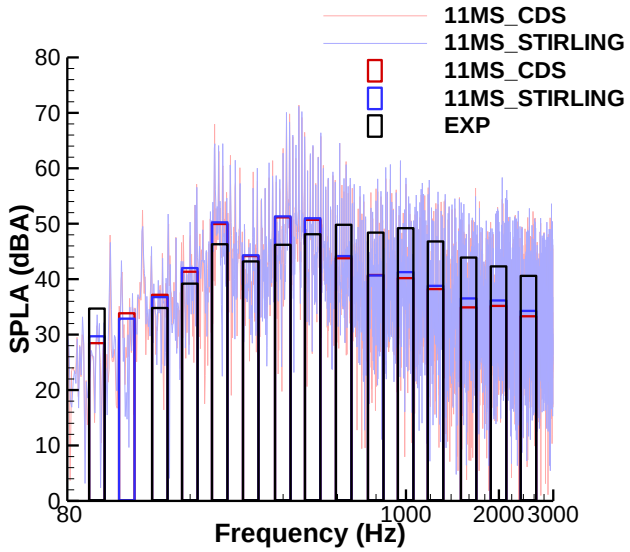

Figure 4.34: Spectra of the A-weighted sound pressure level (SPLA) at $v_{ref} = 11.0\ \mathrm{m\,s^{-1}}$ at hub height. The continuous lines show the narrowband spectra of the SPLA obtained using two different discretization schemes for the time derivative in the FW-H equation (red line: central difference scheme; blue line: Stirling scheme). The bars correspond to the magnitude of the SPLA averaged over one-third octave bands (red bar: central differencing scheme; blue bar: Stirling scheme; black bar: experimental data (EXP)).

It is interesting to consider the differences in the wind turbine noise predictions between the rotor only and the full wind turbine simulations. Figure 4.36 shows the comparison in the predictions of the SPLA from the rotor only and the full wind turbine simulations. In these simulations, the DDES method was used with a one-seventh

power-law velocity profile (with a reference wind speed at hub height of 10 m s^{-1}) as the inlet boundary condition. The acoustic predictions for each case were made using the permeable formulation of the FW-H equation. An examination of Figure 4.36 shows that the rotor only simulation (blue curve) results in larger SPLs at frequencies below approximately 200 Hz as compared to the full wind turbine simulation (red curve). This condition is reversed for frequencies greater than approximately 200 Hz, where it is seen that the SPLA amplitudes for the full wind turbine simulation are larger than those for the rotor only simulation. In particular, the spectrum of the SPLA for the rotor only simulation shows a sharp decrease between approximately 300 Hz and 1000 Hz and a slight increase at frequencies above approximately 1000 Hz. Taken together, these results indicate that the presence of the tower might have suppressed the noise level at frequencies below 200 Hz. On the other hand, the existence of the tower enhances the amplitude of the SPLA at frequencies above approximately 300 Hz. This might be due to the noise source from tower itself or from the interaction between the tower and the wakes produced by the wind turbine blades. Finally, a comparison of the magnitudes of the SPLA at the one-third octave band in Figure 4.36 shows that the predictions of this quantity obtained from the full wind turbine simulation are in better conformance with the experimental measurements than those provided by the rotor only simulation.

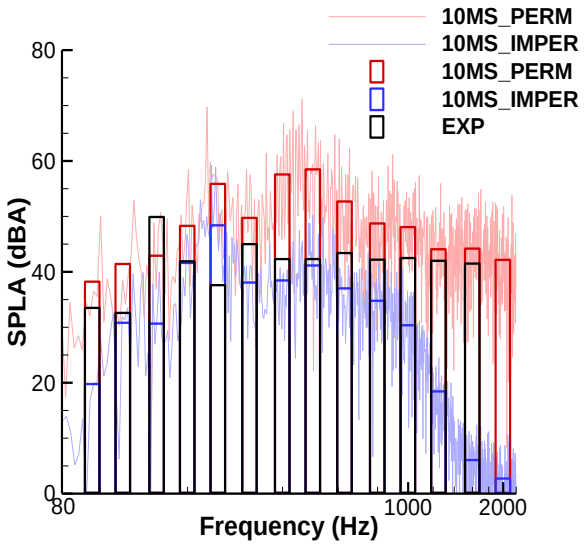

Figure 4.35: Spectra of the A-weighted sound pressure level (SPLA) at $v_{ref} = 10.0\ \mathrm{m\ s^{-1}}$ at hub height. For these predictions of the SPLA, two different formulations of the FW-H equations were used: namely, the permeable formulation (red line) and the impermeable formulation (blue line). The bars correspond to the magnitudes of the SPLA averaged over one-third octave bands (red bar: permeable formulation; blue bar: impermeable formulation; black bar (experimental data or EXP)).

The numerical dissipation introduced by the second-order scheme used for the discretization of the convective terms in the governing equations for the CFD simulations results in the decreasing SPLs for all frequencies in the acoustic spectra. Despite the coarse-resolution computational mesh used for our simulations, a good agreement was obtained for the A-weighted one-third octave spectra of the SPLs between the numerical acoustic simulations and the experimental measurements at three different incident wind speeds. This good agreement provides some validation that our in-house acoustic solver is able to provide accurate predictions of the noise emitted from small HAWTs.

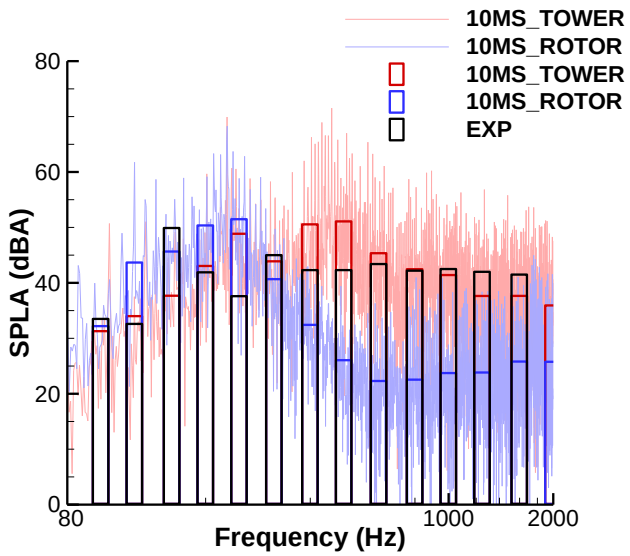

Figure 4.36: Spectra of the A-weighted sound pressure level (SPLA) at $v_{ref} = 10.0\ \mathrm{m\,s^{-1}}$ at hub height. For these predictions of the SPLA, two different simulation cases were considered: namely, the entire wind turbine with the tower (red line) and rotor only (blue line). The bars correspond to the magnitudes of the SPLA averaged over one-third octave bands (red bar: entire wind turbine with tower; blue bar: rotor only configuration; black bar (experimental data or EXP)).

4.3 Acoustic Beamforming Component Validation for Noise Source Localization

In an acoustic beamforming measurement, a validation test is usually conducted with a point source at a single frequency. The monopole sound source is placed in front of the microphone array where the acoustic beamforming is performed. The resulting acoustic image should contain only one acoustic hotspot at the point source's frequency. No noise emission should be detected on the rest of the acoustic maps at frequencies other than the frequency of the tested sound source.

For validation of the acoustic beamforming component, the point source and the acoustic field were simulated and the acoustic signal at each microphone was calculated. Acoustic beamforming was then performed with these predicted acoustic signals to create the acoustic images. The detailed settings, the microphone array as well as the acoustic beamforming algorithm used are described in Section 4.3.1. The predicted results are compared with the experimental data in Section 4.3.2.

4.3.1 Numerical Settings

The validation test setup is illustrated in Figure 4.37. A 5 kHz monopole sound source is placed 1 m away from the center of the microphone array. Two microphone array designs, namely, the Archimedean spiral array and the star array, were utilized for the validation test. The Archimedean spiral array has 66 microphones whereas the star array has 63 microphones. Both microphone arrays have roughly the size of 2 m × 2 m. Note that the same array designs with a different array size were also used for the validation of the computational acoustic beamforming method for the NACA 0012 airfoil and for the CAB method applied to the WINPhase 10 wind turbine.

The acoustic maps were computed on the source plane with a size of 0.5 m × 0.5 m as shown in Figure 4.37. The acoustic maps were computed for the one-third octave bands in the frequency range from 100 Hz to 10 kHz. The acoustic map had 51 points in both directions for a total of 2601 grid points. The color contours in the acoustic maps were normalized to 0 dB at maximum and a 15 dB dynamic range was applied in order to

match the acoustic maps with the experiment. The numerical sampling frequency was 100 kHz for a sampling period of 1 second.

Both the plane wave and spherical wave acoustic fields were simulated in order to validate the acoustic beamformers in the far and near fields of the sound source, respectively. The diagonal removal technique described in Section 3.4.1.3 was applied to both the near-field and far-field acoustic beamformers in order to evaluate its effect on the resulting acoustic maps.

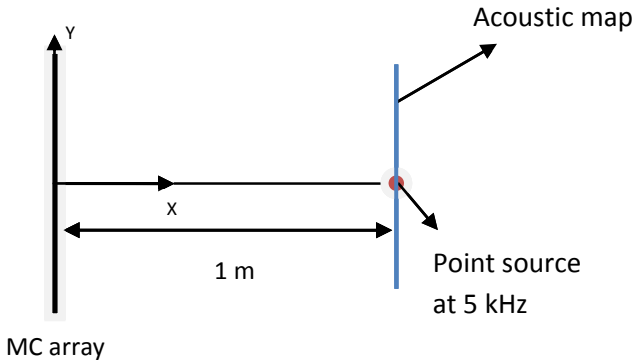

Figure 4.37: Schematic plot of the point source validation case setup.

4.3.2 Acoustic Beamforming Results and Analysis

Firstly, the predicted acoustic images were compared with the experimental results to validate the acoustic beamforming solver. In order to match the experimental setup, the plane wave incident acoustic beamforming algorithm and Archimedean spiral microphone array were used in the numerical simulation. Figure 4.38 compares the predicted acoustic images with the experimental results at 5 kHz. The left panel

presents the experimental results and the right panel presents the numerical results. The top row in Figure 4.38 shows the results using the plane wave incident acoustic beamforming algorithm and the bottom row shows the results with the inclusion of the diagonal removal technique in the plane wave incidence acoustic beamforming algorithm. It is seen that the predicted acoustic images agree quantitatively well with the test results. Furthermore, the addition of the diagonal removal process lowers the MSL and suppresses the microphone self-noise in the numerical simulations, which is evident on a comparison of the top and bottom acoustic images in the right panel of Figure 4.38. However, this improvement is not as obvious when one compares the top and bottom images in the left panel of Figure 4.38, which correspond to acoustic beamforming using the measured data. Nevertheless, the good agreement of the acoustic images at 5 kHz between the simulation and experiment provides evidence of the correct and accurate application of the numerical acoustic beamforming algorithm for the localization of the acoustic sound sources for this monopole sound source case.

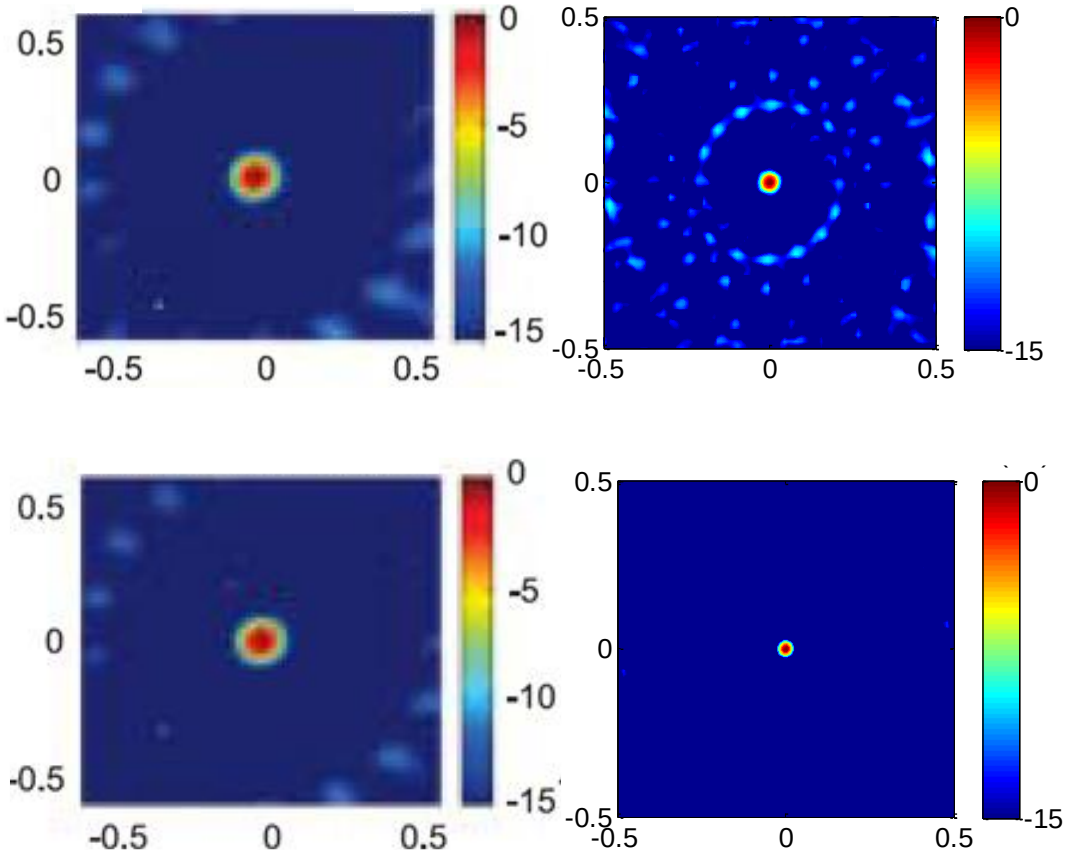

Figure 4.38: Point source validation results from experiment (left panel) [128] and simulation (right panel) using the Archimedean spiral array for a plane wave incidence. The top row shows the results from plane wave incident beamforming algorithm and the bottom row shows the results with inclusion of the diagonal removal technique.

Secondly, the spherical wave incident acoustic beamforming algorithm was implemented numerically for the Archimedean spiral array. The diagonal removal technique was also included in the acoustic beamforming algorithm in order to evaluate its effect for spherical wave incidence. Figure 4.39 compares the acoustic images at 5 kHz with and without the inclusion of the diagonal removal process for the Archimedean spiral array. Similar to the plane wave incidence scenario as shown in Figure 4.38, the diagonal removal process also suppresses the microphone self-noise and decreases the

MSL on the resulting acoustic maps for the spherical wave incidence scenario. Figure 4.38 and Figure 4.39 summarize our efforts to validate the acoustic beamforming algorithm for both plane wave incidence and spherical wave incidence for a point source.

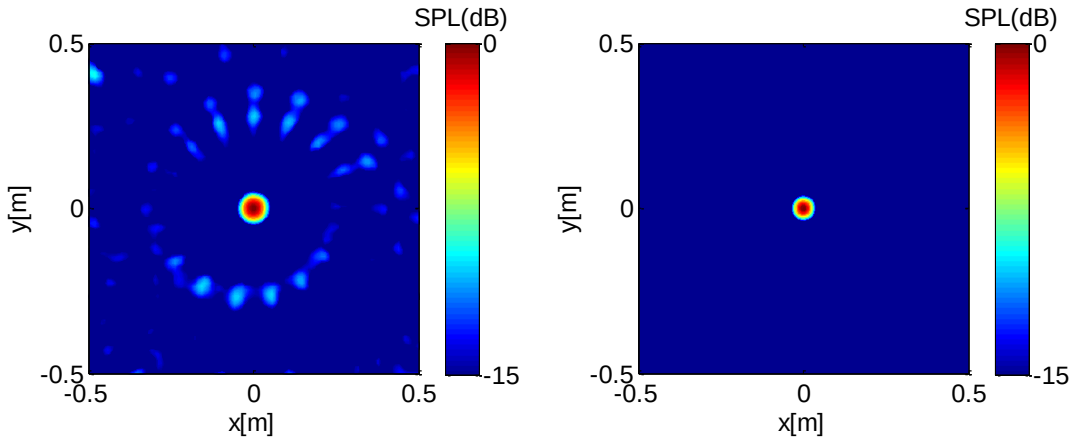

Figure 4.39: Comparison of numerical results with (right) and without (left) the inclusion of the diagonal removal process for the monopole source validation case using a spherical-wave incidence acoustic beamformer with the Archimedean spiral array.

Lastly, the star microphone array was used for validation of the plane wave incidence and spherical wave incidence acoustic beamforming algorithms. The diagonal removal process was also evaluated in this case for these algorithms. Figure 4.40 compares the predicted acoustic images using the star microphone array (right panel) and the Archimedean spiral array (left panel). It is seen that both microphone arrays predict the monopole sound source location correctly on the acoustic map at 5 kHz. It is also observed that the elimination of the diagonal elements in the cross spectral matrix reduces the microphone self-noise on the acoustic maps for both the plane wave

incidence and spherical wave incidence acoustic beamforming algorithms for the two microphone array designs.

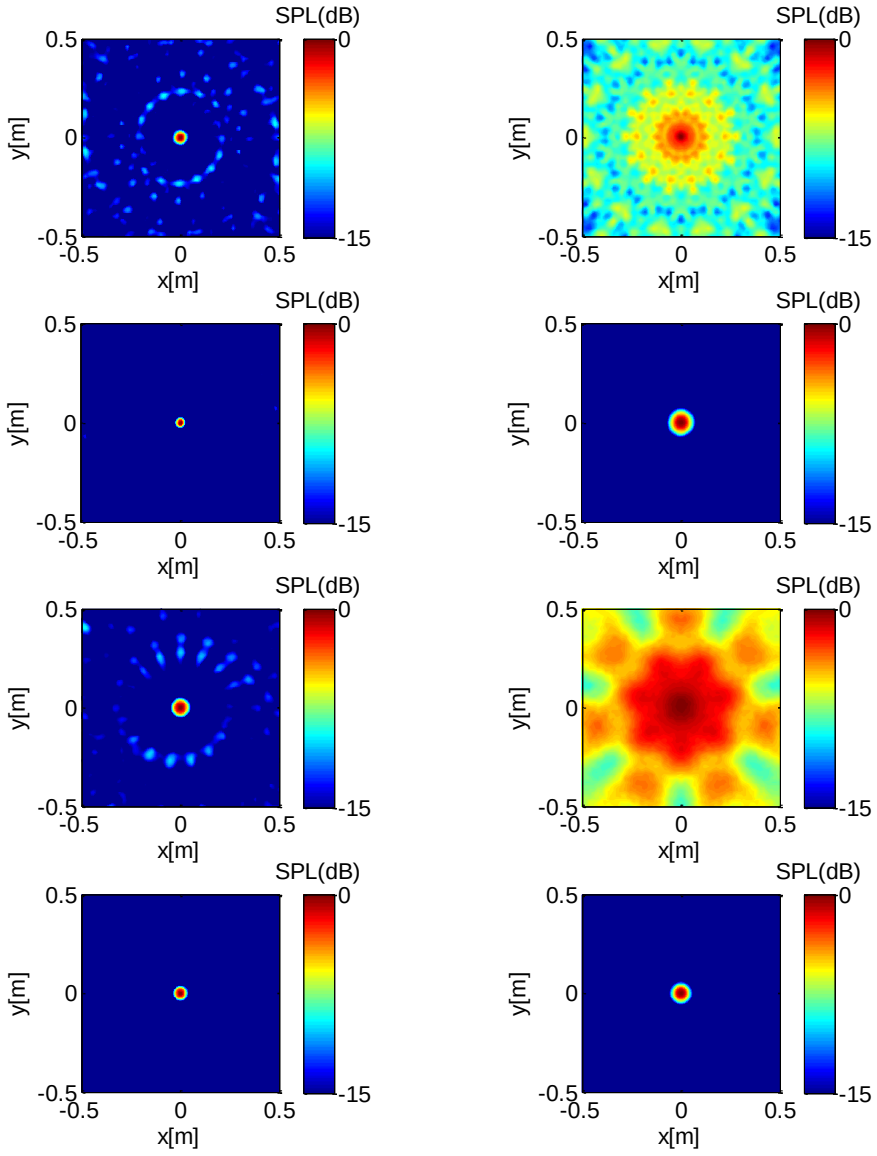

Figure 4.40: Summary of the numerical results for the monopole source validation case. Left column: Archimedean spiral array; Right column: Star array. First row: plane wave incidence acoustic beamformer; Second row: plane wave incidence acoustic beamformer with diagonal removal; Third row: spherical wave incidence acoustic beamformer; Last row: spherical wave incidence acoustic beamformer with diagonal removal.

In summary, good agreement for the acoustic maps between the experiment and numerical calculations of the acoustic beamforming tests provided some validation of the in-house acoustic beamforming solver used in the CAB method for noise source identification with two microphone array patterns (Archimedean spiral array and star array) under both plane wave incidence and spherical wave incidence scenarios. This provides confidence for the application of our in-house acoustic beamformer solver for subsequent validation and application cases.

Chapter 5 Validation of the Computational Acoustic Beamforming Method—Whole System Level

This chapter presents the validation of the CAB method on a whole system level using the case of the flow over a NACA 0012 airfoil. For this case, the numerical predictions agreed exceptionally well with the wind tunnel measurements, providing confidence in the ability of the CAB method for the identification of sound source locations on noise generating objects (e.g., wind turbine, airfoil, etc.). The CPU hours used for this validation case are summarized in Appendix III.

5.1 Experiment Setup of the NACA 0012 Airfoil Trailing Edge Noise Validation Case

An experimental aeroacoustic analysis of NACA 0012 airfoil conducted by NREL was selected for the validation of the CAB method on a whole system level. This experimental campaign also included six other airfoils that were candidates for use on small wind turbines. The goal of the experiment was to understand the aerodynamic and aeroacoustic performance of these airfoils at low-Reynolds numbers which were the operating Reynolds numbers appropriate for small wind turbines. The experiment was conducted at the Netherlands National Aerospace Laboratory (NLR) in Emmeloord, Netherlands [140].

The tests were carried out in NLR's small anechoic wind tunnel KAT. Figure 6.1 shows the KAT set up for the airfoil noise measurements. The microphone array consisted of 48 LinearX M51 microphones mounted in an open grid and was designed for maximum side-lobe suppression at frequencies between 1 kHz and 20 kHz. The array had dimensions of 0.8 m × 0.6 m. The microphone array was placed outside the tunnel flow at a distance of 0.6 m from the tunnel axis as shown in Figure 5.1 and 5.2. The center of the microphone array was placed at the same height as the tunnel axis. The array sampling frequency was 51.2 kHz for a measurement period of 30 s [140].

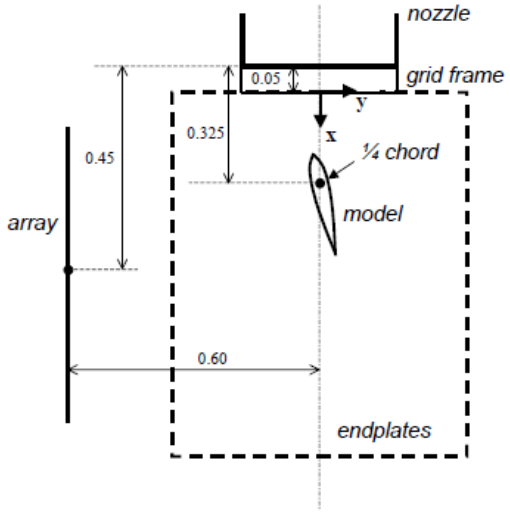

Figure 5.1: Top view of KAT setup for NACA 0012 airfoil noise measurements. The origin of the z-axis is located at the tunnel axis. Dimensions in meters (not to scale) [140].

Figure 5.2: KAT setup with lined endplates and microphone array [140].

The acoustic beamformer used in the experiment was a conventional delay-and-sum acoustic beamformer with the main diagonal eliminated in the cross-power matrix. The resulting acoustic images were plotted at the airfoil model plane as shown in Figure 5.3 with 0.5 cm spatial resolution in both directions. The acoustic images were produced in one-third-octave bands.

The tested NACA 0012 airfoil provided by NREL has a chord length of 0.2286 m and a span length of 0.509 m. The airfoil trailing edge thickness is less than 0.225 mm. The validation case had no trip applied on the airfoil surface and the airfoil was placed at zero degree AOA. The values of two non-dimensional parameters were $Re = 0.62\times10^6$ and $Ma = 0.12$ during the measurements. The simulation uses these same values for Re and Ma numbers.

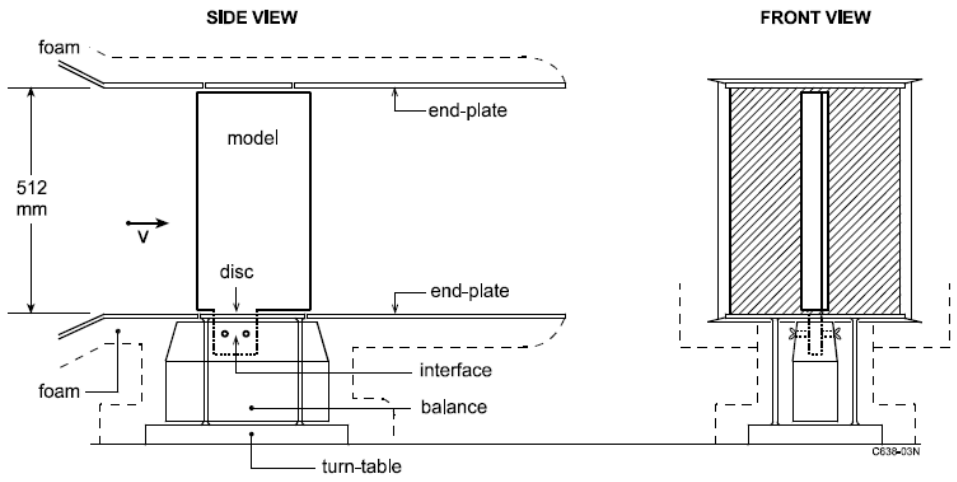

Figure 5.3: Experimental setup for NACA 0012 airfoil trailing edge noise case [140].

Five acoustic maps for the frequency range from 2000 to 5000 Hz were obtained in the experimental measurements for the NACA 0012 airfoil. This information was used for the identification of the sound source location on the airfoils. The details of the experimental procedure are described in [140]. Because no aerodynamic experimental data were available for the NACA 0012 airfoil measurements reported in [140], two other experiments [141], [142] were selected to provide data that can be used to compare the observed pressure, lift, and drag coefficients with the numerical predictions. The aerodynamic data from these two experiments were conducted at an inlet Mach number $Ma = 0.15$ (in comparison with an inlet Mach number of $Ma = 0.12$ for our simulation) and at Reynolds numbers in the range $1.44\times10^6 \leq Re \leq 9\times10^6$ (in comparison with a Reynolds number of $Re = 0.62\times10^6$ for our simulation).

5.2 Numerical Setup of the NACA 0012 Airfoil Trailing Edge Noise Validation Case

5.2.1 Geometry and Mesh

The computational domain has dimensions of $10C$ in the streamwise direction with $4C$ upstream of the airfoil and $6C$ downstream of the airfoil, $6C$ in the wall normal direction and $0.14C$ in the spanwise direction where C is the airfoil chord length.

Twenty prism layers were generated around the airfoil with a layer stretch ratio of 1.2. The resulting non-dimensional wall distance had the value of $y^+ \leq 1$ (recall $y^+ \equiv u_\tau y/\nu$ where u_τ is the friction velocity and ν is the kinematic viscosity of the fluid). A dense mesh was created surrounding the airfoil as shown in Figure 5.4. An increased spatial resolution was applied around the airfoil trailing edge and wake regions as shown in Figure 5.4 (b). A total of 3.6 million grid nodes were generated in the computational domain.

There is a rectangle surrounding the airfoil representing the permeable integration surface. The impermeable integration surface coincided with the airfoil wall boundary. The sound source data obtained on the permeable and impermeable integration surfaces were employed subsequently in the FW-H acoustic calculations, using the permeable and impermeable formulations, respectively.

(a) 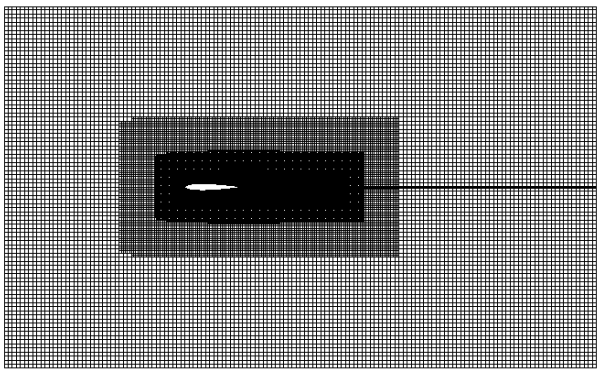 (b) 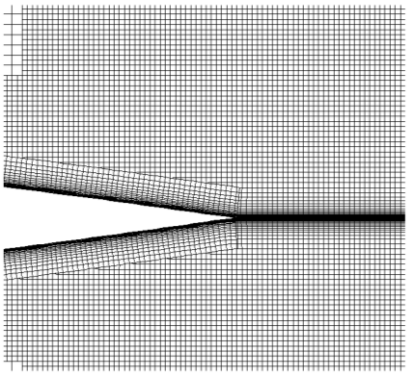

Figure 5.4: Computational mesh used for the aerodynamic simulation of the NACA 0012 airfoil: (a) mesh for the whole computational domain and (b) mesh around the airfoil trailing edge.

In a typical LES, the span width of the airfoil used in the simulation is only a small fraction of the actual airfoil span width due to the limited available computational resources. Nevertheless, the span width in the simulation needs to be equal to or larger than the coherence length in order to correctly predict the frequency spectrum of the sound pressure radiated from the entire span. If this constraint is verified in the simulation, the individual source regions in the computational domain radiate in a statistically independent manner and the total noise spectrum is then simply the sum of contributions from n independent source regions along the span [143], where

$$n = \frac{\text{actual airfoil span width}}{\text{simulated airfoil span width}}. \quad (5.1)$$

Kato et al. [144] discussed this issue in their calculation of noise from a cylinder wake. Wang [143] conducted research on this issue using a flat strut with an asymmetrically beveled trailing edge at zero-degree angle of attack. The relation between the spanwise

coherence of the fluctuating surface pressure and the span width at certain frequencies is shown in Figure 5.5, where Δx_3 is the span width, U_{ref} is the inlet velocity and h is the maximum thickness of the airfoil. In the flow over the NACA 0012 airfoil, $\Delta x_3 = 0.14C$ and $h = 0.12C$, which implies that $(\Delta x_3)/h = 0.14C/0.12C = 1.17$. According to Figure 5.5, the span width used in our simulation is longer than the coherence length required for a non-dimensional frequency of $\omega h/U_{ref} \approx 4.354$, which corresponds to a frequency range of 1000 Hz and above. This is the typical frequency range for airfoil trailing edge noise which is the main noise mechanism for the current validation case.

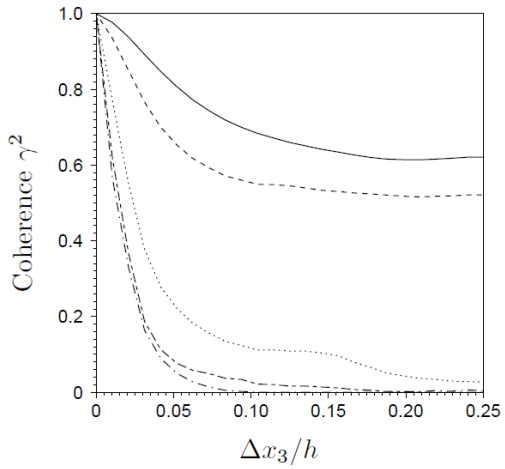

Figure 5.5: Spanwise coherence of the fluctuating surface pressure on the upper surface near the trailing edge at frequencies $\omega h/U_{ref} \approx 1.75$ (solid line), 3.51 (dashed line), 5.26 (dotted line), 7.01 (long-dashed short-dashed line), 8.76 (dashed dotted line) [143].

5.2.2 CFD Simulation Settings and Boundary Conditions

The LES solver described in Section 3.2.2.2 was used with the Smagorinsky subgrid-scale model [114] and the standard Van Driest damping function [115] for the flow field simulation of this validation case. The three-dimensional unsteady Navier-Stokes

equations were solved using a cell-centered finite volume method. The hybrid Gauss-LSQ (least-squares) cell based scheme was chosen with the Venkatakrishnan limiter for the gradient approximation of all quantities used in the discretization of the governing equations. A bounded central differencing scheme was employed for discretization of the convective term in the momentum equation. A pressure-weighted interpolation scheme was used to estimate the pressure values at the cell faces from their values at the cell centroids. A collocated variable arrangement was used and the SIMPLE method was employed for the pressure velocity coupling. A second-order implicit scheme was chosen for the time marching algorithm with a fixed dimensionless time step of $t^* = 0.0017$, where the dimensionless time step was defined as $t^* = tU_{ref}/C$. With the choice of this time step, the average CFL number was kept below a value of 1 within the entire computational domain. In the solution of the discretized equations, a maximum of 50 iterations was permitted for each time step.

A uniform velocity distribution was prescribed at the inlet of the computational domain with an inlet Mach number of 0.12. The pressure at the outlet boundaries of the domain was set to atmospheric pressure. The airfoil surfaces were treated as no-slip smooth walls. The top and bottom boundaries of the computational domain were treated as symmetric planes. Periodic boundary conditions were applied at the front and back surfaces of the computational domain.

5.2.3 Acoustic Propagation Settings

The impermeable and permeable formulations of the FW-H equation were used for this validation case. The impermeable formulation used the sound source data on the airfoil surface (which was chosen as the impermeable surface for this application). The permeable formulation utilized sound source data on a rectangular box which contains the airfoil (chosen as the permeable surface in this application). The time derivative terms in both the impermeable and permeable FW-H formulations were evaluated by two discretization schemes: the CDS and Stirling scheme as stated in Section 3.3.

A total of 153 microphones were used as the receivers in the acoustic calculation. Of these microphones, 66 were used to form an Archimedean spiral array and 63 were used to form a star array. These arrays were placed at the same location relative to the airfoil as was used in the wind tunnel experiment. The remaining 24 microphones were placed uniformly along a circle surrounding the airfoil at a radius of 5 m in the simulation as illustrated in Figure 5.6 in order to investigate the directivity of the airfoil trailing edge noise.

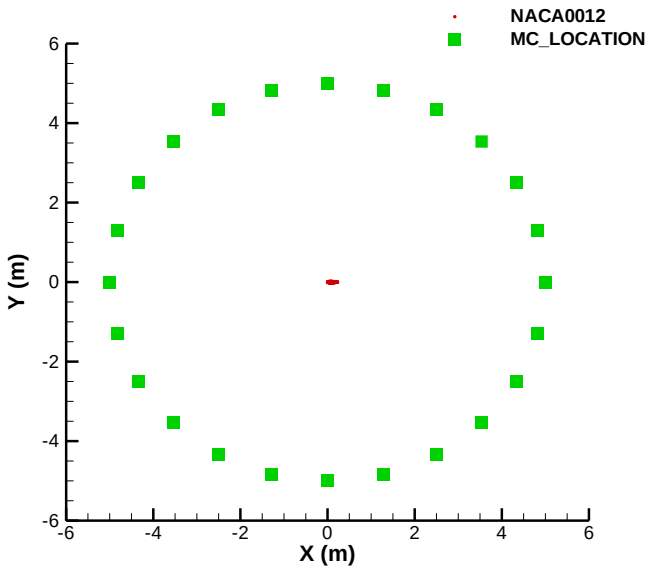

Figure 5.6: Sketch of microphones locations for the airfoil directivity calculation: 24 microphones were evenly located on a circle with 5 m radius surrounding the airfoil.

The spanwise periodic extension was also investigated in this validation case where the airfoil span width was periodically extended to five times of the airfoil span width used in the CFD simulation. The acoustic results with and without the periodic extension of the airfoil in the spanwise direction were used in the acoustic beamforming calculation in order to evaluate the effect of the spanwise periodic extension on the resulting acoustic maps.

5.2.4 Acoustic Beamforming Simulation Settings

Owing to the fact that the microphone array geometry employed in the NACA 0012 airfoil experiment [140] was not described in detail, two different arrays were used in our simulations. The geometry for these two arrays was as follows: (1) an Archimedean spiral array consisting of 66 microphones and (2) a star array consisting of 63

microphones. The microphone arrays used in our simulation have dimensions of 0.8 m × 0.8 m and were similar in size to the array used in the wind-tunnel experiment which had a dimension of 0.8 m × 0.6 m [140]. These two microphone arrays, which were placed at the same location as in the experiment [140], are centered at a distance of $C/4$ along the airfoil chord and at a distance of around 0.6 m away from the source plane as shown in Figure 5.7. The array sampling frequency was 100 kHz and the data recording period was 0.5 s during the simulation.

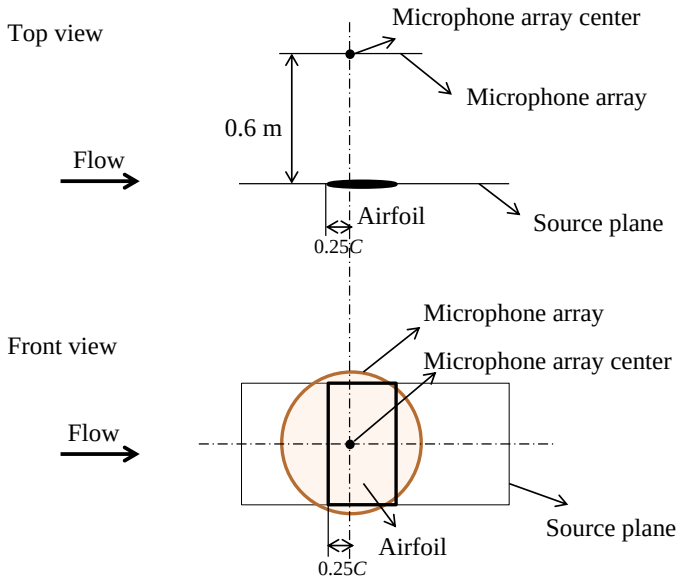

Figure 5.7: Sketch showing the location of the microphone array and the source plane used for the aeroacoustic simulation of the NACA 0012 airfoil.

The spherical wave incidence acoustic beamformer with and without the inclusion of the diagonal removal process were used for the acoustic beamforming calculation.

The acoustic images were computed at the source plane with 3 mm spatial resolution in the spanwise direction and 7 mm spatial resolution in the streamwise direction, in conformance with those measured in the wind-tunnel experiment [140]. As in the case of the acoustic images measured in this experiment, the acoustic maps obtained using the CAB methodology were frequency averaged over one-third octave bands. The determination of the center frequencies and the upper and lower frequency boundaries (the band width) that define each one-third octave band can be found in [139]. An arithmetical average is used to calculate the averaged sound pressure level within each one-third octave band. The dimensions of the simulated acoustic images are $3C \times 0.7C$.

5.3 Numerical Results and Analysis of the NACA 0012 Airfoil Trailing Edge Noise Validation Case

5.3.1 Flow Field Results and Analysis

Figure 5.8 shows the lift and drag coefficients time history for the tested NACA 0012 airfoil obtained from our simulations. The lift and drag coefficients of this airfoil are calculated in accordance to

$$c_L = \frac{L_a}{\frac{1}{2}\rho U_{ref}^2 S_a}, \tag{5.2}$$

$$c_D = \frac{D_a}{\frac{1}{2}\rho U_{ref}^2 S_a}, \tag{5.3}$$

where L_a and D_a are lift and drag force applied on the airfoil surface, S_a is the frontal area which can be calculated from

$$S_a = C \times L_{span}, \tag{5.4}$$

where L_{span} is the spanwise dimension of the airfoil and C is the chord length.

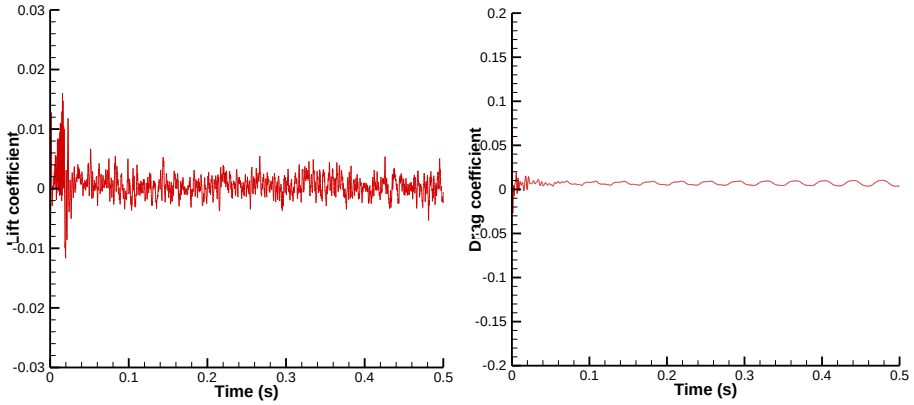

Figure 5.8: Lift (left) and drag (right) coefficients time history for the NACA 0012 airfoil at zero degree angle-of-attack.

The predicted lift (c_L) and drag (c_D) coefficients for the NACA 0012 airfoil at zero-degree AOA are compared with two observed results obtained in two experiments [141], [142] as summarized in Table 5.1. A perusal of Table 5.1 indicates that there is good agreement between the predicted time-averaged lift and drag coefficients and the corresponding measured quantities obtained from the two experiments. Note that the predicted lift coefficient of the airfoil is not zero as shown in Table 5.1. This might be due to the fact that the length of the data obtained from the flow field simulation is not long enough to average out the transient effects on the airfoil surface.

Table 5.1: Lift and drag coefficients comparison for NACA 0012 airfoil at zero-degree AOA.

	Experiment [141], [142]	Simulation (time averaged)
c_L	0	0.0105
c_D	(0.0060, 0.0082)	0.0065

Figure 5.9 compares the predicted mean surface pressure with the experimental data [141], [142]. Overall, the numerical prediction agrees very well with the experimental data, except perhaps around the region associated with the leading edge of the airfoil.

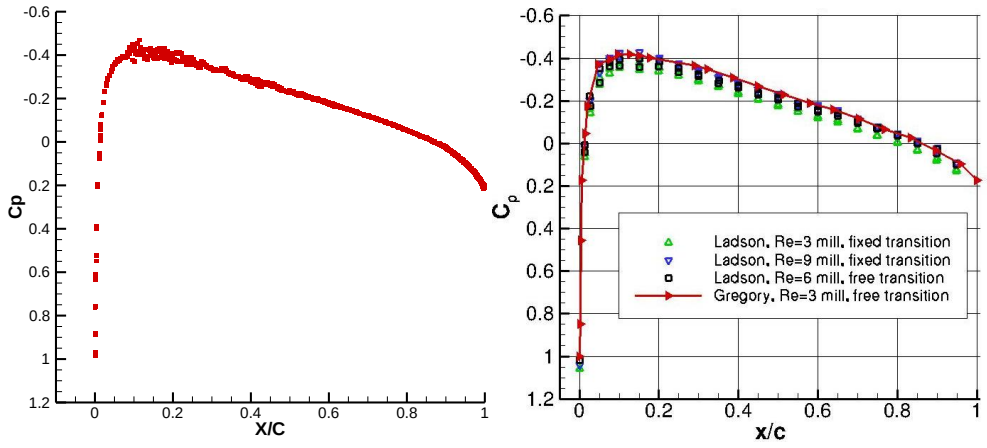

Figure 5.9: Mean airfoil surface pressure coefficient at zero degree angle-of-attack: predicted results (left) and experimental data (right). The upper triangle symbols

correspond to the experimental data from [142] at $Re = 3\times10^6$ with the transition fixed at the 5-percent-chord model station. The down triangle symbols correspond to the experimental data from [142] at $Re = 9\times10^6$ with the transition fixed at the 5-percent-chord model station. The square symbols correspond to the experimental data from [142] at $Re = 6\times10^6$ for a free transition. The right triangle symbols (with the solid line) represent the experimental data from [141] at $Re = 3\times10^6$ for a free transition.

The contours of the velocity magnitude, shown in Figure 5.10 (a), exhibit a symmetric distribution on the upper and lower surfaces of the airfoil. This result is in good agreement with other numerical results reported in the literature [145]. The streamlines around the trailing edge region of the airfoil are displayed in Figure 5.10 (b). A careful perusal of this figure indicates that small-scale turbulence is generated in the boundary layer along the airfoil surface and this turbulence is transported towards the trailing edge of the airfoil where it interacts with the flow in this region.

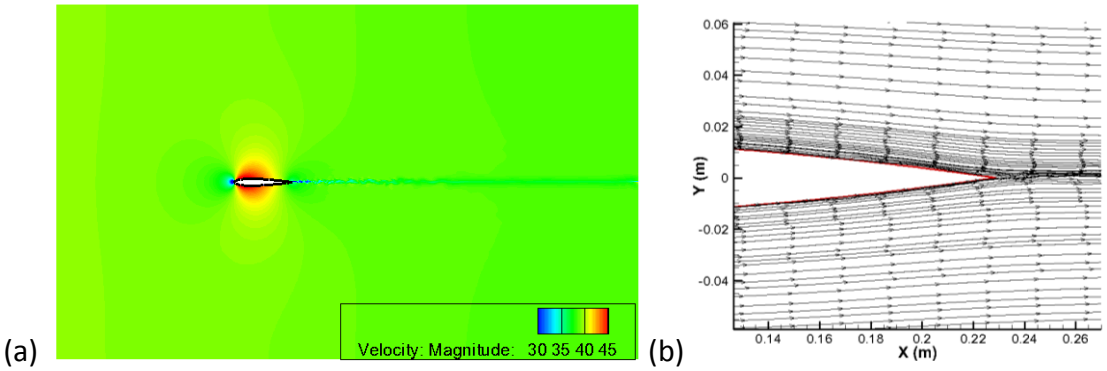

Figure 5.10: Predicted velocity magnitude contours and streamlines around the NACA 0012 airfoil: (a) velocity magnitude (m s^{-1}) contours and (b) velocity streamlines around the trailing edge region of the airfoil.

5.3.2 Acoustic Field Results and Analysis

Amiet [146] derived an analytical expression for the trailing edge noise directivity for a flat plate of chord length C. The characteristics of this theoretical directivity function for a number of non-dimensional frequencies in the plane normal to the trailing edge and on a sphere around the trailing edge source (in terms of the acoustic pressure in decibels) is shown in Figure 5.11 where C represents the airfoil chord length and λ represents the acoustic wavelength.

For the current NACA 0012 airfoil validation case, the airfoil chord length is 0.2285 m and the frequency range of interest is between 500 Hz and 3000 Hz, corresponding to a wavelength range between 0.12 m and 0.68 m. The resultant $C\ /\ \lambda$ is roughly between 0.4 and 2. This range covers the top two panels shown in Figure 5.11. It is expected that the directivity plot of the current NACA 0012 airfoil case is a combination of these two directivity plots. Indeed, the predicted directivity plot which is shown in Figure 5.12 reflects both the noise directivity features shown in the top two panels in Figure 5.11: a symmetric distribution of the SPL around the center horizontal plane with the highest SPL at 105 and 255 degrees.

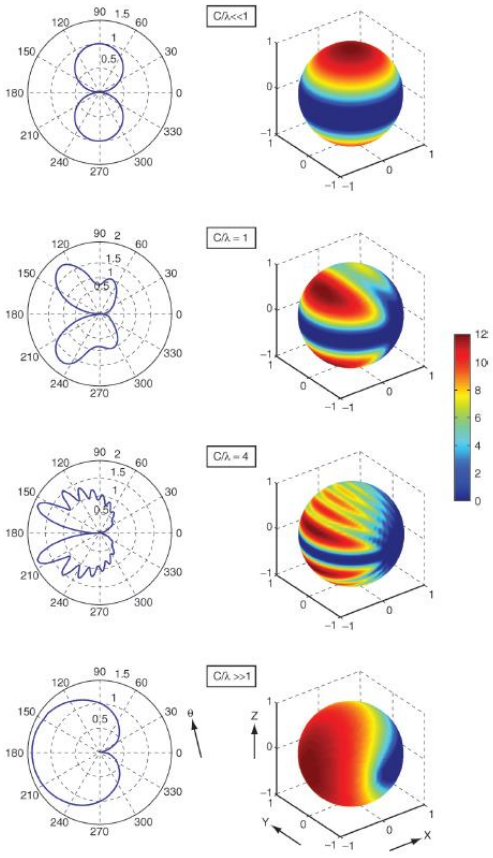

Figure 5.11: Theoretical trailing edge noise directivity for a flat plate of chord length of C for a number of non-dimensional frequencies in the plane normal to the trailing edge (left column) and on a sphere around the trailing edge source (right column) [63].

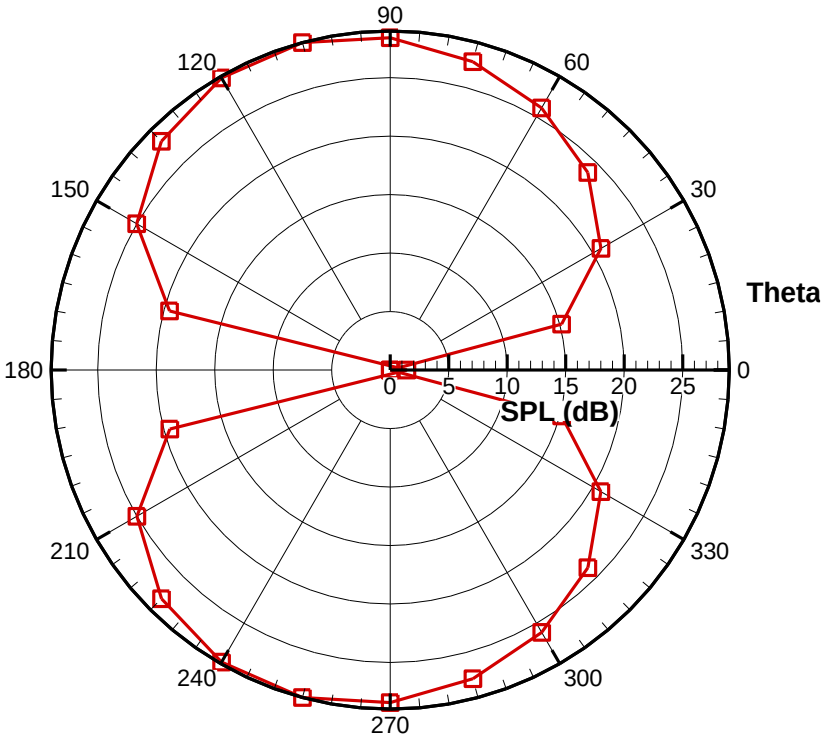

Figure 5.12: Numerical results of directivity plot for NACA 0012 airfoil validation case.

5.3.3 Acoustic Beamforming Results and Analysis

Figure 5.13 compares the predicted acoustic maps (right column) with the measured acoustic maps of the sound pressure level (SPL) obtained from an experiment described in [140] (left column) over the frequency range from 2000 to 5000 Hz inclusive for the NACA 0012 airfoil. These acoustic maps were produced using the impermeable FW-H formulation on an expanded span width (five times the span width used for the CFD simulation) with an Archimedean spiral microphone array. The CDS scheme was used to approximate the time derivatives in the acoustic propagation calculation. The diagonal removal process was not used in the acoustic beamforming calculation.

Despite the differences in the sizes and coordinates (the origins for the coordinates in simulation and experiment were chosen at different locations) of the acoustic maps shown in the left and right columns of Figure 5.13, the maps generated from the numerical simulation are in very good conformance with those generated from the experimental data. The CAB methodology predicts that the sound source is located right at the trailing edge of the airfoil for all the frequencies shown, which agrees well with the experimental measurements. Furthermore, the area of the region of maximum SPL in the acoustic maps decreases as the frequency increases, implying that a better spatial resolution of the source is obtained at the higher frequencies. The same phenomenon is also seen in the experimental results shown in the left column of Figure 5.13. This trend can be explained by consideration of the definition of the acoustic beamforming resolution [128]:

$$R_{BF} \approx 1.22 \frac{L}{\Pi} \lambda, \qquad (5.5)$$

where R_{BF} is the spatial resolution, L is the measurement distance, Π is the microphone array diameter, and λ is the wavelength of interest. From the relationship of Eq. (5.5), it is seen that the spatial resolution R_{BF} is proportional to the wavelength λ (or, equivalently, the spatial resolution is inversely proportional to the frequency f since $\lambda \equiv c/f$).

It is noted that the acoustic maps obtained from the numerical simulation provide a much larger dynamic range than those obtained from the experimental measurements. This implies that the acoustic maps obtained from the numerical simulations using the CAB methodology have a higher SNR than those obtained from the experimental measurements. This is not surprising given the fact that the experimental data are subject to various sources of noise (e.g., background noise) that is absent in the numerical data.

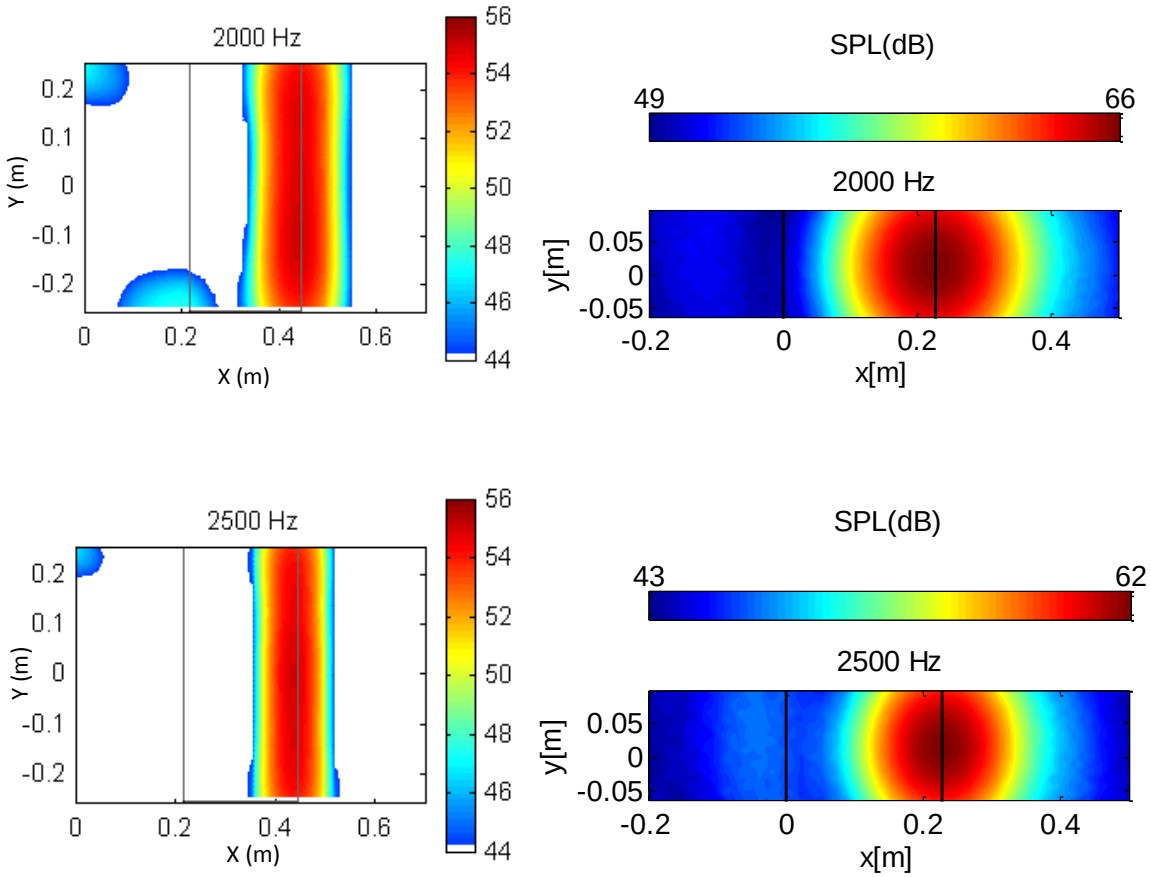

Figure 5.13: Acoustic maps for the NACA 0012 airfoil obtained from experimental measurements [140] (left column) and from the numerical simulation (right column).

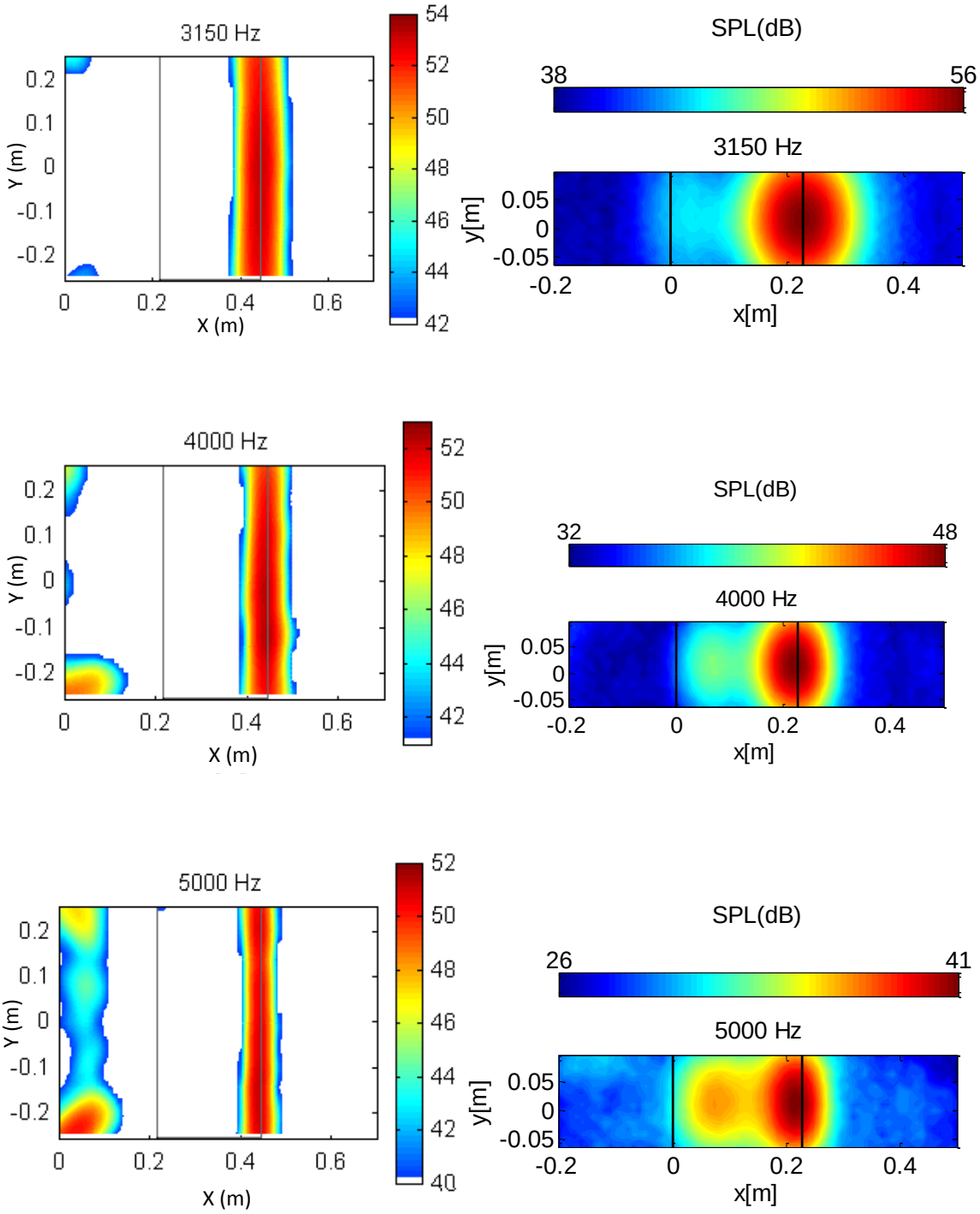

Figure 5.13 (continued)

In order to evaluate the effect of the different discretization schemes used on the time derivatives on the resulting acoustic maps, Figure 5.14 compares the acoustic maps obtained using the CDS scheme (left column) with those obtained using the Stirling scheme (right column) for the time derivatives in the acoustic propagation calculation. A comparison of the results in these two columns shows that the CDS and Stirling schemes yield almost identical acoustic maps. Overall, it is hard to differentiate the results using these two temporal discretization schemes. Due to the simplicity of the CDS, it will be used for the calculation of the results reported in the remainder of this thesis (unless otherwise indicated).

Next, the effect of using different formulations of the FW-H equation on the generation of acoustic maps is shown in Figure 5.15. The left column of Figure 5.15 exhibits the acoustic maps obtained using sound data generated by the impermeable formulation of the FW-H equation and the right column shows those obtained using sound data generated by the permeable formulation of the FW-H equation. It is seen that the sound pressure levels in the acoustic maps for the permeable formulation are larger than those for the impermeable formulation. The reason might be that the permeable surface encloses not only the sound source associated with the impermeable surface (airfoil surface), but also includes other sound sources such as those associated with turbulence in the vicinity of the airfoil trailing edge that are generated in the volume enclosed by the permeable surface lying outside the airfoil surface. As additional sound sources are included in the permeable integration surface, it is reasonable to expect

that the resulting acoustic maps would give higher sound pressure levels than those corresponding to the impermeable integration surface. In addition, the impermeable formulation (left column) predicts that the sound source is located right on the airfoil trailing edge center, which is in good conformance with the experimental results as shown in Figure 5.13. However, the predicted sound source location from the permeable formulation (right column) is situated below the airfoil trailing edge center and slightly downstream compared with the experimental results and that obtained from the impermeable formulation. This change in sound source location might be due to the computational resources limitation: a coarser mesh was used on and within the permeable sub-domain compared with the mesh used on the airfoil surface (impermeable surface). The decreased spatial resolution might diffuse and/or distort some sound sources generated on or within the permeable integration surface. This might cause the displacement of the predicted sound source location on the acoustic maps for the permeable formulation.

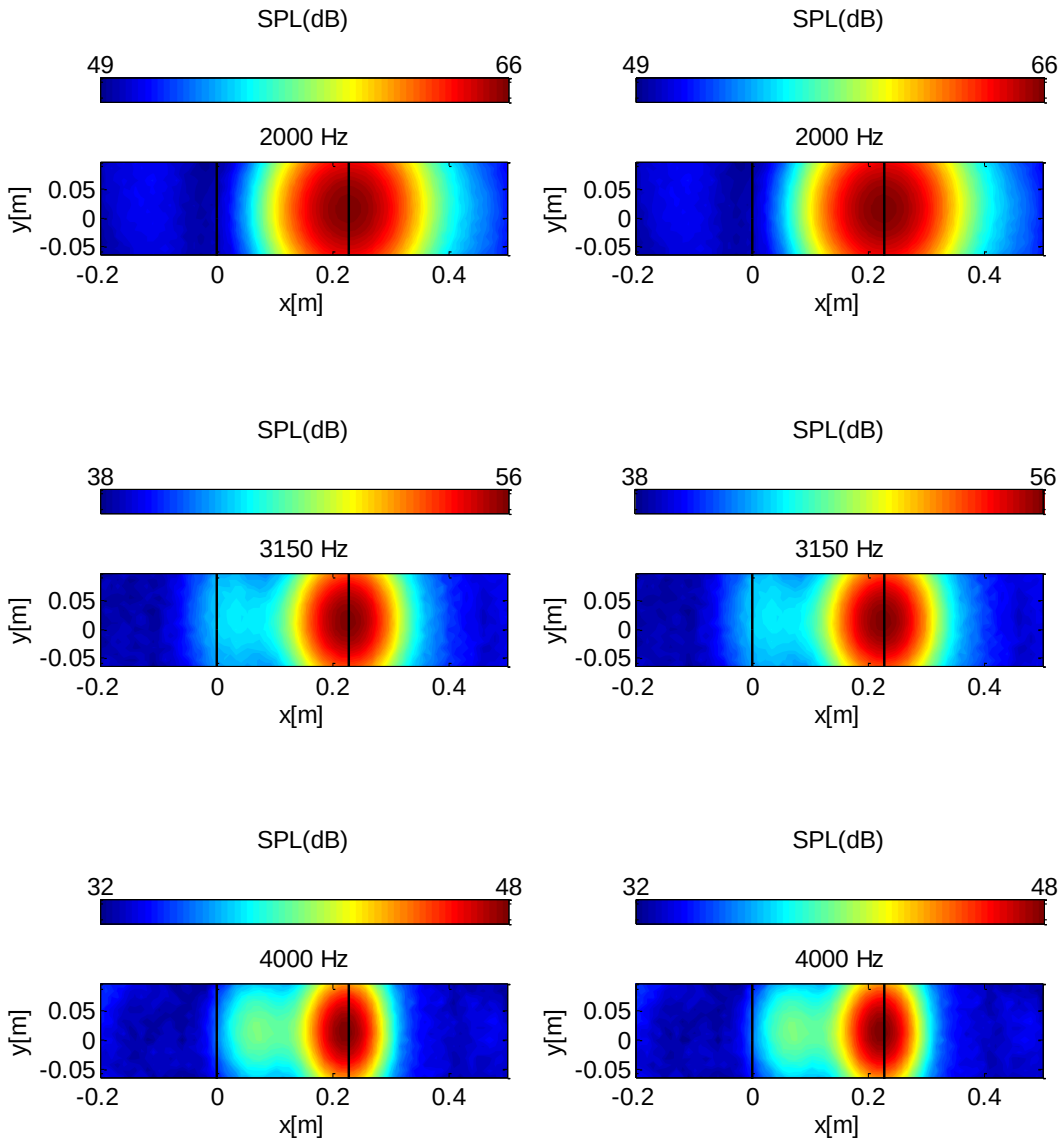

Figure 5.14: NACA 0012 airfoil acoustic maps obtained using two temporal discretization schemes: CDS scheme (left column) and Stirling scheme (right column).

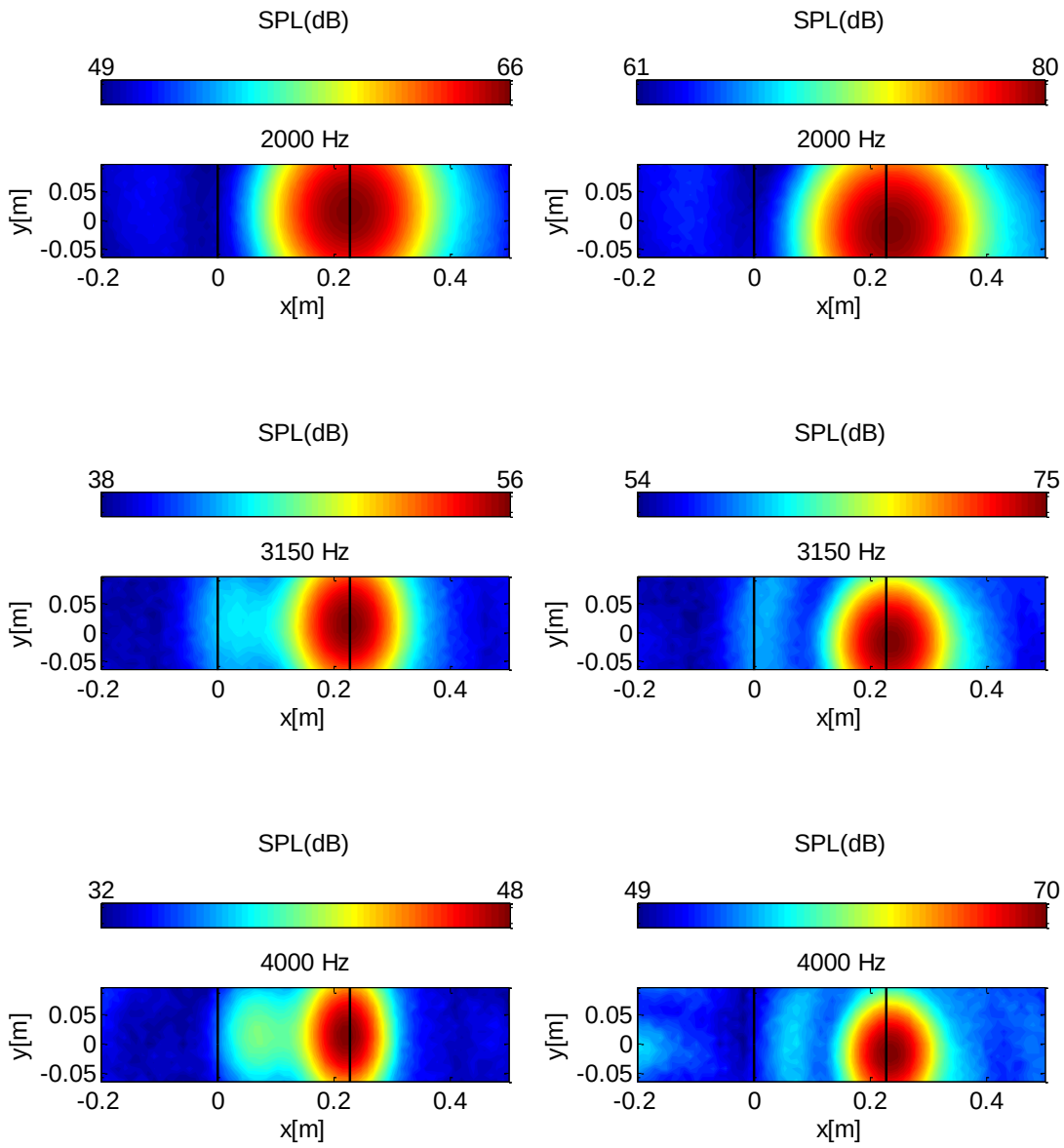

Figure 5.15: NACA 0012 airfoil acoustic maps obtained using the impermeable (left column) and the permeable (right column) of the FW-H formulations.

Continuing with the validation of the CAB methodology using the NACA 0012 airfoil, the author investigated the effect of the periodic expansion of the sound source information in the spanwise direction on the resulting acoustic maps. Figure 5.16 compares the acoustic maps obtained using the original sound source data derived from

the CFD simulations (left column) with those obtained by periodically extending the original sound source data five times in the spanwise direction. It is seen that both results predict the location of the trailing edge noise correctly compared with the experimental data as shown in the left column of Figure 5.13. In addition, the acoustic maps obtained from the original sound source data and from a periodic extension of this data are seen to have similar dynamic ranges. Nevertheless, it is seen that the acoustic maps generated for the periodic extension of the sound source (right column) have larger sound pressure levels than those for the original sound source (left column). Finally, an examination of Figure 5.16 shows that the detected noise source on the acoustic maps for the periodically extended sound source is elongated along the trailing edge of the airfoil, whereas the detected noise source on the acoustic maps for the original sound source appears to be circular in shape. In summary then, the acoustic maps provided by the periodically extended sound source are generally in better conformance with the experimental measurements than those for the original sound source.

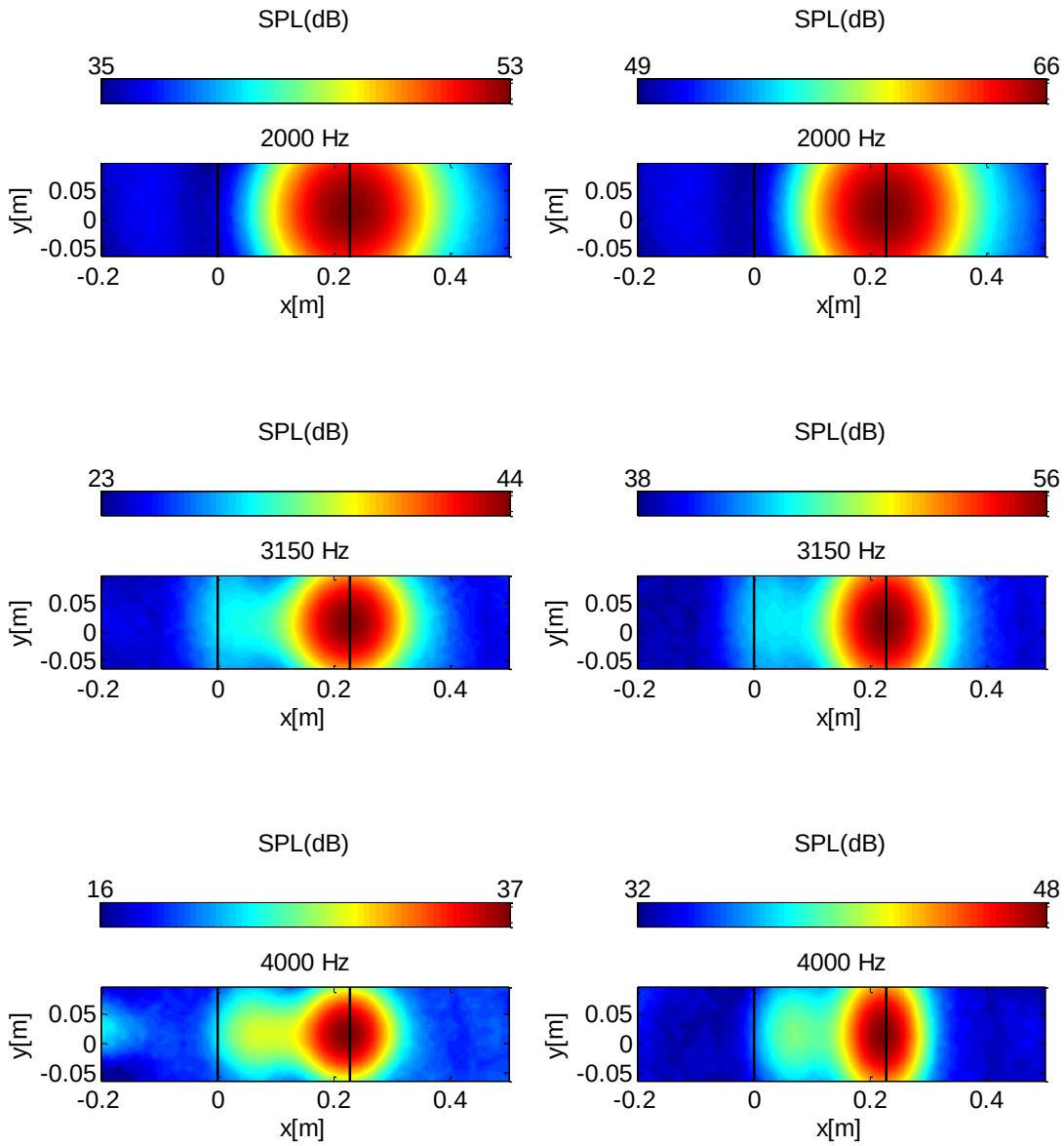

Figure 5.16: Predicted acoustic maps for the NACA 0012 airfoil obtained using the original sound source data (left column) and using a periodic extension of the original sound source data in the spanwise direction (right column).

Next, the author studied the effect of the inclusion of the diagonal removal process in the acoustic beamforming calculations on the generation of the acoustic maps. The left column of Figure 5.17 shows the acoustic maps obtained without the inclusion of the diagonal removal process in the acoustic beamforming calculations, whereas the right column of the Figure 5.17 shows the acoustic maps obtained with the inclusion of the diagonal removal process. The sound source locations on the acoustic maps obtained both with and without the inclusion of the diagonal removal technique in the acoustic beamforming are very similar. A perusal of the right column in Figure 5.17 shows that the use of the diagonal removal technique increases the dynamic range of acoustic maps as the frequency increases. A similar result regarding the increase of the dynamic range on acoustic maps obtained with the inclusion of the diagonal removal technique as the frequency increases has also been reported in the literature [18].

Furthermore, the area of the region of maximum SPL on the acoustic maps with the inclusion of the diagonal removal technique is slightly larger at the higher frequencies than those obtained without the inclusion of the diagonal removal technique. This shows that the diagonal removal process might worsen the acoustic beamforming spatial resolution while increasing the dynamic range. Although most of the investigations reported that the use of the diagonal removal technique improved the dynamic range on the acoustic maps, some investigators [16]-[18] suggest that caution needs to be taken in the inclusion of the diagonal removal technique in acoustic beamforming, especially for cases involving the identification of multiple sources. Since

the NACA 0012 airfoil results without the inclusion of the diagonal removal agreed very well with the experimental data and the diagonal removal technique is itself a computational demanding process in the acoustic beamforming component, the acoustic images reported henceforth in this thesis will be generated without the inclusion of the diagonal removal technique in the acoustic beamforming calculations.

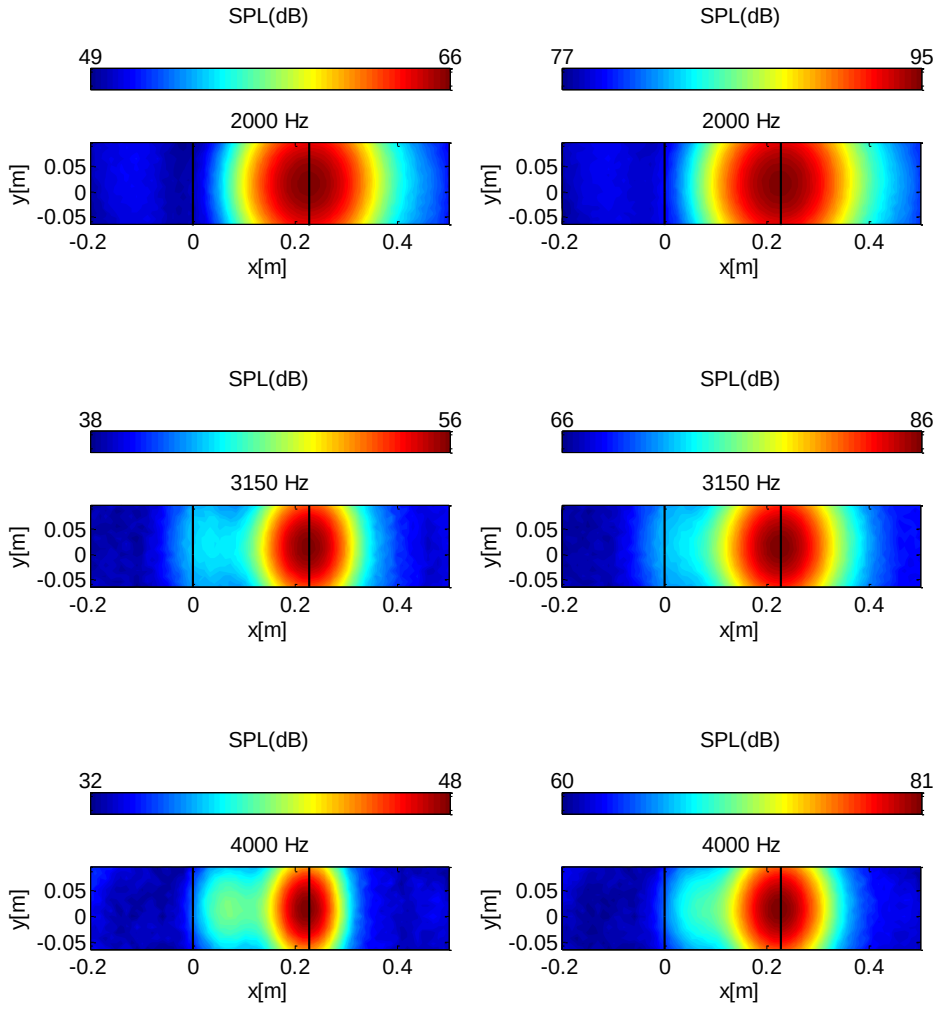

Figure 5.17: Predicted acoustic maps for the NACA 0012 airfoil obtained without (left column) and with (right column) the inclusion of the diagonal removal process in the acoustic beamforming calculations.

Finally, the author investigated the effect of different microphone array geometries on the generation of acoustic maps. The left column of Figure 5.18 displays the acoustic maps obtained for an Archimedean spiral array and the right column shows those obtained for a star array for a frequency range extending from 500 to 4000 Hz inclusive. Firstly, the acoustic maps for both microphone arrays identified the trailing edge of the airfoil as the location of the sound source, which agrees well with the experimental measurements (cf. left column of Figure 5.13). Consequently, both microphone array geometries yielded a correct identification of the noise source for the NACA 0012 airfoil. Secondly, at all the frequencies investigated, the sound source area predicted using an Archimedean spiral array is smaller than that predicted using a star array. This indicates that the Archimedean spiral array has better spatial resolution than the star array on the acoustic maps for the NACA 0012 airfoil. Thirdly, the dynamic range of the acoustic maps obtained for the Archimedean spiral array are slightly larger than those obtained for the star array for frequencies below 1000 Hz. At frequencies above 1000 Hz, a star array produces a much wider dynamic range in the acoustic maps than an Archimedean spiral array. This implies that an Archimedean spiral array results in a higher SNR for frequencies below 1000 Hz, but a lower SNR for frequencies above 1000 Hz, than a star array. Similar conclusions were reached in [15] where an aeroacoustic test of a larger NACA 0012 airfoil (longer span and chord length) was conducted experimentally.

It is stressed that there is no “universal” microphone array geometry that would produce optimal results vis-à-vis the acoustic beamforming for every case. For the

current application involving the identification of trailing edge noise from the NACA 0012 airfoil, an Archimedean spiral array generally resulted in a better spatial resolution, but a star array yielded a higher SNR at frequencies above 1000 Hz. However, it is not possible to conclude that one array performs better than the other because both arrays were found to provide correct predictions of the locations of the sound source for the various frequencies examined. In consequence, both array geometries will be used to generate acoustic maps for the identification of the source of wind turbine noise described in the next chapter.

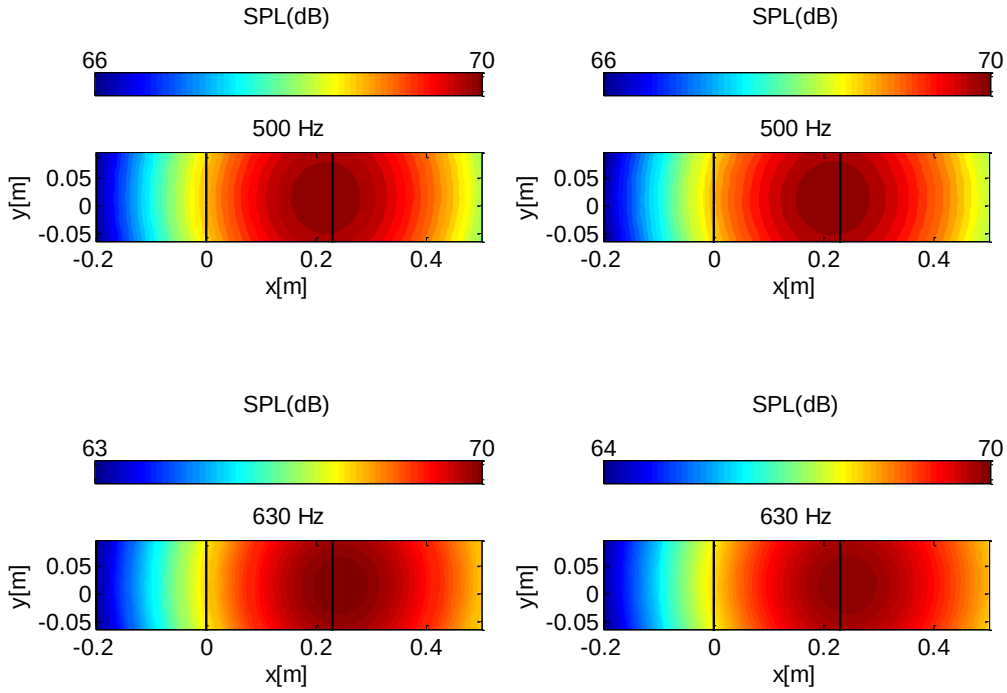

Figure 5.18: Predicted acoustic maps for the NACA 0012 airfoil obtained using an Archimedean spiral array (left column) and a star array (right column).

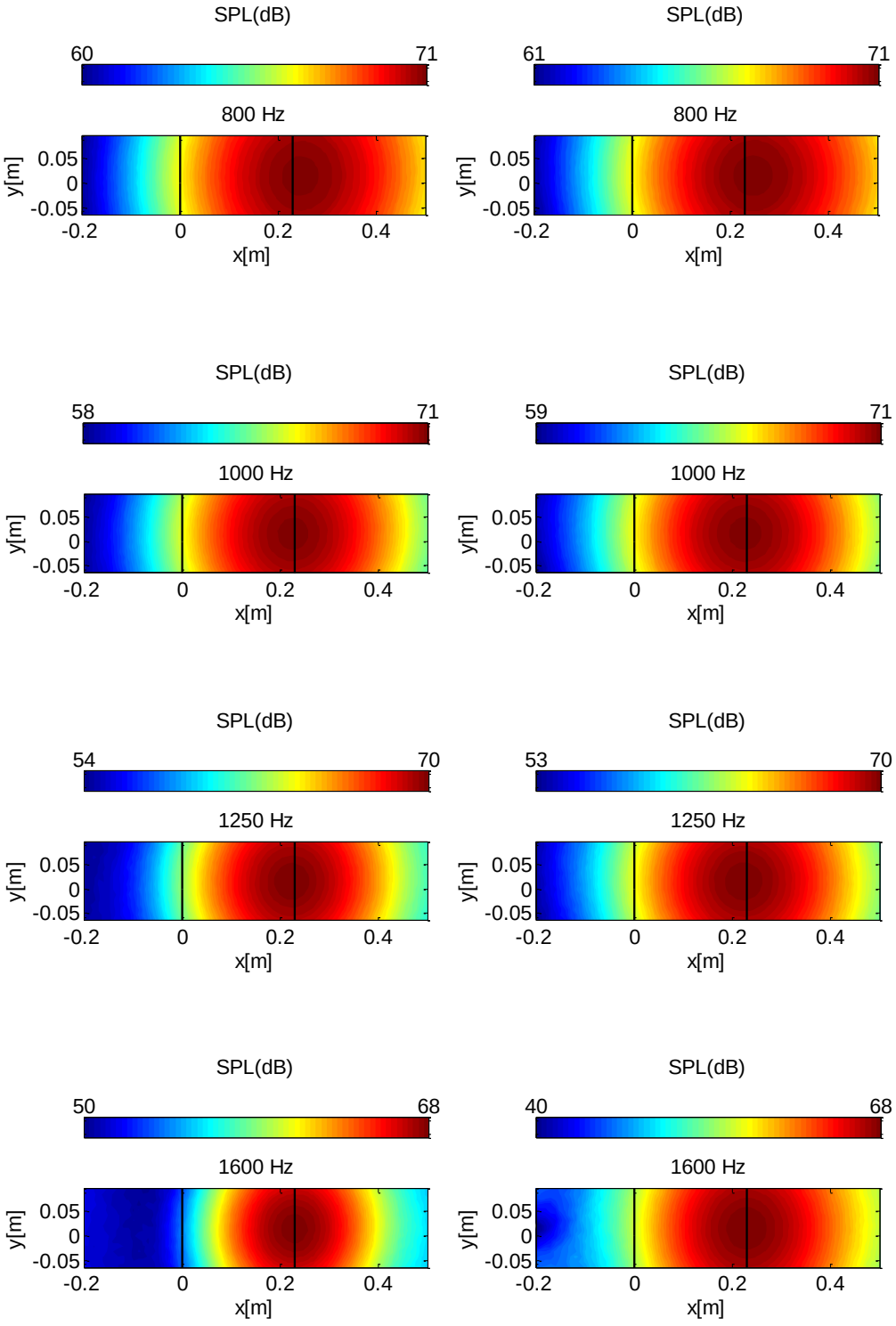

Figure 5.18 (continued).

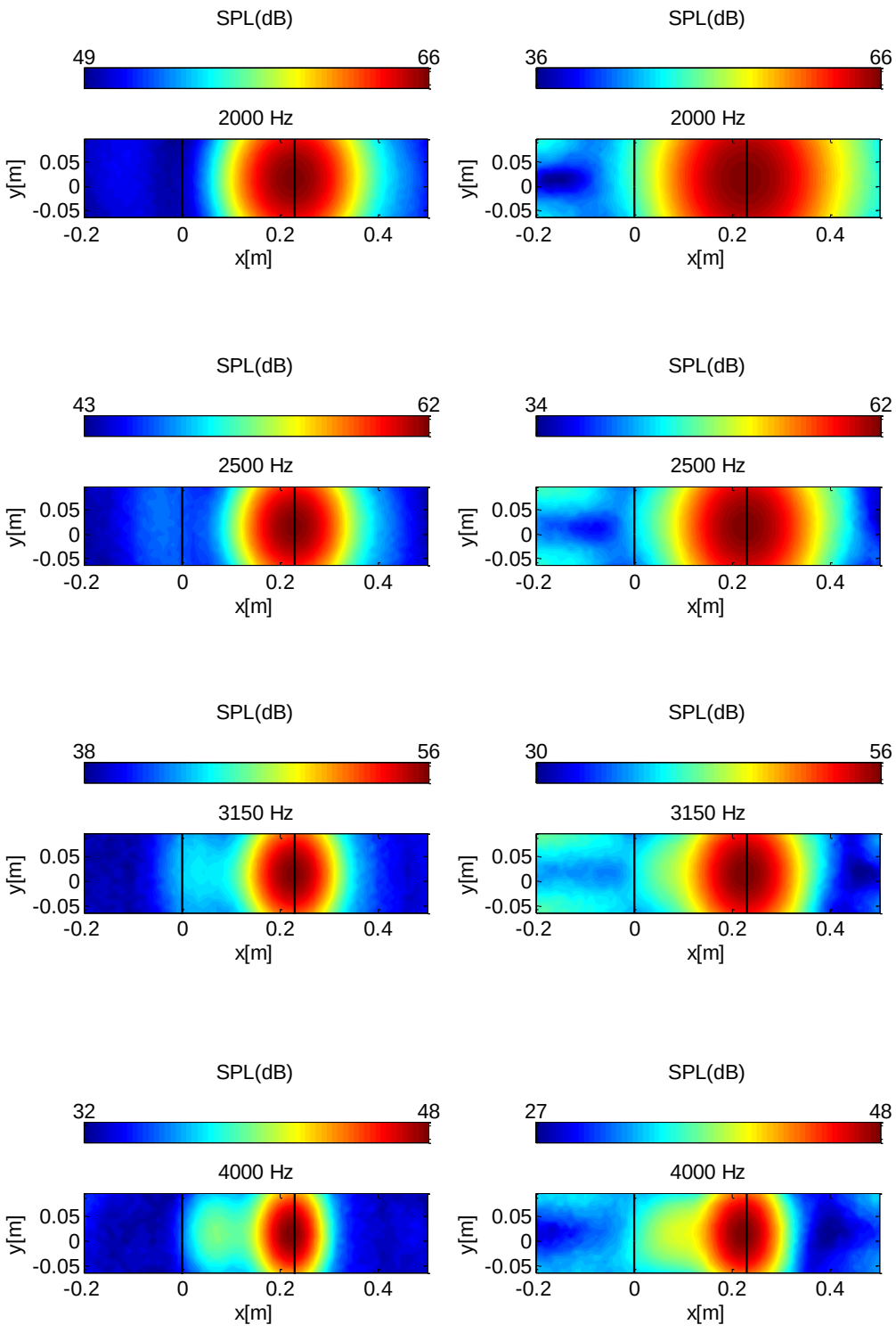

Figure 5.18 (continued).

Figure 5.19 compares the maximum SPL distribution over the frequency range between 500 Hz and 4000 Hz for five different configurations. These five configurations are:

1. Configuration 1: Archimedean spiral array, CDS used for the temporal discretization of the impermeable formulation of the FW-H equation, and acoustic maps generated using the periodically extended sound source data (the original sound source data derived from the CFD simulation was periodically extended five times in the spanwise direction);
2. Configuration 2: same as Configuration 1, except that the Stirling scheme was used for the temporal discretization;
3. Configuration 3: same as Configuration 1, except acoustic maps were generated using the original sound source data derived from the CFD simulation;
4. Configuration 4: same as Configuration 1, except that the permeable formulation of the FW-H equation was used; and,
5. Configuration 5: same of Configuration 1, except a star array was used.

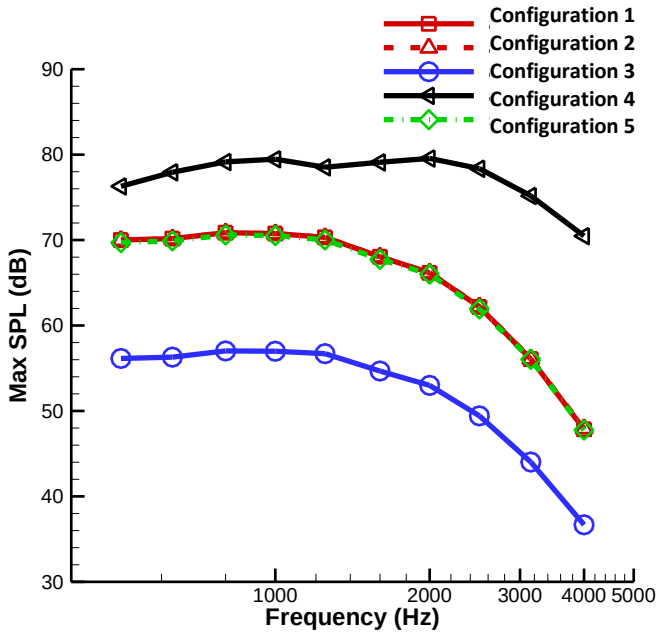

Figure 5.19: Max SPL vs. frequency for five different configurations of the CAB calculations.

Examining the results from these five configurations, it is found that the following two factors have an important influence on the SPL distribution over the frequency range between 500 Hz and 4000 Hz:

1. The FW-H formulation (impermeable and permeable); and,
2. The periodic extension of the sound source information in the spanwise direction (the original sound source data derived from the CFD simulation and the sound source data which is obtained by periodically extending the original sound source data five times in the spanwise direction).

It is seen that configuration 4 give the largest values for the maximum SPL. This is because the integration surface of the permeable formulation of FW-H equation

encompassed more volume than the integration surface used in the impermeable formulation. The inclusion of this extra volume surrounding the airfoil not only contributes to the higher level of the sound pressure on the acoustic maps, but also changes the distribution shape of the maximum SPL over the range of frequencies investigated, producing two small local maxima (bumps) at around 1000 Hz and 2000 Hz.

The SPLs obtained for the shorter span length (configuration 3) over the investigated frequency range are smaller than those obtained for the longer span length. This is reasonable because a longer span length incorporates more sound sources in the calculation, leading as such to larger sound pressure levels.

The predictions obtained from the CAB methodology provided good agreement with the experimental measurements obtained from the NACA 0012 airfoil (with respect to the flow field, the acoustic field, and the noise source identification using acoustic beamforming). Given this performance, it is expected that the CAB methodology can be used to identify the locations of noise sources in more complicated bodies such as a wind turbine.

Chapter 6

Application of the Computational Acoustic Beamforming Method to WINPhase 10 Wind Turbine Case

The predicted flow field and acoustic field for the WINPhase 10 wind turbine were validated with field measurement data in Sections 4.1.2 and 4.2.2, respectively. This chapter applies the acoustic beamforming component of the CAB methodology to the identification of noise sources on the WINPhase 10 wind turbine. The CPU hours used for this validation case are summarized in Appendix III.

6.1 Acoustic Beamforming Calculation Settings

Figure 6.1 sketches the numerical acoustic beamforming setup for the WINPhase 10 wind turbine. The center of the microphone array was placed upstream of the wind turbine at a distance of R_0 where $R_0 = H + \frac{D}{2}$ with H being the hub height and D being the rotor diameter [1], [3]. The acoustic beamforming plane coincides with the wind turbine rotor plane and has a size of 6 m × 6 m. The grid used for the acoustic beamforming has 121 points in both directions resulting in the generation of acoustic maps with 14,641 points. A spherical wave incidence acoustic beamformer was employed without the use of the diagonal removal process. The sampling duration

corresponds to three complete revolutions of the wind turbine rotor at three different reference wind speeds: 9 m s^{-1}, 10 m s^{-1} and 11 m s^{-1}. The sampling frequency is 10 kHz.

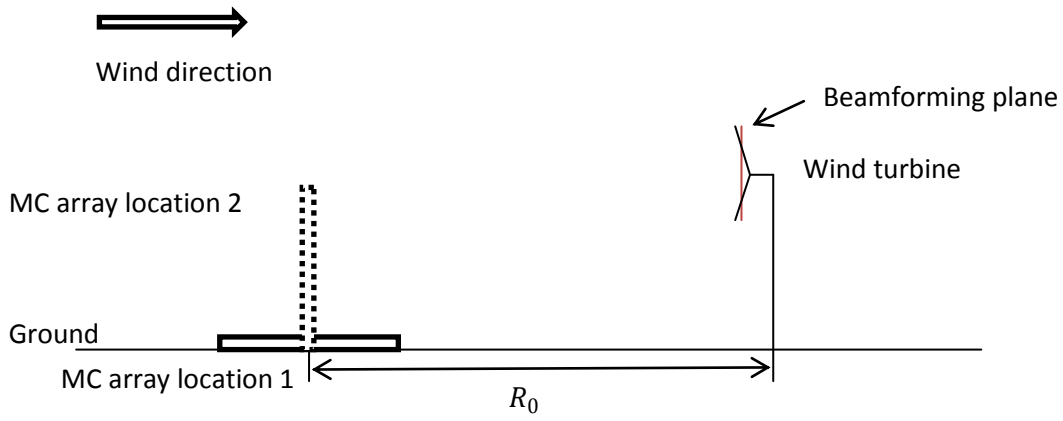

Figure 6.1: Sketch showing the locations of the microphone (MC) arrays used for acoustic beamforming for the WINPhase 10 wind turbine.

Two microphone array geometries (viz., Archimedean spiral array and star array) were used for the acoustic beamforming calculations for the WINPhase 10 wind turbine. Three scenarios were applied for each array geometry: namely, (1) an 8 m × 8 m horizontal array placed on the ground; (2) a 20 m × 20 m horizontal array placed on the ground; and, (3) a 20 m × 20 m vertical array oriented parallel with the wind turbine rotor plane.

6.2 Acoustic Beamforming Results and Analysis

The acoustic maps for three inflow reference wind speeds (9 m s^{-1}, 10 m s^{-1} and 11 m s^{-1} at the wind turbine hub height) were generated from the predicted sound signals at the microphones for two array geometries. Owing to the similarities of the acoustic maps

obtained for the three reference velocities at hub height, this section presents only the acoustic maps generated for a 9 m s^{-1} reference velocity. These maps were computed in the frequency range from 100 and 800 Hz for one-third octave bands. The results for an Archimedean spiral array and for a star array are exhibited in Figure 6.2 and Figure 6.3, respectively. The acoustic maps obtained for the other two reference velocities (10 m s^{-1} and 11 m s^{-1}) are shown in Appendix IV.

According to Eq. (5.5), at a fixed measurement distance, the spatial resolution of the acoustic map is proportional to the wavelength but inversely proportional to the array size. This dependence is evident from a careful perusal of the acoustic maps exhibited in Figures 6.2 and 6.3. For both the Archimedean spiral and the star arrays, the area of the identified sound source in the acoustic maps is seen to decrease as the frequency increases. This implies that the localization of the source is better resolved spatially as the frequency increases. Furthermore, the sound source is better localized spatially using the 20 m × 20 m array in comparison to that obtained using the 8 m × 8 m array (cf. the left and middle columns in Figures 6.2 and 6.3). As a consequence, it is seen that the spatial resolution of a putative sound source improves as the size of the microphone array increases. Similar conclusions were also reported in the literature [88] for experimental measurements.

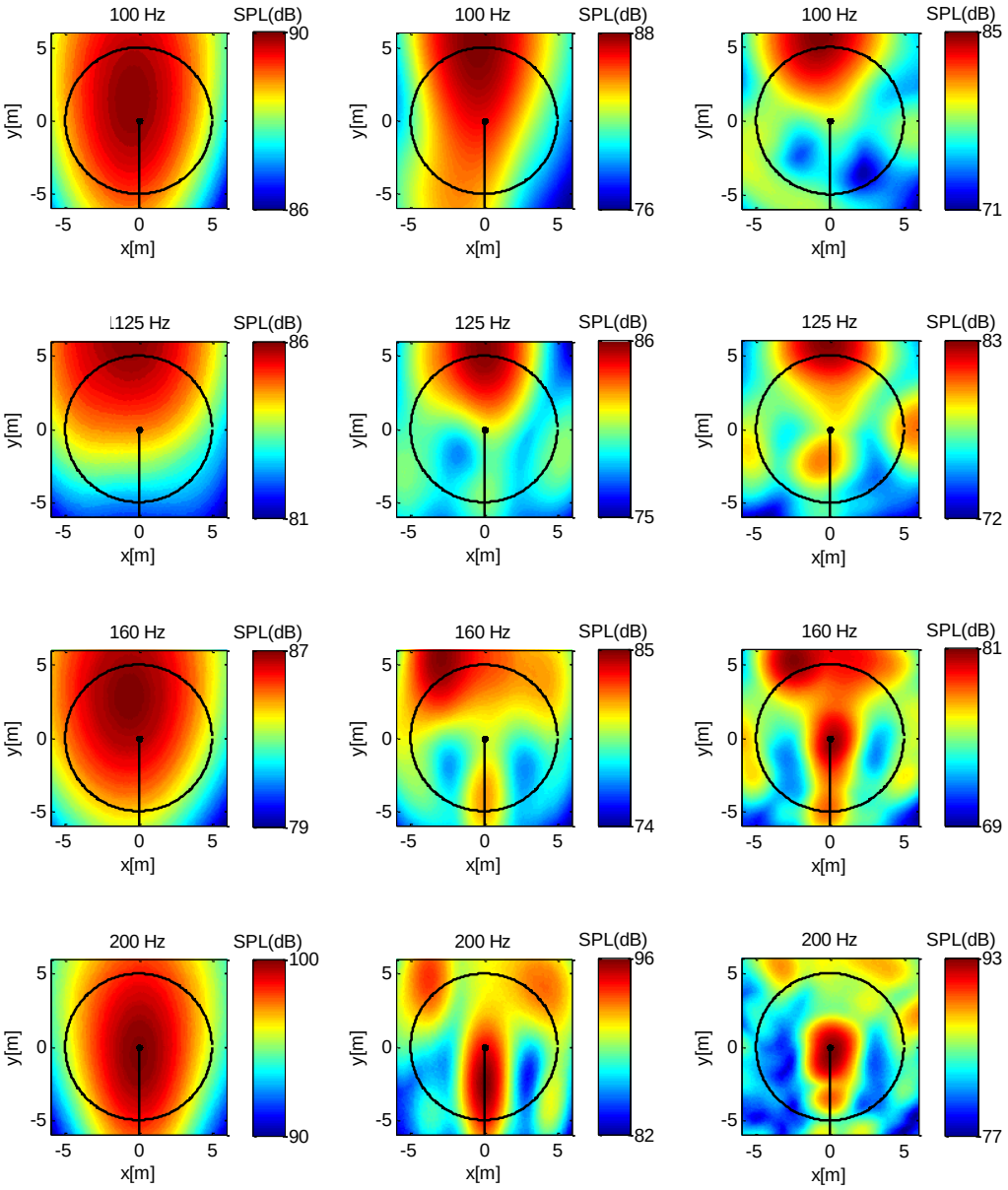

Figure 6.2: Numerical acoustic maps for the Archimedean spiral array: 8 m × 8 m horizontal array at ground level (left column); 20 m × 20 m horizontal array at ground level (middle column); 20 m × 20 m vertical array parallel to the wind turbine rotor plane (right column). The incidence wind speed is 9 m s^{-1}. The wind turbine rotates in the counter-clockwise direction.

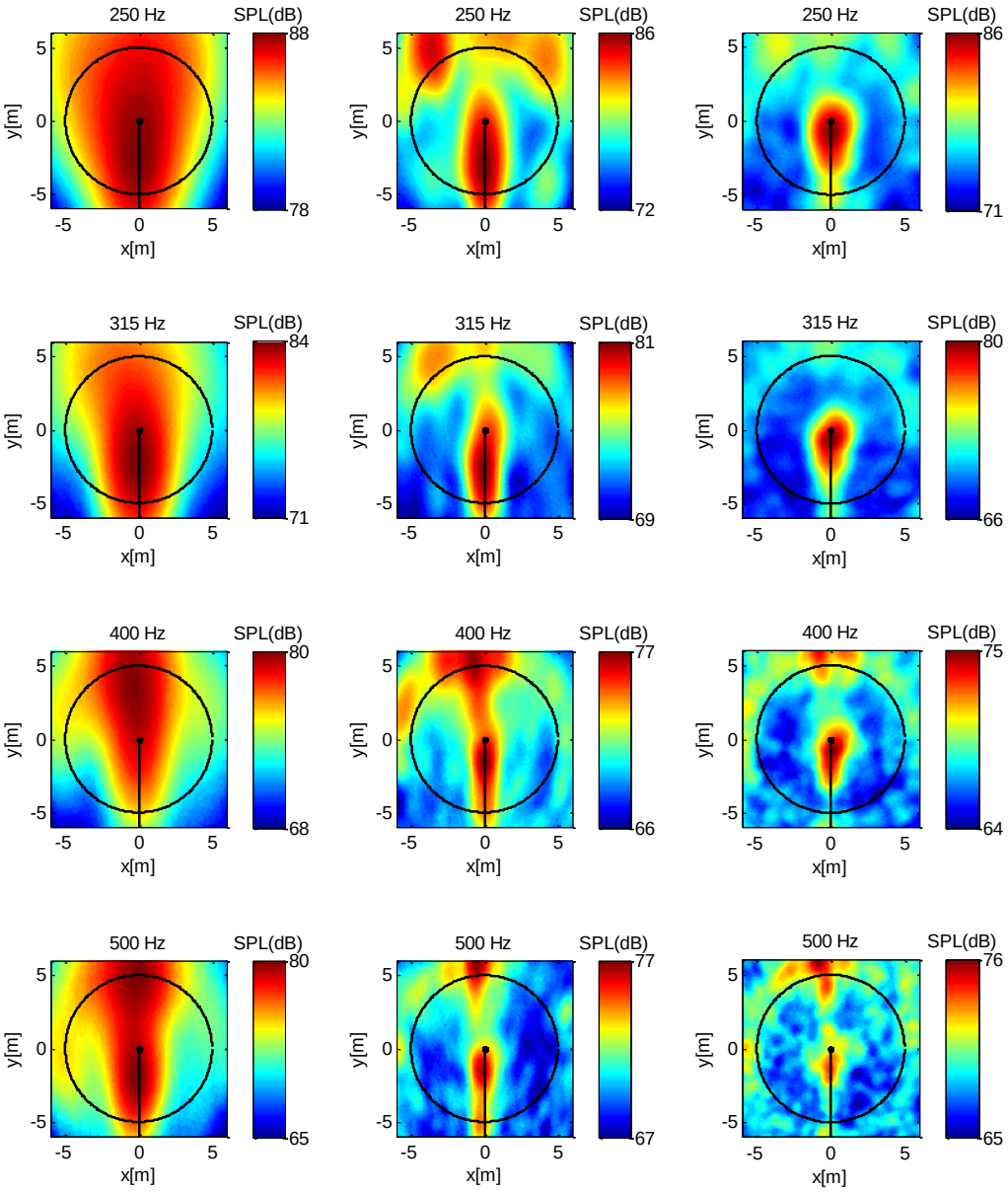

Figure 6.2 (continued).

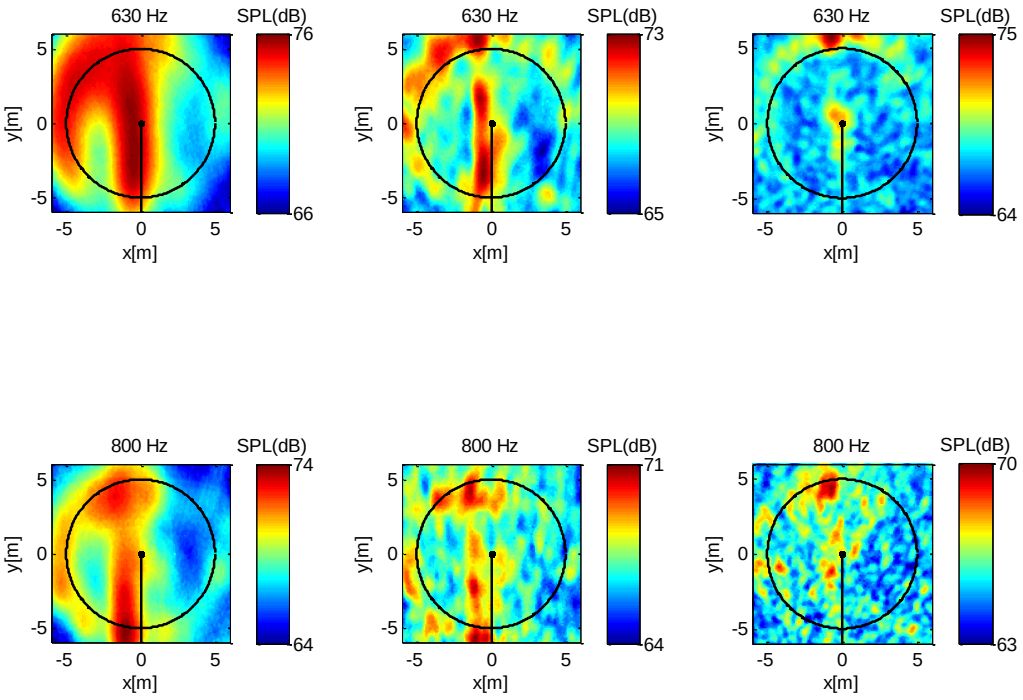

Figure 6.2 (continued).

For the NACA 0012 airfoil case investigated in Chapter 5, both the numerical results and the literature [15] suggest that an Archimedean spiral array provides a better spatial resolution of a sound source in the acoustic map than that obtained from a star array. This conclusion also holds for the current case involving a small wind turbine. More specifically, this is evident on comparing the acoustic maps in Figure 6.2 (Archimedean spiral array) with those in Figure 6.3 (star array). Nevertheless, the sound sources identified using both the Archimedean spiral and star arrays occur at similar locations in the acoustic maps.

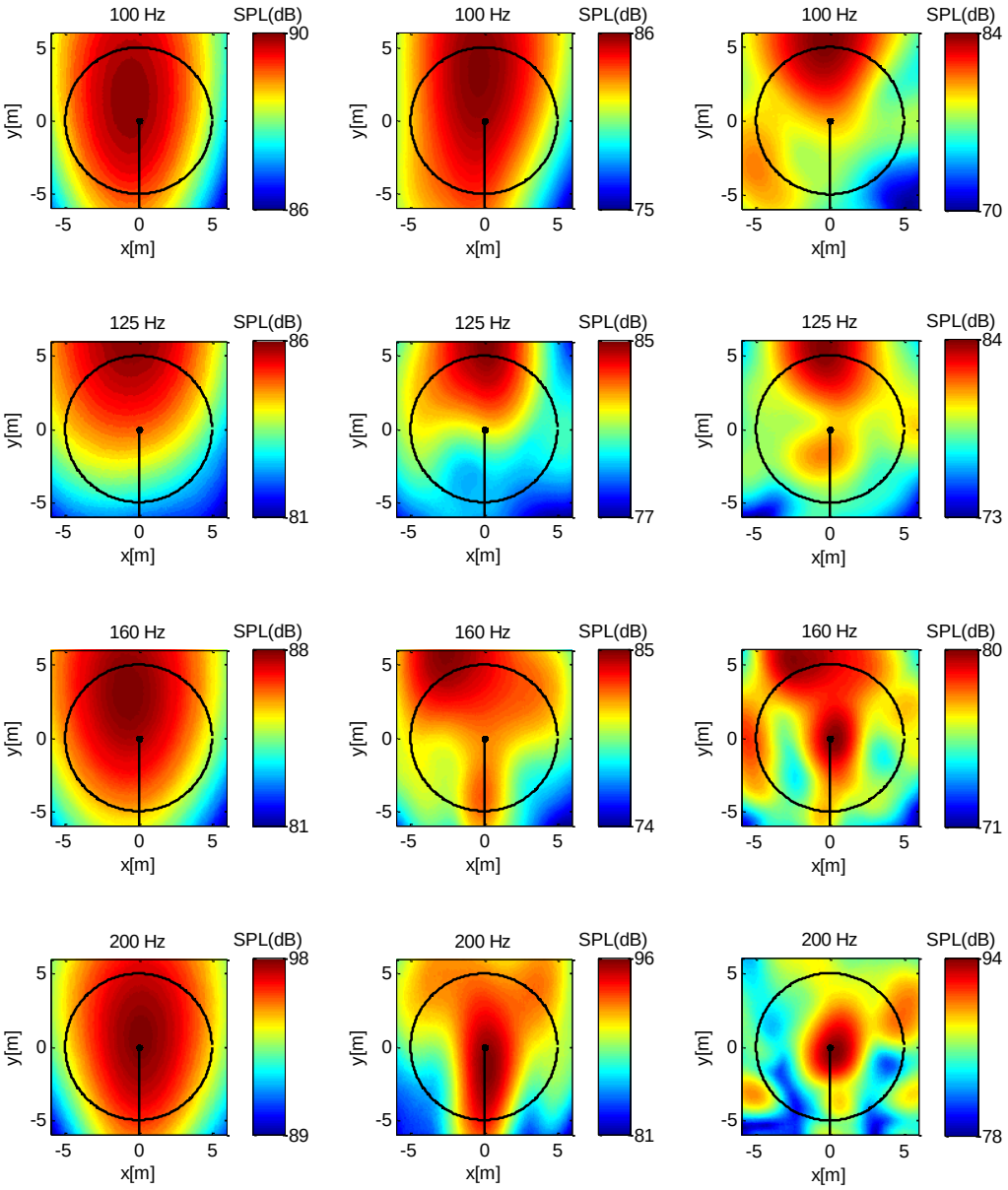

Figure 6.3: Numerical acoustic maps for the star array: 8 m × 8 m horizontal array at ground level (left column); 20 m × 20 m horizontal array at ground level (middle column); 20 m × 20 m vertical array parallel to the wind turbine rotor plane (right column). The incidence wind speed is 9 m s^{-1}. The wind turbine rotates in the counter-clockwise direction.

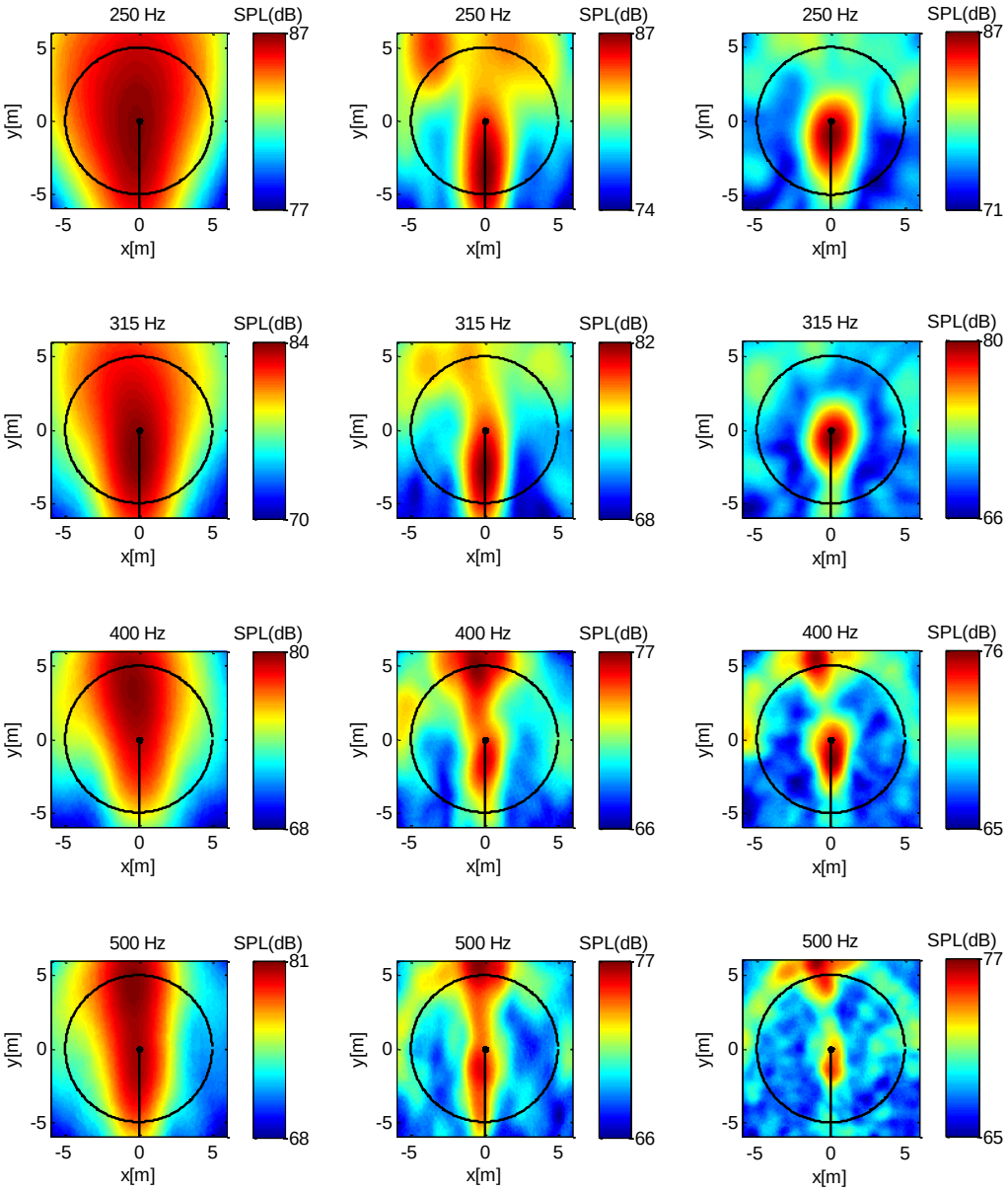

Figure 6.3 (continued).

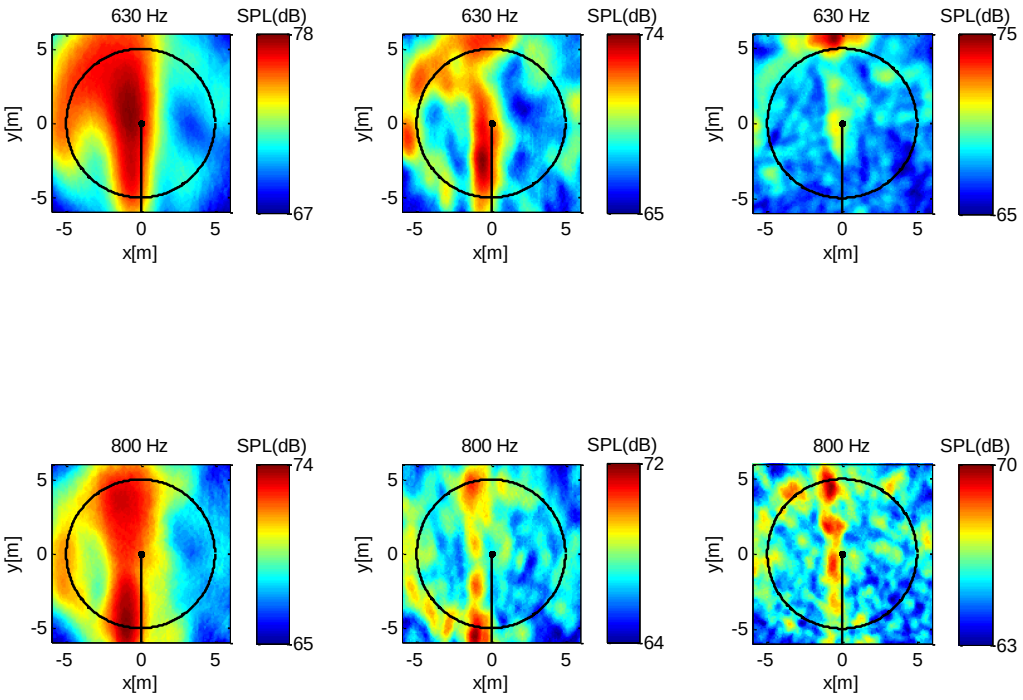

Figure 6.3: (continued).

For the two different microphone array geometries employed, the area of the identified sound source in the acoustic maps obtained for the vertical microphone array (the right columns of Figures 6.2 and 6.3) is smaller than that identified by the same size horizontal microphone array at ground level (the middle columns of Figures 6.2 and 6.3), implying a better resolution was achieved with the vertical microphone array. This is because the opening angle of the acoustic beamformer is decreased from 50° to 22° by using the vertical microphone array. According to the literature [128], a useful opening angle for an acoustic beamformer in practice is restricted to 30°. Furthermore, the smaller the opening angle, the better is the spatial resolution that is achieved in the

resulting acoustic maps. However, for actual acoustic beamforming measurements, erecting a large-sized microphone array is usually very difficult (technically and logistically). This is the reason that most of the large-sized microphone arrays are placed on the ground during measurements, with the disadvantage that this leads to a large opening angle for the acoustic beamformer. On the other hand, these limitations for the installation of microphone arrays are absent when the CAB methodology is used for the generation of the acoustic maps. In this case, any array geometry of any given size and with any orientation can be used for the acoustic beamforming. In consequence, the microphone array used in the CAB methodology can be placed at any location in order to achieve optimal performance for the noise source localization.

An examination of Figures 6.2 and 6.3 suggests that the identified noise source locations are different at different frequencies. This implies that the physical mechanisms responsible for the noise generation at these frequencies are different. For frequencies between 200 and 400 Hz, the identified noise source is located in the central area of the rotor plane. The noise at this location might be due to the wind turbine nacelle. As the frequency increases, the location of the identified noise source shifts downwards from the nacelle towards the outer portion of the rotor plane. The source of this noise (which is generated in the frequency range between 400 and 630 Hz) probably arises from the blade tower interaction. This inboard noise caused by the turbine nacelle and blade tower interaction has also been observed and reported in the literature [63], [96].

Figure 6.4 illustrates the maximum SPL on the acoustic map at the center frequency of each one-third octave band at a reference wind speed of 9 m s^{-1}. The Archimedean spiral and star arrays yielded very similar SPL shapes in the frequency range between 100 and 800 Hz. The highest sound pressure level occurs at about 200 Hz. The maximum SPL plots for reference wind speeds of 10 m s^{-1} and 11 m s^{-1} are presented in Appendix IV.

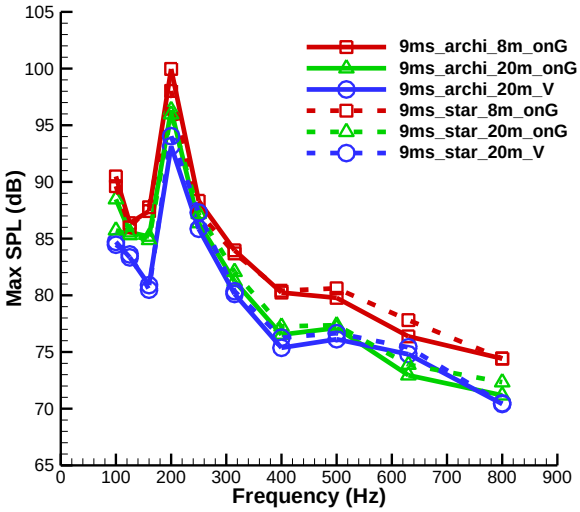

Figure 6.4: Max SPL vs. frequency for an incident wind speed of 9 m s^{-1}.

Chapter 7

Conclusions and Future Work

This thesis has proposed the CAB methodology for identification of noise sources generated by a small wind turbine. This predictive method was validated thoroughly on the component level (the three components of the CAB method have been validated with experimental data individually) and on the whole system level (the entire CAB method has been validated using the NACA 0012 airfoil trailing edge noise case).

The CFD component has been validated using data obtained for the Fortis Montana small HAWT and for the WINPhase 10 small commercial HAWT cases. Good agreement of the wind turbine power output was achieved between the experimental results (wind tunnel data and field measurement data) and the numerical results obtained from a DDES solver with S-A turbulence closure.

The acoustic propagation component has been validated using some measurements obtained for the tandem cylinders and the WINPhase 10 small commercial HAWT cases. The predicted SPL agreed well with the wind tunnel experimental data for the tandem cylinders case. Good agreement was also obtained between the predicted A-weighted SPL and field measurements at a reference point for the WINPhase 10 small commercial wind turbine case. It is found that, for this small HAWT, that the blade self-noise falls in the frequency range between approximately 250 and 1000 Hz and that the quadrupole sources included in the permeable formulation of the FW-H equation contribute to the

broadband noise at frequencies above approximately 1000 Hz. It is also found that the presence of the tower enhances the SPLA obtained at the reference point for frequencies above approximately 300 Hz.

The acoustic beamforming component has been validated using the data obtained for a point source at a single frequency. Both the plane wave incidence and spherical wave incidence acoustic beamformers yielded good agreement of acoustic maps with the experimental and theoretical results. The numerical simulation showed that the inclusion of the diagonal removal led to a decreased MSL in the acoustic maps.

The good agreement between the experimental data and the simulation results implies that the first objective listed in Section 1.4 (component level validation of the CAB methodology) has been achieved.

The CAB methodology on a whole system level has been validated using the NACA 0012 airfoil trailing edge noise case. The predicted acoustic maps were in excellent agreement with the corresponding acoustic maps obtained from wind-tunnel experiments. It is found that the spatial resolution of the CAB method on the acoustic maps increases with increasing frequency. It is also found that the Archimedean spiral array has a better spatial resolution than the star array at all frequencies of interest. Furthermore, an Archimedean spiral array exhibits better SNR at frequencies below 1000 Hz, but poorer SNR at frequencies above 1000 Hz when compared to the performance of a star microphone array.

The good agreement with the experimental data for the NACA 0012 airfoil case implies that the second objective listed in Section 1.4 (whole system level validation of the CAB methodology) has been achieved and provides the confidence to apply the CAB methodology on a small commercial HAWT (WINPhase 10 wind turbine). Despite the coarse grid and large time step used in the CFD simulations, the simulated aerodynamic results (wind turbine power output) and aeroacoustic results (A-weighted SPL spectra) were in good agreement with some field measurements for this wind turbine. The simulated acoustic maps revealed that the blade tower interaction and the wind turbine nacelle were two possible noise generation mechanisms in the range of frequencies between 200 and 630 Hz for this small wind turbine, which implies that the third objective listed in Section 1.4 (WINPhase 10 small wind turbine noise source investigation using CAB method) has been achieved.

The agreement between the numerical results obtained using the CAB methodology and the corresponding experimental data for both the NACA 0012 airfoil and the WINPhase 10 wind turbine suggests that the methodology proposed herein can be used to obtain deeper insights for the noise generation issue for other type of wind turbines and turbomachinery. This is especially true for applications where it would be difficult and expensive to conduct a comprehensive set of acoustic beamforming measurements. The CAB methodology can also be applied in cases that require large-sized microphone arrays and/or large numbers of microphones. In particular, it is anticipated that the CAB methodology will be less expensive to apply in these cases owing to the increasing

availability of cheap high-performance computing. In addition, the CAB methodology can also be applied as a virtual proving ground for optimization of microphone array geometries and acoustic beamforming algorithms for noise source identification that can take the user through the complete development cycle from design to evaluation. Finally, the use of the CAB methodology provides not only the acoustic maps for the noise source identification, but also the associated flow field which embodies the sound source information. This additional flow field information, which cannot be provided by the traditional acoustic beamforming experiments, can help researchers to gain deeper physical insights into the causes of the noise generated by turbomachinery (e.g., wind turbines, airfoils, etc.).

Future research efforts will focus on improving the simulation resolution and acoustic map quality for WINPhase 10 small wind turbine case. Currently, the noise source locations on the acoustic maps at frequencies below 200 Hz for this small wind turbine are difficult to identify because the sources appear to cover a relatively large area in the acoustic maps. It is anticipated that the use of more advanced acoustic beamforming techniques can potentially be used to improve the spatial resolution and, hence, to better localize the noise source in the acoustic maps for frequencies less than 200 Hz. Two examples of super-resolution techniques for acoustic beamforming are the non-negative least squares and the deconvolution approaches for noise source identification. It has been reported that these super-resolution techniques can improve the spatial resolution of the acoustic maps by a factor of typically between three and ten [82].

To better localize the noise sources in the acoustic maps for frequencies above 800 Hz for this small wind turbine, a finer mesh and a smaller time step will need to be used in the CFD simulations. If this is done, it is anticipated that the high-frequency noise source information (for frequencies greater than about 800 Hz) can be encapsulated in the flow field calculations. This information can subsequently be passed onto the aeroacoustic calculations which can then be used in the generation of acoustic maps that will provide a better localization of noise sources from the wind turbine that are associated with frequencies greater than about 800 Hz.

References

[1] *IEC 61400-11 Ed 2.1 2006-11 Wind Turbnie Generator Systems-Part 11 Acoustic Noise Measurement Techniques*, 2006.

[2] World Wind Energy Association, "2015 Summary Small Wind World Report," 2015.

[3] *AWEA Standard 9.1 - 2009 AWEA Small Wind Turbine Performance and Safety, Standard Acoustic Sound Testing*, 2009.

[4] P. Gipe, *Small Wind Turbines* [Online] Available: http://www.wind-works.org/cms/index.php?id=64&tx_ttnews%5Btt_news%5D=152&cHash=355c12e5aab85ed7b1ba8c55bde7efa2

[5] Distributed Wind Energy Association, "2014 Distributed Wind Market Report," 2014.

[6] S. Rolland and B. Auzane, "The Potential of Small and Medium Wind Energy in Developing Countries. A Guide for Energy Sector Decision-Makers," Alliance for Rural Electrification, 2012.

[7] S. Vanhaeverbeke, "Simulation of Aeroacoustic Emission for Small Wind Turbines," Project thesis, Department of Aerospace Engineering, University of Technology Delft, Delft, Netherlands, 2007.

[8] Museum of Science Wind Turbine Lab, "Boston Museum of Science Wind Turbine Lab: Two-Year Report on Rooftop Wind Turbines," 2012.

[9] Online picture source, Available: https://en.wikipedia.org/wiki/Strata_SE1

[10] Online picture source, Available: http://www.inapub.co.uk/pubs/gallery/21834.aspx

[11] T. Cho, C. Kim, and D. Lee, "Acoustic Measurement for 12% Scaled Model of NREL Phase VI Wind Turbine by using Beamforming,"*Current Applied Physics*,vol. 10, no. 2, pp. 320-325,2010.

[12] A. Bale and D. a. Johnson, “The Application of a MEMS Microphone Phased Array to Aeroacoustics of Small Wind Turbines,” *Wind Engineering*, vol. 37, no. 6, pp. 637-658, 2013.

[13] A. E. Bale, “The Application of MEMS Microphone Arrays to Aeroacoustic Measurements,” M.S. thesis, Department of Mechanical and Mechatronics Engineering, University of Waterloo, Waterloo, Ontario, Canada, 2011.

[14] C. S. Li, “Computational Acoustic Beamforming of Noise Source on Wind Turbine Airfoil,” M.S. thesis, Department of Mechanical and Mechatronics Engineering, University of Waterloo, Waterloo, Ontario, Canada, 2014.

[15] W. Devenport, R. A. Burdisso, H. Camargo et al., “Aeroacoustic Testing of Wind

Turbine Airfoils," NREL Technical Report, NREL/SR-500-43471,2010.

[16] F. Hutcheson and T. Brooks, "Effects of Angle of Attack and Velocity on Trailing Edge Noise Determined Using Microphone Array Measurements," *International Journal of Aeroacoustics*, vol. 5, no. 1, pp. 39-66, 2005.

[17] T. Brooks and W. Humphreys, "Effect of Directional Array Size on the Measurement of Airframe Noise Components," in *5th AIAA/CEAS Aeroacoustics Conf.*, Bellevue, Washington,May, 1999.

[18] E. Sarradj, C. Schulze, and A. Zeribig, "Aspects of Source Separation in Beamforming," in *1st Berlin Beamforming Conf.*, Berlin, Germany, Feb. 2006.

[19] J. G. Leishman, "*Principles of Helicopter Aerodynamics*," Cambridge: Cambridge University Press, 2006.

[20] J. L. Tangler, "The Nebulous Art of Using Wind Tunnel Aerofoil Data for Predicting Rotor Performance," *Wind Energy*, vol. 5, no. 2-3, pp. 245-257, 2002.

[21] R. Mikkelsen, "Actuator Disc Methods Applied to Wind Turbines," Ph.D dissertation, Department of Mechanical Engineering, Technical University of Denmark, Lyngby, Denmark, 2003.

[22] C. Alinot and C. Masson, "Aerodynamic Simulations of Wind Turbines Operating in Atmospheric Boundary Layer with Various Thermal Stratifications," in *ASME 2002 Wind Energy Symp.*, Reno, Nevada, Jan. 2002, pp. 206-215.

[23] C. Masson, "Viscous Differential/Actuator Disk Method and Its Applications," in *15th IEA Symp. on the Aerodynamics of Wind Turbines*, Athens, Nov. 2001, pp. 65-80.

[24] A. Elkasmi and C. Masson, "An Extended k–ε Model for Turbulent Flow through Horizontal-Axis Wind Turbines," *Journal of Wind Engineering and Industrial Aerodynamics*, vol. 96, no. 1, pp. 103-122, 2008.

[25] J. N. Sørensen and W. Z. Shen, "Numerical Modeling of Wind Turbine Wakes," *Journal of Fluids Engineering*, vol. 124, pp. 393-399, 2002.

[26] N. Troldborg, J. N. Sorensen, and R. Mikkelsen, "Numerical Simulations of Wake Characteristics of A Wind Turbine in Uniform Inflow," *Wind Energy*, vol. 13, no. 1, pp. 86-99, 2010.

[27] A. Gonzalez and X. Munduate, "Three-Dimensional and Rotational Aerodynamics on the NREL Phase VI Wind Turbine Blade," *Journal of Solar Energy Engineering*, vol. 130, no. 3, pp. 031008-031008-7, 2008.

[28] S. Schmitz and J.-J. Chattot, "Characterization of Three-Dimensional Effects for the Rotating and Parked NREL Phase VI Wind Turbine," *Journal of Solar Energy Engineering*, vol. 128, no. 4, pp. 445-454, 2006.

[29] S. Ivanell, J. N. Sørensen, R. Mikkelsen, and D. Henningson, "Numerical Analysis of the Tip and Root Vortex Position in the Wake of a Wind Turbine," *Journal of Physics: Conference Series*, vol. 75, 2007.

[30] K. S. and H. C., “Features of the 3D Flow around Wind Turbine Blades based on Numerical Solutions,” in *2001 European wind energy conference and exhibition*, Copenhagen, Denmark, Jul. 2001.

[31] S. Benjanirat, L. N. Sankar, and G. Xu, “Evaluation of Turbulence Models for the Prediction of Wind Turbine Aerodynamics,” in *41st Aerospace Sciences Meeting and Exhibit,* Reno, Nevada, Jan. 2003.

[32] Lakshmi N. Sankar, “Computational Studies of Horizontal Axis Wind Turbines,” Quarterly Progress Report for National Renewable Energy Laboratory, 2001.

[33] G. Xu and L. N. Sankar, “Effects of Transition, Turbulence and Yaw on the Performance of Horizontal Axis Wind Turbines,” in *2000 ASME Wind energy Symp.,* Reno, Nevada, Jan. 2000.

[34] S. Benjanirat and L. N. Sankar, “Recent Improvements to a Combined Navier-Stokes Full Potential Methodology for Modeling Horizontal Axis Wind Turbines,” in *42nd AIAA Aerospace Sciences Meeting and Exhibit, Reno, Nevada*, 2004, pp. 378-385.

[35] C. Tongchitpakdee, S. Benjanirat, and L. N. Sankar, “Numerical Simulation of the Aerodynamics of Horizontal Axis Wind Turbines under Yawed Flow Conditions,” *Journal of Solar Energy Engineering*, vol. 127, no. 4, pp. 464-474, 2005.

[36] N. N. Sørensen, “3D Background Aerodynamics using CFD,” Risø National Laboratory Technical Report, Risø-R-1376(EN), 2002.

[37] N. N. Sørensen, J. Johansen, and S. Conway, “CFD Computations of Wind Turbine Blade Loads During Standstill Operation TASK 3 .1 Report,” Risø National Laboratory Technical Report Risø-R-1465(EN), 2004.

[38] N. N. Sørensen, J. Johansen, S. Conway et al., “Tip Shape Study KNOW-BLADE Task 3.2 report,” Risø National Laboratory Technical Report, Risø-R-1495(rev)(EN), 2005.

[39] N. N. Sørensen, J. a. Michelsen, and S. Schreck, “Navier-Stokes Predictions of the NREL Phase VI Rotor in the NASA Ames 80 ft by 120 ft Wind Tunnel,” *Wind Energy*, vol. 5, no. 2-3, pp. 151-169, 2002.

[40] E. P. N. Duque, M. D. Burklund, and W. Johnson, “Navier-Stokes and Comprehensive Analysis Performance Predictions of the NREL Phase VI Experiment,” *ASME 2003 Wind Energy Symposium*,Reno, Nevada, Jan. 2003, pp. 43-61.

[41] A. Le Pape and J. Lecanu, “3-D Navier-Stokes Computations of a Stall-Regulated Wind Turbine,” *Wind Energy*, vol. 7, no. 4, pp. 309-324, 2004.

[42] A. Le Pape and V. Gleize, “Improved Navier-Stokes Computations of a Stall-regulated Wind Turbine using Low Mach number Preconditioning,” in *44th AIAA Aerospace Sciences Meeting and Exhibit,*Reno, Nevada, Jan. 2006.

[43] N. Sezer-uzol and L. N. Long, “3-D Time-Accurate CFD Simulations of Wind

Turbine Rotor Flow Fields," *AIAA Paper*, vol. 394, 2006.

[44] S. Gómez-Iradi and G. N. Barakos, "Computational Fluid Dynamics Investigation of Some Wind Turbine Rotor Design Parameters," *Proceedings of the Institution of Mechanical Engineers, Part A, Journal of Power and Energy*, vol. 222, no. 5, pp. 455-470, 2008.

[45] C. E. Carcangiu, "CFD-RANS Study of Horizontal Axis Wind Turbines," Ph.D Thesis, Università degli Studi di Cagliari, Italy, 2008.

[46] J. Wang, R. Jia, and K. Wu, "Numerical Simulation on Effect of Pressure Distribution of Wind Turbine Blade with a Tip Vane," *Journal of Thermal Science*, vol. 16, no. 3, pp. 203-207, 2007.

[47] E. Ferrer and X. Munduate, "Wind Turbine Blade Tip Comparison using CFD," *Journal of Physics: Conference Series*, vol. 75, 2007.

[48] T. Wang and F. N. Coton, "Wall Effects on Wind Turbine Flows," *Wind Energy*, vol. 3, no. 3, pp. 135-148, 2000.

[49] I. Grant, M. Mo, P. Parking, J. Powell, H. Reineche, K. Shuang, and F. Coton, "Optical Evaluation of the Wake Characteristics of a Wind Turbine and a Prescribed Wake Model," in *5th International Symposium on Flow Visualization*, 1998, pp. 132.1-132.15.

[50] D. Simms, S. Schreck, M. Hand, and L. J. Fingersh, "NREL Unsteady Aerodynamics Experiment in the NASA-Ames Wind Tunnel: A Comparison of Predictions to Measurements," NREL Technical Report, NREL/TP-500-29494, 2001.

[51] H. Glauert, *The Elements of Aerofoil and Wing Theory*. 2nd ed., Cambridge University Press, 1947.

[52] E. Duque, C. P. van Dam, and S. C. Hughes, "Navier-Stokes Simulations of the NREL Combined Experiment Phase II Rotor," in *37th Aerospace Sciences Meeting and Exhibit*, Reno, Nevada, 1999, pp. 143-153.

[53] F. Zahle, N. N. Sørensen, J. Johansen, and R. National, "Wind Turbine Rotor-Tower Interaction Using an Incompressible Overset Grid Method," *Wind Energy*, vol. 12, no. 6, pp. 594-619, 2009.

[54] P. Fuglsang and H. aagaard Madsen, "Implementation and Verification of an Aeroacoustic Noise Prediction Model for Wind Turbines," Risø National Laboratory Technical Report, Risø-R-867 (EN), 1996.

[55] T. F. Brooks, D. S. Pope, and M. A. Marcolini, "Airfoil Self-Noise and Prediction," NASA Technical Report, NASA-RP-1218, 1989.

[56] R. Parchen, "Progress Report DRAW, A Prediction Scheme for Trailing-edge Noise based on Detailed Boundary-layer Characteristics," TNO Report HAG-RPT-980023, TNO Institute of Applied Physics, Delft, Netherlands, 1998.

[57] R. K. Amiet, "Acoustic Radiation from an Airfoil in a Turbulent Stream," *Journal of Sound and Vibration*, vol. 41, no. 4, pp. 407-420, 1975.

[58] M. V. Lowson, “Applications of Aero-acoustic Analysis to Wind Turbine Noise Control,” *Wind Engineering*, vol. 16, no. 3, pp. 126-140, 1992.

[59] W. J. Zhu, “Modelling of Noise from Wind Turbines,” M.S. thesis, Department of Mechanical Engineering, Technical University of Denmark, Lyngby, Denmark, 2004.

[60] Y. Tian, B. Cotté, and A. Chaigne, “Wind Turbine Noise Modelling based on Amiet’s Theory,” in *5th International Conference on Wind Turbine Noise,* Denver, Colorado, Aug. 2013.

[61] Y. Tian, B. Cotté, and A. Chaigne, “Wind Turbine Noise Modeling : Prediction of Amplitude Modulation and Influence of Atmospheric Conditions,” in *Forum Acusticum*, Krakow, Poland, Sep. 2014.

[62] P. De Ruído, “Wind Turbine Noise Prediction,” M.S. thesis, University of Lisbon, Lisboa, Portugal, 2008.

[63] S. Oerlemans and J. G. Schepers, “Prediction of Wind Turbine Noise and Validation against Experiment,” NLR Technical Report, NLR-TP-2009-402, 2009.

[64] G. Leloudas, W. J. Zhu, J. N. Sørensen, W. Z. Shen, and S. Hjort, “Prediction and Reduction of Noise from a 2.3 MW Wind Turbine,” *Journal of Physics: Conference Series,* vol.75, 2007.

[65] K. Boorsma and J. G. Schepers, “Enhanced Wind Turbine Noise Prediction Tool SILANT,” in *4th International Meeting on Wind Turbine Noise*, Rome, Apr. 2011.

[66] P. Moriarty and P. Migliore, “Semi-empirical Aeroacoustic Noise Prediction Code for Wind Turbines,” NREL Technical Report, NREL/TP-500-34478, 2003.

[67] H. A. Madsen, J. Johansen, N. N. Sørensen, G. C. Larsen, and M. H. Hansen, “Simulation of Low frequency Noise from a Downwind Wind Turbine Rotor,” in*45th AIAA Aerospace Sciences Meeting and Exhibit*, Reno, Nevada, Jan. 2007.

[68] H. A. Madsen, “Low Frequency Noise from MW Wind Turbines -- Mechanisms of Generation and its Modeling,” Risø National Laboratory Technical Report,Risø-R-1637(EN), 2008.

[69] H. Klug, T. Osten, M. V. Lowson, J. Jakobsen et al., “Aerodynamic Noise from Wind Turbines and Rotor Blade Modification. JOULE 2 Final Report,” DEWI-V-95-0006, 1995.

[70] F. Farassat, “Derivation of Formulations 1 and 1A of Farassat,” Nasa Technical Report, NASA/TM-2007-214853, 2007.

[71] T. Fukano, Y. Kodama, and Y. Senoo, “Noise Generated by Low Pressure Axial Flow Fans, I: Modeling of the Turbulent Noise,” *Journal of Sound and Vibration*, vol. 50, no. 1, pp. 63-74, 1977.

[72] T. Fukano, Y. Kodama, and Y. Takamatsu, “Noise Generated by Low Pressure Axial Flow Fans, II: Effects of Number of Blades, Chord Length and Camber of Blade,” *Journal of Sound and Vibration*, vol. 50, no. 1, pp. 75-88, 1977.

[73] T. Fukano, Y. Kodama, and Y. Takamatsu, “Noise Generated by Low Pressure Axial Flow Fans, III: Effects of Rotational Frequency, Blade Thickness anda Outer Blade Profile,” *Journal of Sound and Vibration*, vol. 56, no. 2, pp. 261-277, Jan. 1978.

[74] A. E. Filios, N. S. Tachos, A. P. Fragias et al., “Broadband Noise Radiation Analysis for an HAWT Rotor,” *Renewable Energy*, vol. 32, no. 9, pp. 1497-1510, 2007.

[75] D. Moroianu and L. Fuchs, “Numerical Simulation of Wind Turbine Noise Generation and Propagation,” in *6th International ERCOFTAC Workshop on Direct and Large-Eddy Simulation,* Poitiers, France, 2005.

[76] A. Tadamasa and M. Zangeneh, “Numerical Prediction of Wind Turbine Noise,” *Renewable Energy*, vol. 36, no. 7, pp. 1902-1912, 2011.

[77] C. Arakawa, O. Fleig, M. Iida, and M. Shimooka, “Numerical Approach for Noise Reduction of Wind Turbine Blade Tip with Earth Simulator,” *Journal of the Earth Simulator*, vol. 2, pp. 11-33, 2005.

[78] O. Fleig, M. Iida, and C. Arakawa, “Wind Turbine Blade Tip Flow and Noise Prediction by Large-eddy Simulation,” *Journal of Solar Energy Engineering*, vol. 126, no. 4, 2004.

[79] W. J. Zhu, “Aero-Acoustic Computations of Wind Turbines,” Ph.D thesis, Department of Mechanical Engineering, Technical University of Denmark, Lyngby, Denmark, 2007.

[80] J. C. Hardin and D. S. Pope, “An Acoustic/Viscous Splitting Technique for Computational Aeroacoustics,” *Theoretical and Computational Fluid Dynamics*, vol. 6, pp. 323-340, 1994.

[81] W. Z. Shen and J. N. Sorensen, “Comment on the Aeroacoustic Formulation of Hardin and Pope,” *AIAA Journal*, vol. 37, pp. 141-143, 1999.

[82] K. B. Ginn and K. Haddad, “Noise Source Identification Techniques: Simple to Advanced Applications,” in *Acoustics 2012*, Nantes, France, Apr. 2012.

[83] S. Gade and J. Hald, “Noise Source Identification with Increased Spatial Resolution Used in Automotive Industry,”*J. Acoust. Soc. Am.,* vol. 131, 2012.

[84] S. Buck, J. Roadman, P. Moriarty, and S. Palo, “Acoustic Array Development for Wind Turbine Noise Characterization,” NREL Technical Report, NREL/TP-5000-60457, 2013.

[85] L. Koop and K. Ehrenfried, “Microphone Array Processing for Wind Tunnel Measurements with Strong Background Noise,” in *14th AIAA/CEAS Aeroacoustics Conference (29th AIAA Aeroacoustics Conference)*, Vancouver, British Columbia, May 2008.

[86] X. F. Zhang, Y. G. Xiao, and H. L. Deng, “Noise Source Localization Investigation in High Speed Train Based on Microphone Array,” *Applied Mechanics and Materials*, vol. 103, pp. 285-291, 2012.

[87] P. T. Soderman and C. S. Allen, “Microphone Measurements In and Out of

Airstream," in *Aeroacoustic Measurements*, T. J. Mueller, Ed. Springer Berlin Heidelberg,2002, pp. 1-61.

[88] R. C. Ramachandran and G. Raman, "Evaluation of Various Beamforming Algorithms for Wind Turbine Noise Measurement," in *49th AIAA Aerospace Sciences Meeting including the New Horizons Forum and Aerospace Exposition*, Orlando, Florida, Jan. 2011.

[89] R. C. Ramachandran, H. Patel, G. Raman, and R. P. Dougherty, "Localization of Wind Turbine Noise Sources Using a Compact Microphone Array with Advanced Beamforming Algorithms," in *4th Berlin Beamforming Conference*, Berlin, Germany, Feb. 2012.

[90] G. Raman and R. C. Ramachandran, "Remote Noise Source Localization for Complex Machines such as Wind Turbines," in *21st International Congress on Sound and Vibration*, Beijing, China, Jul. 2014.

[91] S. Oerlemans and B. Méndez López, "Acoustic Array Measurements on a Full Scale Wind Turbine," in *11th AIAA/CEAS Aeroacoustics Conference,* Monterey, California, May 2005.

[92] S. Oerlemans, M. Fisher, T. Maeder, and K. Kögler, "Reduction of Wind Turbine Noise Using Optimized Airfoils and Trailing-Edge Serrations,"*AIAA Journal,* vol. 47, no. 6, 2009.

[93] S. Oerlemans, P. Sijtsma, and B. Mendez-Lopez, "Location and Quantification of Noise Sources on a Wind Turbine," NLR Technical Report, NLR-TP-2007-798, 2007.

[94] S. Oerlemans, "Prediction of Wind Turbine Noise and Comparison with Experiment," NLR Technical Report, NLR-TP-2007-654, 2007.

[95] S. Oerlemans, "An Explanation for Enhanced Amplitude Modulation of Wind Turbine Noise," NLR Technical Report, NLR-CR-2011-071, 2011.

[96] E. J. Simley, "Development of an Acoustic Array for Wind Turbine Aeroacoustic Noise Analysis," M.S. thesis, Department of Electrical, Computer, and Energy Engineering, University of Colorado, Doulder, Colorado, 2010.

[97] E. Simley, P. Moriarty, and S. Palo, "Aeroacoustic Noise Measurements of a Wind Turbine with BSDS Blades using an Acoustic Array," in *48th AIAA Aerospace Sciences Meeting including the New Horizons Forum and Aerospace Exposition,* Orlando, Florida, Jan. 2010.

[98] S. M. Orlando, "Laser Doppler Anemometry and Acoustic Measurements of an S822 Airfoil at Low Reynolds Numbers," M.S.thesis, Department of Mechanical and Mechatronics Engineering, University of Waterloo, Waterloo, Canada, 2011.

[99] M. Wang, J. B. Freund, and S. K. Lele, "Computational Prediction of Flow-Generated Sound," *Annual Review of Fluid Mechanics*, vol. 38, no. 1, pp. 483-512, 2006.

[100] T. B. Gatski and J. P. Bonnet, "*Compressibility, Turbulence and High Speed Flow*,"

11st ed. Amsterdam: Elsevier Science, 2009.

[101] D. C. Wilcox, "*Turbulence Modeling for CFD*," 3rd ed. DCW Industries, 2006.

[102] C. Hirsch, "*Numerical Computation of Internal and External Flows: The Fundamentals of computational Fluid Dynamics,"*2nd ed. Butterworth-Heinemann, 2007.

[103] F. M. White, "*Viscous Fluid Flow*," New York: McGraw Hill, 1974.

[104] W. Rodi, "Experience with Two-Layer Models Combining the k-ε Model with a One-Equation Model Near the Wall," in*29th Aerospace Sciences Meeting,* Reno, Neveda, Jan. 1991.

[105] B. E. Launder and D. B. Spalding, "The Numerical Computation of Turbulent Flows," *Computer Methods in Applied Mechanics and Engineering*, vol. 3, no. 2, pp. 269-289, 1974.

[106] B. E. Launder and D. B. Spalding, "*Lectures in Mathematical Models of Turbulence,"* London, England: Academic Press, 1972.

[107] M. Wolfshtein, "The Velocity and Temperature Distribution in One-Dimensional Flow with Turbulence Augmentation and Pressure Gradient," *International Journal of Heat and Mass Transfer*, vol. 12, no. 3, pp. 301-318, 1969.

[108] V. Yakhot, S. Orszag, S. Thangam, T. Gatski, and C. G. Speziale, "Development of Turbulence Models for Shear Flows by a Double Expansion Technique," *Physics of Fluids A*, vol. 4, no. 7, pp. 1510-1520, 1992.

[109] F. R. Menter, "Two-Equation Eddy-Viscosity Turbulence Models for Engineering Application," *AIAA Journal*, vol. 32, no. 8, pp. 1598-1605, 1994.

[110] U. Frisch, "*Turbulence: The Legacy of A. N. Kolmogorov,"* Cambridge University Press, 1996.

[111] K. Khusnutdinova, "Kolmogorov's 5/3 law," [Online], Available: http://homepages.lboro.ac.uk/~makk/mathrev_kolmogorov.pdf

[112] S. G. Chumakov, "Subgrid Models for Large Eddy Simulation: Scalar Flux, Scalar Dissipation and Energy Dissipation," Ph.D thesis, Department of Mechanical Engineering, University of Wisconsin-Madison, Madison, Wisconsin, 2005.

[113] E. Garnier, N. Adams, and P. Sagaut, *"Large Eddy Simulation for Compressible Flows,"* Springer Netherlands, 2009.

[114] J. Smagorinsky, "General Circulation Experiments with the Primitive Equations: Part I, The Basic Experiment," *Monthly Weather Review*, vol. 91, no. 3, pp. 99-164, 1963.

[115] E. R. Van Driest, "On Turbulent Flow Near a Wall," *Journal of the Aeronautical Sciences*, vol. 23, no. 11, pp. 1007-1011, 1956.

[116] E. Balaras, C. Benocci, and U. Piomelli, "Two-Layer Approximate Boundary Conditions for Large-Eddy Simulations," *AIAA Journal*, vol. 34, no. 6, pp. 1111-

1119, 1996.

[117] P. R. Spalart, W. H. Jou, M. Strelets, and S. R. Allmaras, “Comments on the Feasibility of LES for Wings, and on a Hybrid RANS/LES Approach,” in *Proceedings of the First AFOSR International Conference on DNS/LES,* Ruston, Louisiana, Aug. 1997.

[118] P. Spalart and S. Allmaras, “A One-Equation Turbulence Model for Aerodynamic Flows,” in *30th Aerospace Sciences Meeting and Exhibit,* Reno, Neveda, Jan. 1992.

[119] P. R. Spalart, “Detached-Eddy Simulation,” *Annual Review of Fluid Mechanics*, vol. 41, pp. 181-202, 2009.

[120] F. R. Menter and M. Kuntz, “Adaptation of Eddy-Viscosity Turbulence Models to Unsteady Separated Flow Behind Vehicles,” in *The Aerodynamics of Heavy Vehicles: Trucks, Buses and Trains*, R. McCallen, F. Browand, and J. Ross, Eds. Springer, Berlin Heidelberg New York, 2004, pp. 339-359.

[121] P. R. Spalart, S. Deck, M. L. Shui et al., “A New Version of Detached-Eddy Simulation, Resistant to Ambiguous Grid Densities,” *Theoretical and Computational Fluid Dynamics*, vol. 20, pp. 181-195, 2006.

[122] T. Cebeci and P. Bradshaw, “Momentum Transfer in Boundary Layers,” McGraw-Hill Inc., 1977, pp. 176-180.

[123] T. Knopp, “Model-Consistent Universal Wall-Functions for RANS Turbulence Modelling,” in *BAIL 2006 International Conference on Boudary and Interior Layers*, Goettingen, Germany, Jul. 2006.

[124] J. E. F. Williams and D. L. Hawkings, “Sound Generation by Turbulence and Surfaces in Arbitrary Motion.,” *Philosophical Transactions of the Royal Society of London Series A Mathematical and Physical Sciences*, vol. 264, no. 1151, pp. 321-342, 1969.

[125] C. J. Doolan, “Computational Bluff Body Aerodynamic Noise Prediction Using a Statistical Approach,” *Applied Acoustics*, vol. 71, no. 12, pp. 1194-1203, 2010.

[126] G. C. Waller, “Prediction of Flap-Edge Noise Using STAR-CD,” in *14th AIAA/CEAS Aeroacoustics Conference (29th AIAA Aeroacoustics Conference)*, Vancouver, British Columbia, Canada, May 2008.

[127] A. Greensted, “Delay Sum Beamforming,” [Online], Available: http://www.labbookpages.co.uk/audio/beamforming/delaySum.html

[128] J. J. Christensen and J. Hald, “Technical Review - Beamforming,” Brüel & Kjær Technical Review, 2004.

[129] S. Gade and J. Hald, “Noise Source Identification with Increased Spatial Resolution used in Automotive Industry,” *Journal of Acoustic Soceity of America*, vol. 131, 2012.

[130] M. Kern and H. Opfer, “Enhancement of the Dynamic Range in Acoustic Photos by Modified Time Domain Beamforming,” in *2nd Berlin Beamforming*

Conference,Berlin, Germany, Feb. 2008.

[131] R. P. Doughery, “Beamforming in Acoustic Testing,” in *Aeroacoustic Measurements*, T. J. Mueller, Ed. Berlin: Springer, 2002, pp. 83-86.

[132] W. C. Horne and K. D. James, “Concepts for Reducing the Self-noise of In-flow Acoustic Sensors and Arrays,” in *5th AIAA/CEAS Aeroacoustics Conference and Exhibit,* Bellevue, Washington, May 1999.

[133] S. Oerlemans and P. Sijtsma, “Acoustic Array Measurements of a 1:10.6 Scaled Airbus A340 Model,”in *10th AIAA/CEAS Aeroacoustics Conference,* Manchester, UK, May 2004.

[134] A. Xenaki, F. Jacobsen, E. Tiana-roig, and E. F. Grande, “Improving the Resolution of Beamforming Measurements on Wind Turbines,” in *Proceedings of 20th International Congress on Acoustics*, Sydney, Australia, Aug. 2010.

[135] S. Benjanirat, “Computational Studies of Horizontal Axis Wind Turbines in High Wind Speed Condition Using Advanced Turbulence Models,” Ph.D thesis, Department of Aerospace Engineering, Georgia Institute of Technology, Atlanta, Georgia, 2006.

[136] P. Ma, M. Li, J. Jilesen, F.-S. Lien, E. Yee, and H. Harrison, “A Comparison of Coarse-Resolution Numerical Simulation with Experimental Measurements of Wind Turbine Aerodynamic Performance,” *Procedia Engineering*, vol. 79, pp. 17-27, 2014.

[137] D. P. Lockard, M. R. Khorrami, M. M. Choudhari, F. V Hutcheson, T. F. Brooks, and D. J. Stead, “Tandem Cylinder Noise Predictions,” in *13th AIAA/CEAS Aeroacoustics Conference*, Rome, Italy, May 2007.

[138] C. J. Doolan, “Flow and Noise Simulation of the NASA Tandem Cylinder Experiment using OpenFOAM,” in *15th AIAA/CEAS Aeroacoustics Conference*, Miami, Florida, May 2009.

[139] T. Rossing (Ed.), "Springer Handbook of Acoustics," Berlin: Springer-Verlag, 2015.

[140] P. Migliore and S. Oerlemans, “Wind Tunnel Aeroacoustic Tests of Six Airfoils for Use on Small Wind Turbines,” in *10th AIAA/CEAS Aeroacoustics Conference*, Manchester, UK,May 2004.

[141] N. Gregory and C. L. O’Reilly, “Low-Speed Aerodynamic Characteristics of NACA 0012 Aerofoil Sections, including the Effects of Upper-Surface Roughness Simulation Hoar Frost,” NASA Technical Report, NASA R&M 3726, 1970.

[142] C. L. Ladson, “Effects of Independent Variation of Mach and Reynolds Numbers on the Low-Speed Aerodynamic Characteristics of the NACA 0012 Airfoil Section,” NASA Technical Report, NASA TM 4074, 1988.

[143] M. Wang, “Computation of Trailing-Edge Noise at Low Mach Number Using LES and Acoustic Analogy,” Center for Turbulence Research Annual Research Briefs 1998, 1998.

[144] C. Kato, A. Iida, Y. Takano, and M. Ikegawa, “Numerical Prediction of Aerodynamic Noise Radiated from Low Mach Number Turbulent Wake,” in *31st Aerospace Sciences Meeting,* Reno, Neveda, Jan. 1993.

[145] K. S. Patel, S. B. Patel, U. B. Patel, and A. P. Ahuja, “CFD Analysis of an Aerofoil,” *International Journal of Engineering Research*, vol. 3, no. 3, pp. 154-158, 2014.

[146] R. K. Amiet, “Noise due to Turbulent Flow past a Trailing Edge,” *Journal of Sound and Vibration*, vol. 47, pp. 387-393, 1976.

[147] T. Jongen, “Simulation and Modeling of Turbulent Incompressible Flows,” Ph.D thesis, EPF Lausanne, Lausanne, Switzerland, 1992.

[148] J. Dacles-Mariani, G. G. Zilliac, J. S. Chow, and P. Bradshaw, “Numerical/Experimental Study of a Wingtip Vortex in the Near Field,” *AIAA Journal*, vol. 33, no. 9, pp. 1561-1568, 1995.

[149] J. Dacles-Mariani, D. Kwak and G. G. Zilliac, "On Numerical Errors and Turbulence Modeling in Tip Vortex Flow Prediction," *International Journal for Numerical Methods in Fluids*, vol. 30, pp. 65-82, 1999.

Appendix I RANS Turbulence Models

I.1 $k-\varepsilon$ Two-layer Turbulence Model

The transport equations for the standard $k-\varepsilon$ model [105], [106] are given by

$$\frac{\partial}{\partial t}(\bar{\bar{\rho}}k)+\frac{\partial}{\partial x_j}(\bar{\bar{\rho}}k\hat{u}_j)=\frac{\partial}{\partial x_j}\left[\left(\mu+\frac{\hat{\mu}_t}{\sigma_k}\right)\frac{\partial k}{\partial x_j}\right]+G_k-\bar{\bar{\rho}}\varepsilon; \tag{I.1}$$

and

$$\frac{\partial}{\partial t}(\bar{\bar{\rho}}\varepsilon)+\frac{\partial}{\partial x_j}(\bar{\bar{\rho}}\varepsilon\hat{u}_j)=\frac{\partial}{\partial x_j}\left[\left(\mu+\frac{\hat{\mu}_t}{\sigma_\varepsilon}\right)\frac{\partial \varepsilon}{\partial x_j}\right]+C_{1\varepsilon}\frac{\varepsilon}{k}G_k-C_{2\varepsilon}\bar{\bar{\rho}}\frac{\varepsilon^2}{k}, \tag{I.2}$$

where the turbulence viscosity $\hat{\mu}_t$ is calculated from

$$\hat{\mu}_t=\bar{\bar{\rho}}C_\mu\frac{k^2}{\varepsilon}. \tag{I.3}$$

The generation of turbulence kinetic energy G_k due to the mean velocity gradients is calculated as

$$G_k=-\rho\overline{\overline{u_i'u_j'}}\frac{\partial\hat{u}_j}{\partial x_i}=\hat{\mu}_tS^2, \tag{I.4}$$

where S is the modulus of the mean rate of strain tensor and has the following expression:

$$S = \sqrt{2\hat{S}_{ij}\hat{S}_{ij}}, \tag{I.5}$$

where $\hat{S}_{ij}$ is the Favre-averaged rate of strain tensor and can be calculated by

$$\hat{S}_{ij} = \frac{1}{2}\left(\frac{\partial \hat{u}_i}{\partial x_j} + \frac{\partial \hat{u}_j}{\partial x_i}\right). \tag{I.6}$$

Within the near wall region, a blending function

$$\lambda_T = \frac{1}{2}\left[1 + \tanh\left(\frac{Re_y - Re_y^*}{A}\right)\right], \tag{I.7}$$

where Re_y(wall distance Reynolds number), is given by Jongen [147]. A value of $Re_y^* = 60$ was used which implies that the standard $k-\varepsilon$ turbulence model will be applied directly beyond $Re_y = 60$.

In Eq. (I.7), the width of λ_T is determined by the constant

$$A = \frac{\left|\Delta Re_y\right|}{\operatorname{arctanh}(0.98)}, \tag{I.8}$$

where $\Delta Re_y = 10$.

The turbulent viscosity from the $k-\varepsilon$ model was blended with the two-layer value as follows:

$$\hat{\mu}_t = \lambda_T \hat{\mu}_t|_{k-\varepsilon} + (1-\lambda_T)\mu\left(\frac{\hat{\mu}_t}{\mu}\right)_{near-wall}, \quad \text{(I.9)}$$

where the turbulent viscosity ratio from the near wall model can be calculated by

$$\frac{\hat{\mu}_t}{\mu} = Re_y C_\mu^{1/4}\kappa\left[1-\exp\left(-\frac{Re_y}{A_\mu}\right)\right], \quad \text{(I.10)}$$

where $A_\mu = 70$.

The turbulent dissipation rate is computed as

$$\varepsilon = \frac{k^{3/2}}{l_\varepsilon}. \quad \text{(I.11)}$$

The one-equation Wolfshtein model [107] was used to calculate the characteristic length scale

$$l_\varepsilon = C_l y\left[1-\exp\left(-\frac{Re_y}{A_\varepsilon}\right)\right], \quad \text{(I.12)}$$

where

$$A_\varepsilon = 2C_l, \qquad C_l = \kappa C_\mu^{-\frac{3}{4}}, \quad C_\mu = 0.09, \quad \kappa = 0.42. \tag{I.13}$$

The constants used to close the two layer $k-\varepsilon$ turbulence model are listed below:

$$C_{1\varepsilon} = 1.44, \qquad C_{2\varepsilon} = 1.92, \quad \sigma_k = 1.0, \qquad \sigma_\varepsilon = 1.3. \tag{I.14}$$

I.2 RNG $k-\varepsilon$ Turbulence Model

The transport equations of turbulent kinetic energy k and dissipation rate ε are:

$$\frac{\partial}{\partial t}(\bar{\bar{\rho}}k) + \frac{\partial}{\partial x_j}\left(\bar{\bar{\rho}}k\hat{u}_j\right) = \frac{\partial}{\partial x_j}\left[\alpha\hat{\mu}_{eff}\frac{\partial k}{\partial x_j}\right] + G_k - \bar{\bar{\rho}}\varepsilon; \tag{I.15}$$

and

$$\frac{\partial}{\partial t}(\bar{\bar{\rho}}\varepsilon) + \frac{\partial}{\partial x_j}\left(\bar{\bar{\rho}}\varepsilon\hat{u}_j\right) = \frac{\partial}{\partial x_j}\left[\alpha\hat{\mu}_{eff}\frac{\partial \varepsilon}{\partial x_j}\right] + C_{1\varepsilon RNG}\frac{\varepsilon}{k}G_k - C_{2\varepsilon RNG}\bar{\bar{\rho}}\frac{\varepsilon^2}{k} - R_\varepsilon, \tag{I.16}$$

where $\hat{\mu}_{eff}$ is the effective viscosity and α is the inverse effective Prandtl number which is computed using the following formula derived analytically by the RNG theory:

$$\left|\frac{\alpha - 1.3929}{0.3929}\right|^{0.6321}\left|\frac{\alpha + 2.3929}{3.3929}\right|^{0.3679} = \frac{\mu}{\hat{\mu}_{eff}}, \tag{I.17}$$

for high Reynolds number flow where $\frac{\mu}{\hat{\mu}_{eff}} \ll 1$, $\alpha \approx 1.393$.

The turbulent eddy viscosity in the RNG $k-\varepsilon$ turbulence model is related to k^2/ε via a differential equation

$$\frac{d\left(\frac{\rho^2 k}{\sqrt{\varepsilon\mu}}\right)}{d\hat{v}} = 1.72\frac{\hat{v}}{\sqrt{\hat{v}^3 - 1 + C_v}}, \tag{I.18}$$

where $\hat{v} = \frac{\hat{\mu}_{eff}}{\mu}$, $C_v \approx 100$.

For high Reynolds number flow, $\hat{\mu}_t = \frac{\bar{\bar{\rho}} C_{\mu RNG} k^2}{\varepsilon}$ with $C_{\mu RNG} = 0.0845$.

The main difference between the standard $k-\varepsilon$ turbulence model and the RNG $k-\varepsilon$ turbulence model is the additional term added to the dissipation rate transport equation given by

$$R_\varepsilon = \frac{C_{\mu RNG}\bar{\bar{\rho}}\eta^3(1-\frac{\eta}{\eta_0})}{1+\beta\eta^3}\frac{\varepsilon^2}{k}, \tag{I.19}$$

where η is the ratio of the turbulent to mean strain time scale given by

$$\eta = \frac{Sk}{\varepsilon}. \tag{I.20}$$

The closure constants for the RNG $k-\varepsilon$ turbulence model have the following values:

$$C_{1\varepsilon RNG} = 1.42, \quad C_{2\varepsilon RNG} = 1.68, \quad \beta = 0.012, \quad \eta_0 = 4.38. \tag{I.21}$$

I.3 $k-\omega$ SST Turbulence Model

Two transport equations,

$$\frac{\partial}{\partial t}(\bar{\bar{\rho}}k)+\frac{\partial}{\partial x_j}(\bar{\bar{\rho}}k\hat{u}_j)=\frac{\partial}{\partial x_j}\left[\left(\mu+\frac{\hat{\mu}_t}{\sigma_k}\right)\frac{\partial k}{\partial x_j}\right]+\tilde{G}_k-Y_k; \tag{I.22}$$

and

$$\frac{\partial}{\partial t}(\bar{\bar{\rho}}\omega)+\frac{\partial}{\partial x_j}(\bar{\bar{\rho}}\omega\hat{u}_j)=\frac{\partial}{\partial x_j}\left[\left(\mu+\frac{\hat{\mu}_t}{\sigma_\omega}\right)\frac{\partial \omega}{\partial x_j}\right]+G_\omega-Y_\omega+D_\omega, \tag{I.23}$$

are solved in the $k-\omega$ SST turbulence model [109], where k is the turbulence kinetic energy and ω is the dissipation per unit turbulence kinetic energy.

The generation of k and ω, $\tilde{G}_k$ and G_ω, the cross diffusion term D_ω, and σ_k and σ_ω are calculated by the following equations:

$$\tilde{G}_k=\min(G_k,10\rho\beta^*k\omega), \qquad G_\omega=\frac{\alpha}{\hat{\nu}_t}\tilde{G}_k, \tag{I.24}$$

$$D_\omega=2(1-F_1)\bar{\bar{\rho}}\sigma_{\omega,2}\frac{1}{\omega}\frac{\partial k}{\partial x_j}\frac{\partial \omega}{\partial x_j},$$

$$\sigma_k=\left[\left(F_1/\sigma_{k,1}\right)+\left(\frac{1-F_1}{\sigma_{k,2}}\right)\right]^{-1}, \qquad \sigma_\omega=[\left(F_1/\sigma_{\omega,1}\right)+((1-F_1)/\sigma_{\omega,2})]^{-1},$$

where

$$G_k = -\overline{\overline{\rho u_i' u_j'}}\frac{\partial \hat{u}_j}{\partial x_i}, \qquad \alpha = \frac{\alpha_\infty}{\alpha^*}\left(\frac{\alpha_0 + Re_t/R_\omega}{1 + Re_t/R_\omega}\right), \tag{I.25}$$

$$\alpha^* = \alpha_\infty^*\left(\frac{\alpha_0^* + Re_t/R_k}{1 + Re_t/R_k}\right),$$

$$\alpha_\infty = F_1\alpha_{\infty,1} + (1 - F_1)\alpha_{\infty,2}, \qquad F_1 = \tanh(\Phi_1^4),$$

$$\Phi_1 = \min\left[\max\left(\frac{k^{1/2}}{\beta^*\omega y}, \frac{500\mu}{\bar{\bar{\rho}} y^2 \omega}\right), \frac{4\bar{\bar{\rho}} k}{\sigma_{\omega,2} D_\omega^+ y^2}\right],$$

$$\alpha_{\infty,1} = \beta_{i,1}/\beta_\infty^* - \kappa^2\left(\sigma_{\omega,1}\right)^{-1}(\beta_\infty^*)^{-1/2},$$

$$\alpha_{\infty,2} = \beta_{i,2}/\beta_\infty^* - \kappa^2\left(\sigma_{\omega,2}\right)^{-1}(\beta_\infty^*)^{-1/2},$$

$$Re_t = \frac{\bar{\bar{\rho}} k}{\mu\omega}, \quad D_\omega^+ = \max\left(2\bar{\bar{\rho}}\frac{1}{\sigma_{\omega,2}}\frac{1}{\omega}\frac{\partial k}{\partial x_j}\frac{\partial \omega}{\partial x_j}, 10^{-10}\right).$$

In Eq. (I.25), $-\overline{\overline{\rho u_i' u_j'}}$ is the Reynolds stress tensor which is modeled using the Boussinesq assumption. The dissipation of k and ω, Y_k and Y_ω in Eq. (I.22) and Eq. (I.23) is determined using the following equations:

$$Y_k = \bar{\bar{\rho}}\beta_i^* k\omega, \tag{I.26}$$

$$Y_\omega = \bar{\bar{\rho}}\beta_i\omega^2, \qquad \beta_i^* = \beta_\infty^*\left[\frac{4/15 + \left(Re_t/R_\beta\right)^4}{1 + \left(Re_t/R_\beta\right)^4}\right],$$

where

$$\beta_i = F_1\beta_{i,1} + (1 - F_1)\beta_{i,2}.$$

Finally, the turbulent viscosity is computed using the following equation:

$$\mu_t = \frac{\bar{\bar{\rho}}k/\omega}{\max\left(\frac{1}{\alpha^*}, \frac{SF_2}{a_1\omega}\right)}, \tag{I.27}$$

where

$$F_2 = \tanh(\Phi_2^2), \qquad \Phi_2 = \max\left(\frac{2k^{1/2}}{\beta^*\omega y}, \frac{500\mu}{\bar{\bar{\rho}}y^2\omega}\right).$$

The closure constants used in the $k - \omega$ SST model take the following values:

$$\alpha_\infty^* = 1, \qquad \alpha_0 = 1/9\,, \qquad \alpha_0^* = \beta_i/3\,, \qquad \beta_\infty^* = 0.09, \qquad \beta_i = 0.072, \tag{I.28}$$

$$a_1 = 0.31, \qquad \sigma_{k,1} = 1.176, \qquad \sigma_{k,2} = 1.0, \qquad \sigma_{\omega,1} = 2.0,$$

$$\sigma_{\omega,2} = 1.168, \quad \beta^* = 0.09, \qquad \beta_{i,1} = 0.075, \qquad \beta_{i,2} = 0.0828,$$

$$R_\beta = 8, \qquad R_k = 6, \qquad R_\omega = 2.95.$$

Appendix II S-A DDES Turbulence Model

The Spalart-Allmaras (S-A) DDES model [118] has one transport equation for the modified turbulent kinematic viscosity $\tilde{\nu}$, which is identical to the turbulent kinematic viscosity except in the near-wall region; namely,

$$\frac{\partial}{\partial t}(\bar{\bar{\rho}}\tilde{\nu}) + \frac{\partial}{\partial x_j}\left(\bar{\bar{\rho}}\tilde{\nu}\hat{u}_j\right) = \frac{\partial}{\partial x_j}\left[\left(\frac{\mu + \bar{\bar{\rho}}\tilde{\nu}}{\sigma_{\tilde{\nu}}}\right)\frac{\partial\tilde{\nu}}{\partial x_j}\right] + C_{b2}\bar{\bar{\rho}}(\frac{\partial\tilde{\upsilon}}{\partial x_j})^2 + G_{\tilde{\nu}} - Y_{\tilde{\nu}}. \quad (I.29)$$

The turbulent viscosity production term $G_{\tilde{\nu}}$ and the turbulent viscosity destruction term $Y_{\tilde{\nu}}$ are determined from the following parameterization:

$$G_{\tilde{\nu}} = (1 - f_{t2})C_{b1}f_{r1}\bar{\bar{\rho}}\tilde{S}\tilde{\nu}, \quad (I.30)$$

$$Y_{\tilde{\nu}} = \bar{\bar{\rho}}\left(C_{w1}f_w - \frac{C_{b1}}{\kappa^2}f_{t2}\right)\left(\frac{\tilde{\nu}}{\tilde{d}}\right)^2,$$

where

$$f_{t2} = C_{t3}\exp(-C_{t4}\chi^2), \qquad f_w = g\left(\frac{1 + C_{w3}^6}{g^6 + C_{w3}^6}\right)^{1/6}, \quad (I.31)$$

$$g = r + C_{w2}(r^6 - r), \qquad r = \frac{\tilde{\nu}}{\tilde{S}\kappa^2\tilde{d}^2}.$$

The rotation function can be expressed as

$$f_{r1} = (1 + C_{r1})\frac{2r^*}{1 + r^*}[1 - C_{r3}\arctan(C_{r2}\tilde{r})] - C_{r1}, \tag{I.32}$$

where

$$r^* = \frac{|S|}{|\Omega|}, \qquad \widehat{\Omega}_{ij} = \frac{1}{2}\left(\frac{\partial \hat{u}_i}{\partial x_j} - \frac{\partial \hat{u}_j}{\partial x_i}\right), \tag{I.33}$$

$$\tilde{r} = 2\widehat{\Omega}_{jk}\hat{S}_{jk}\left(\frac{D\hat{S}_{ij}}{Dt}\right)\frac{1}{D^4}, \qquad D = \frac{1}{2}(|S|^2 + |\Omega|^2).$$

In Eq. (I.33), $\frac{D}{Dt}$ represents Lagrangian derivative. The modulus of the mean rate of rotation tensor is defined as

$$\Omega = \sqrt{2\widehat{\Omega}_{ij}\widehat{\Omega}_{ij}}. \tag{I.34}$$

The length scale $\tilde{d} = d$ is the distance between the cell center and the nearest wall. The deformation parameter $\tilde{S}$ has the following expression:

$$\tilde{S} = S + \frac{\tilde{\nu}}{\kappa^2\tilde{d}^2}f_{v2}, \qquad f_{v2} = 1 - \frac{\chi}{1 + \chi f_{v1}}, \tag{I.35}$$

$$f_{v1} = \frac{\chi^3}{\chi^3 + C_{v1}^3}, \quad \chi = \frac{\tilde{\nu}}{\nu}.$$

Dacles-Mariani et al. [148], [149] proposed a modification of the model for the calculation of the mean rate of strain tensor as

$$S = |\Omega| + C_{prod} \min[0, |S| - |\Omega|]. \tag{I.36}$$

The closure constants used in the S-A model for DDES calculation is specified as follows:

$$C_{b1} = 0.1355, \qquad C_{b2} = 0.622, \qquad C_{w1} = \frac{C_{b1}}{\kappa^2} + \frac{(1 + C_{b2})}{\sigma_{\tilde{\nu}}}, \tag{I.37}$$

$$C_{b2} = 0.622, \qquad \sigma_{\tilde{\nu}} = 2/3\,, \qquad C_{v1} = 7.1,$$

$$C_{v2} = 5.0, \qquad C_{w2} = 0.3, \qquad C_{w3} = 2.0$$

$$\kappa = 0.41, \qquad C_{t3} = 1.1, \qquad C_{t4} = 2.0,$$

$$C_{r1} = 1.0, \qquad C_{r2} = 12.0, \qquad C_{r3} = 1.0. \qquad C_{prod} = 2.0.$$

The turbulent dynamic viscosity is then calculated using $\mu_t = \rho \tilde{\nu} f_{v1}$.

Appendix III CPU Hours Summary

The CPU hours used for both the NACA 0012 airfoil trailing edge noise and the WINPhase 10 small commercial wind turbine case are summarized in the table shown below.

Table III.1: Summary of CPU hours used in the simulations of NACA 0012 airfoil and WINPhase 10 wind turbine.

Case	CPU hours		
	CFD	Acoustic propagation	Acoustic beamforming
NACA 0012	5006	26	1
WINPhase 10	12672	30	1.5

Appendix IV Acoustic Beamforming Results for WINPhase 10 Wind Turbine Case

Figures IV.1 and IV.2 display acoustic maps for WINPhase 10 commerical small HAWT using the Archimedean spiral and star array, respectively, for an inflow reference wind speed of 10 m s^{-1}.

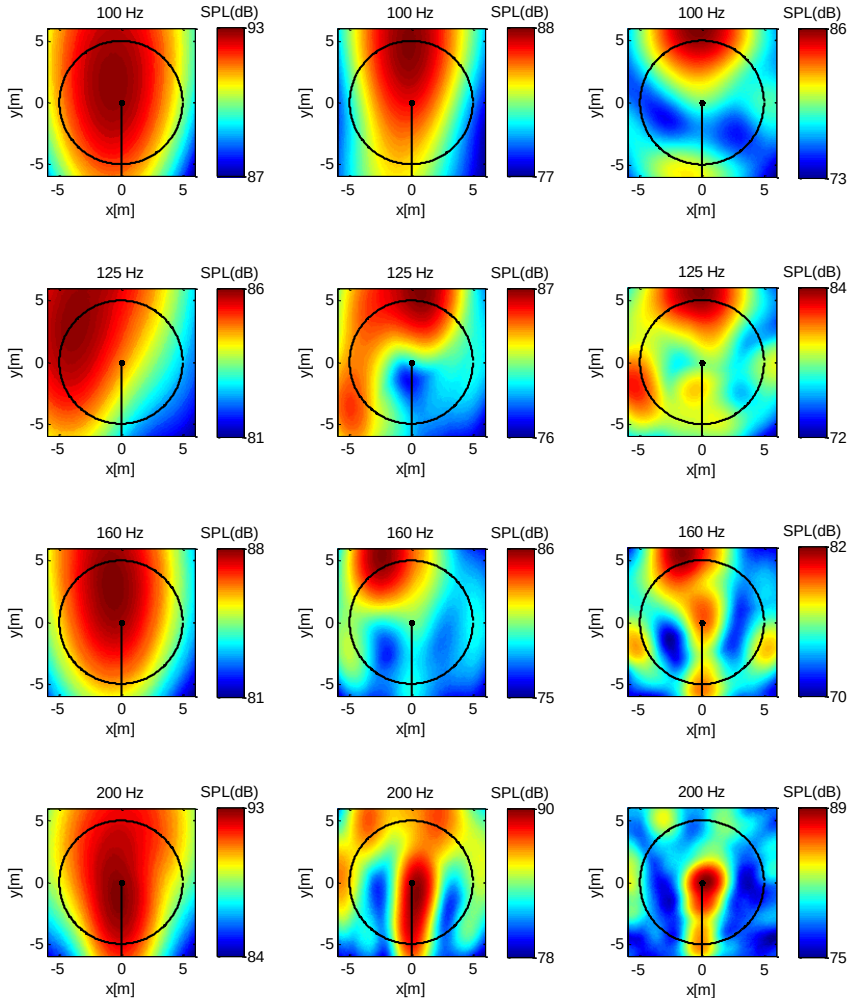

Figure IV.1: Numerical acoustic maps for the Archimedean spiral array: 8 m × 8 m horizontal array at ground level (left column), 20 m × 20 m horizontal array at ground level (middle column); 20 m × 20 m vertical array parallel to the wind turbine rotor plane (right column). The incident wind speed is 10 m s^{-1}. The wind turbine rotates in the counter-clockwise direction.

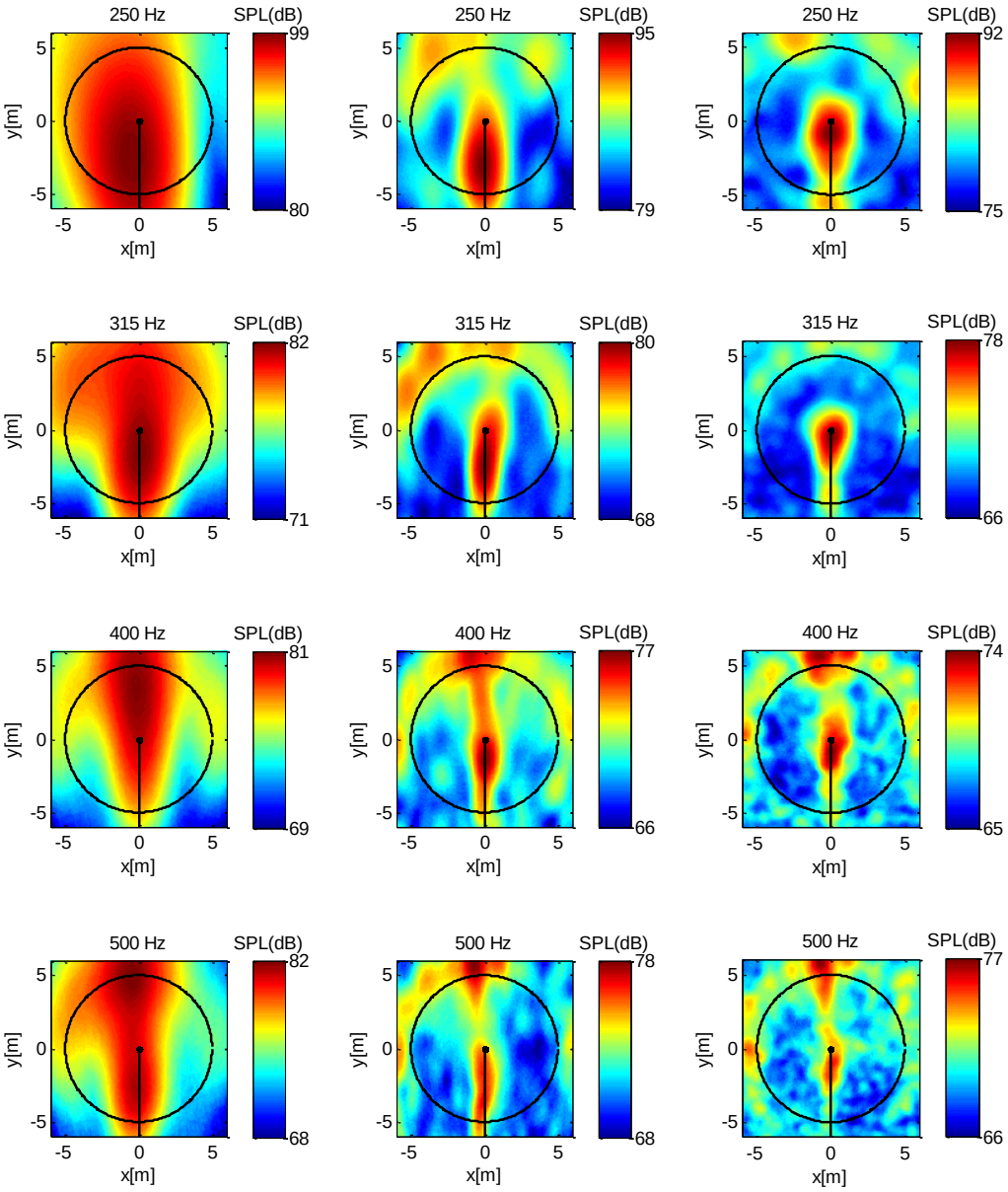

Figure IV.1 (continued).

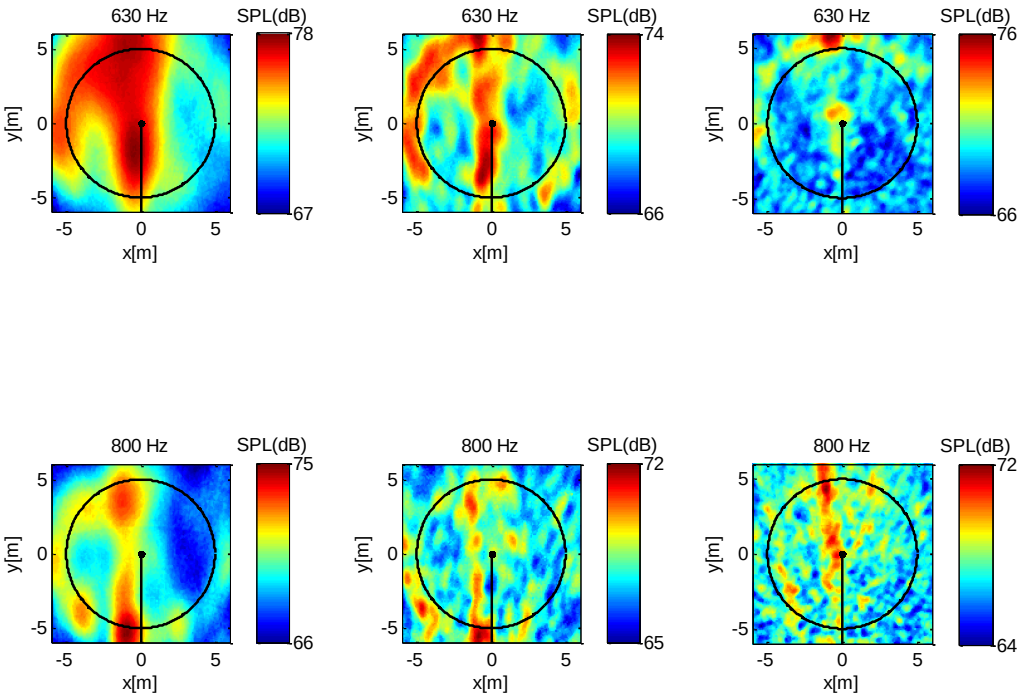

Figure IV.1 (continued).

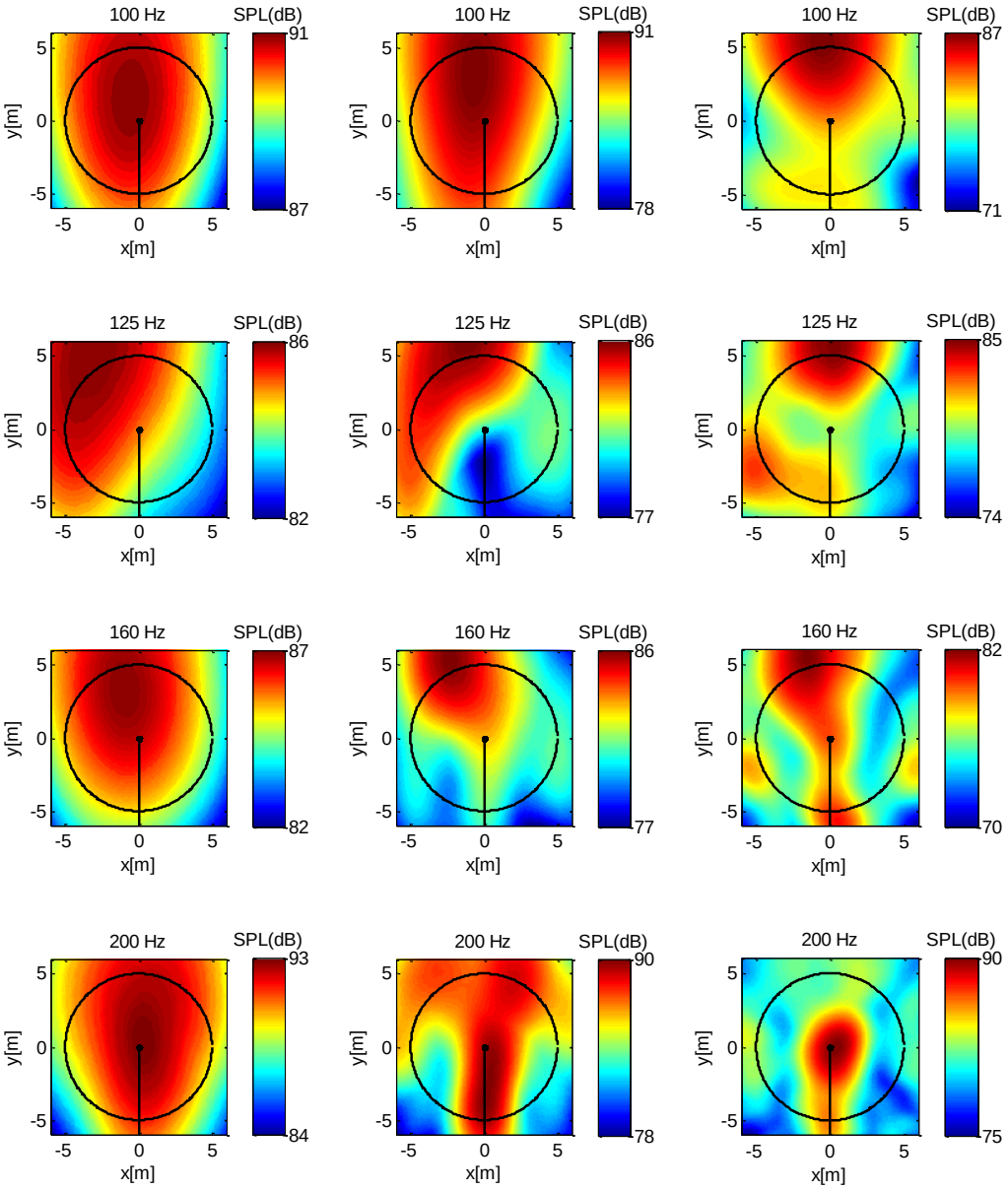

Figure IV.2: Numerical acoustic maps for the star spiral array: 8 m × 8 m horizontal array at ground level (left column), 20 m × 20 m horizontal array at ground level (middle column); 20 m × 20 m vertical array parallel to the wind turbine rotor plane (right column). The incident wind speed is 10 m s^{-1}. The wind turbine rotates in the counter-clockwise direction.

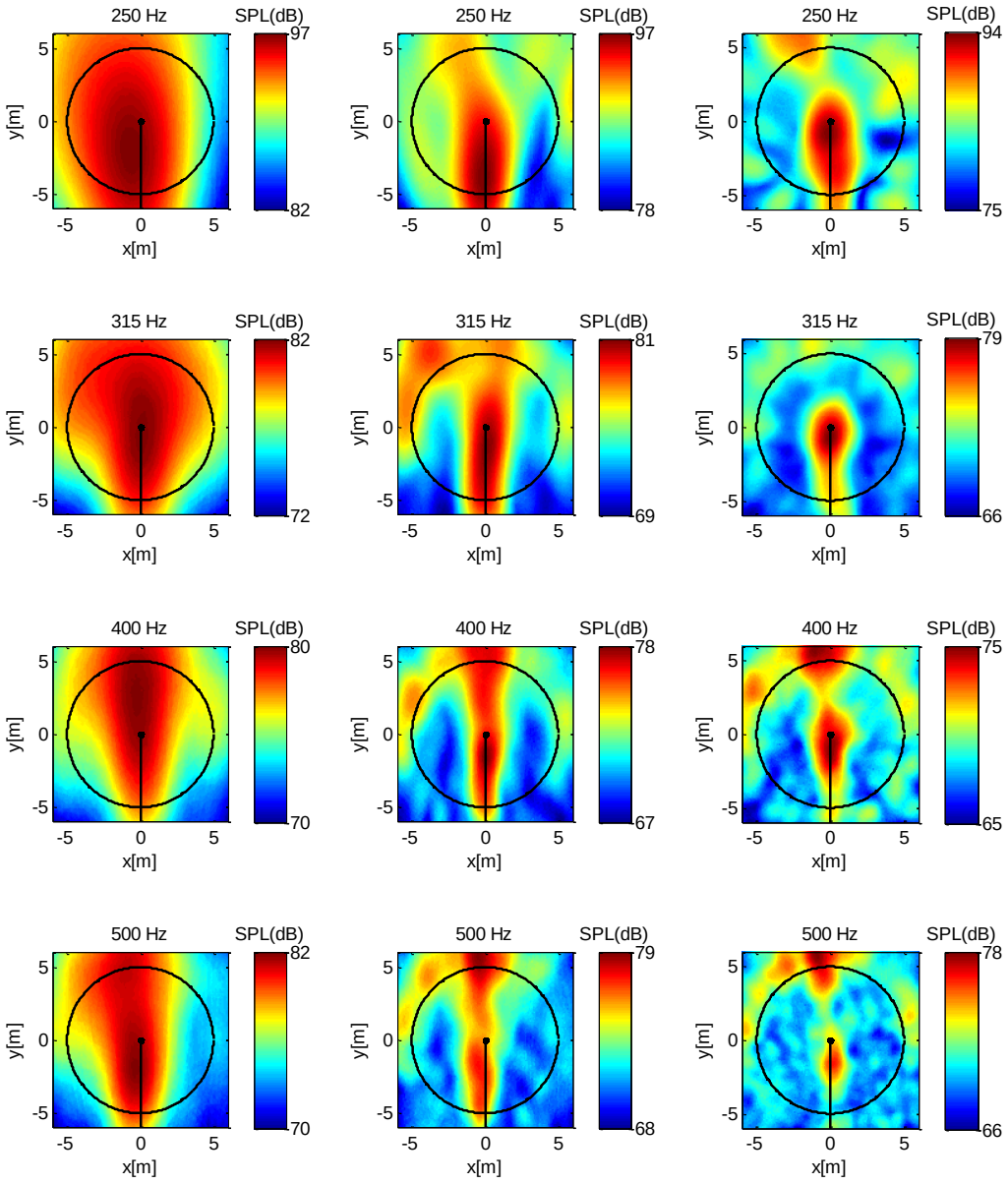

Figure IV.2 (continued).

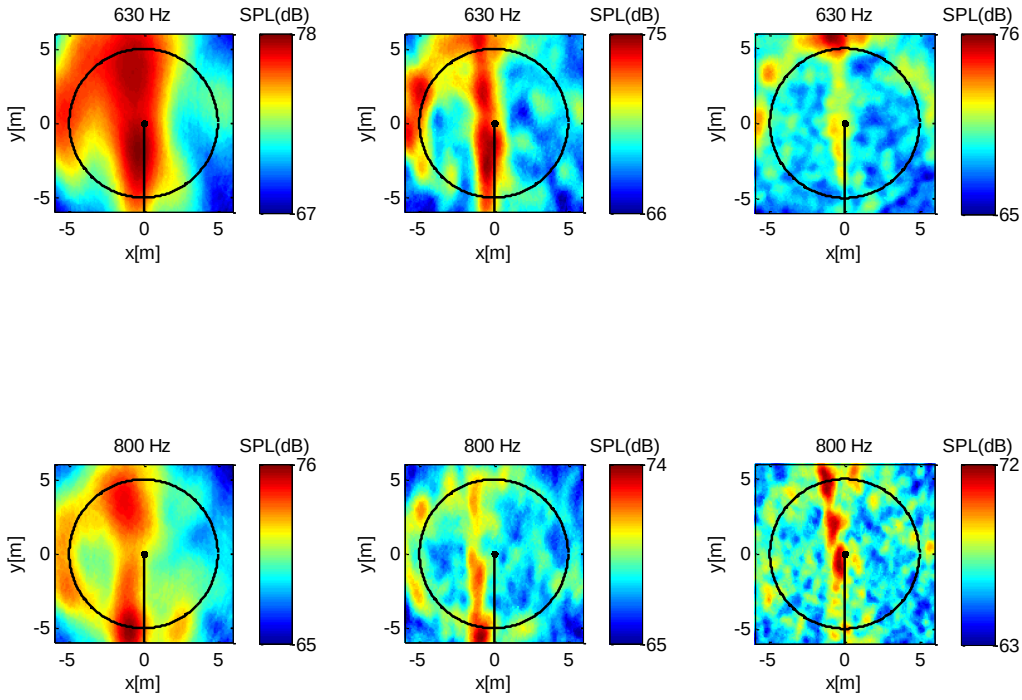

Figure IV.2 (continued).

Figures IV.3 and IV.4 display acoustic maps for the WINPhase 10 commercial small HAWT using the Archimedean spiral and star array, respectively, for an incident wind speed of 11 m s^{-1}.

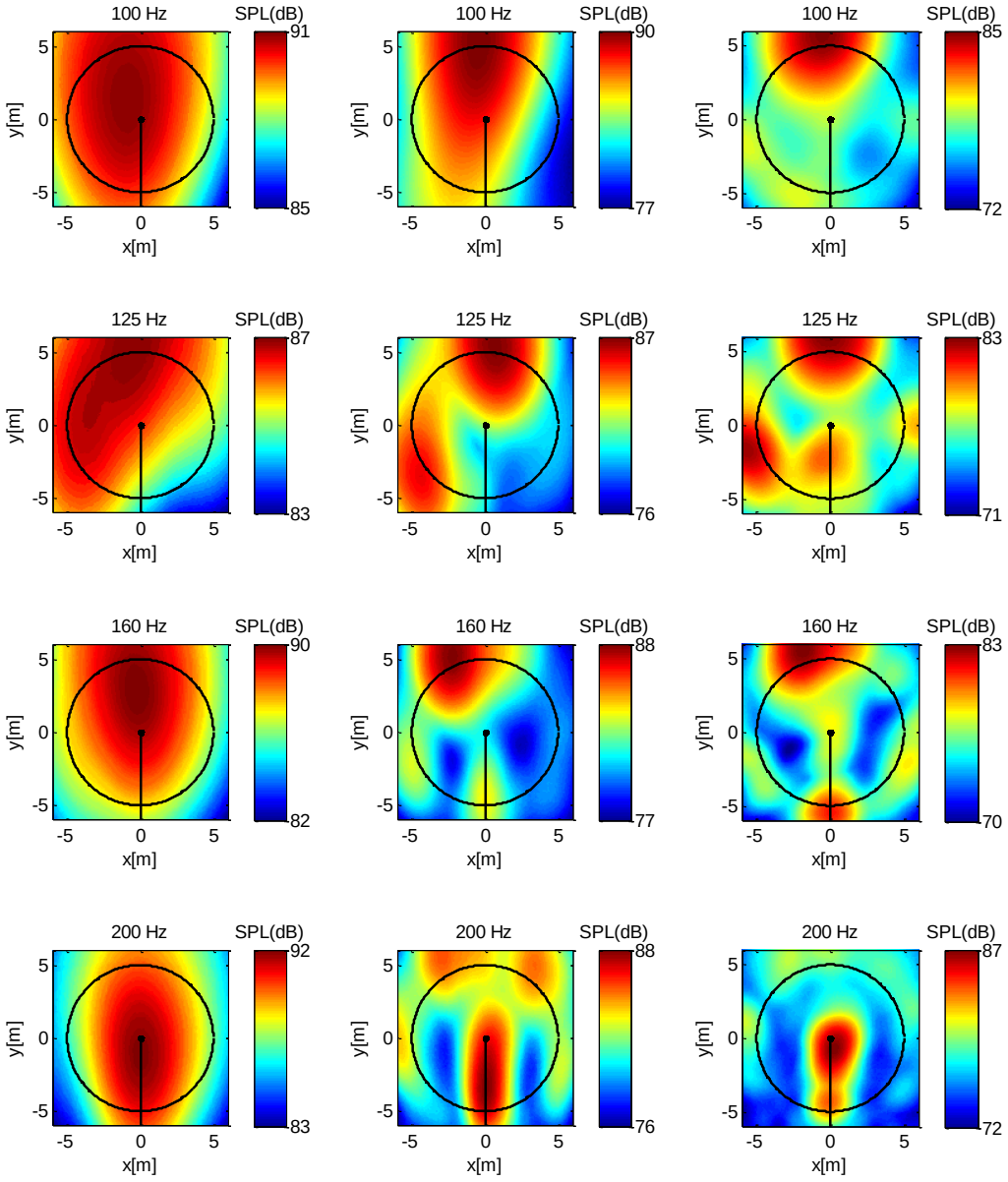

Figure IV.3: Numerical acoustic maps for the Archimedean spiral array: 8 m × 8 m horizontal array at ground level (left column), 20 m × 20 m horizontal array at ground level (middle column); 20 m × 20 m vertical array parallel to the wind turbine rotor plane (right column). The incident wind speed is 11 m s^{-1}. The wind turbine rotates in the counter-clockwise direction.

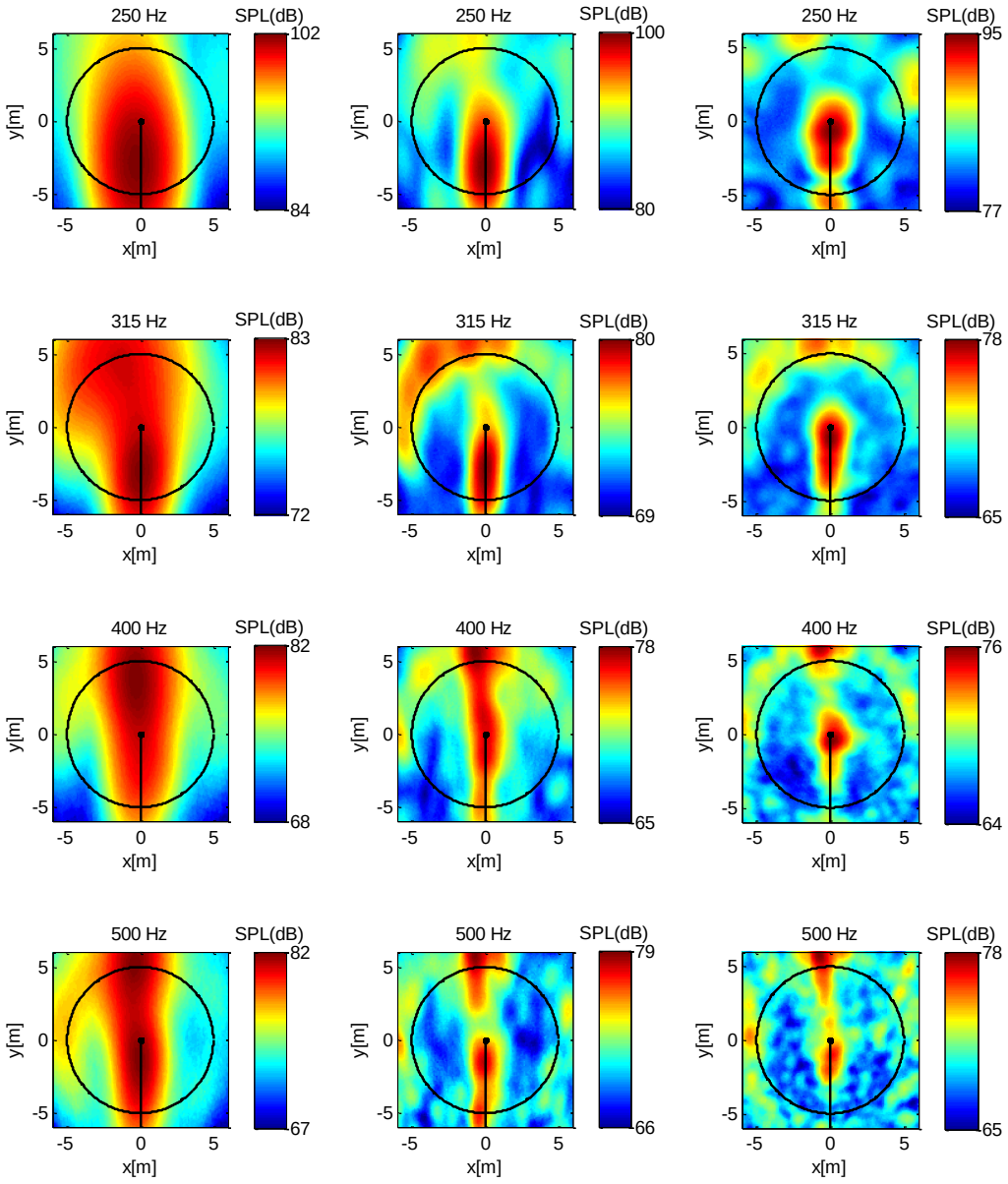

Figure IV.3 (continued).

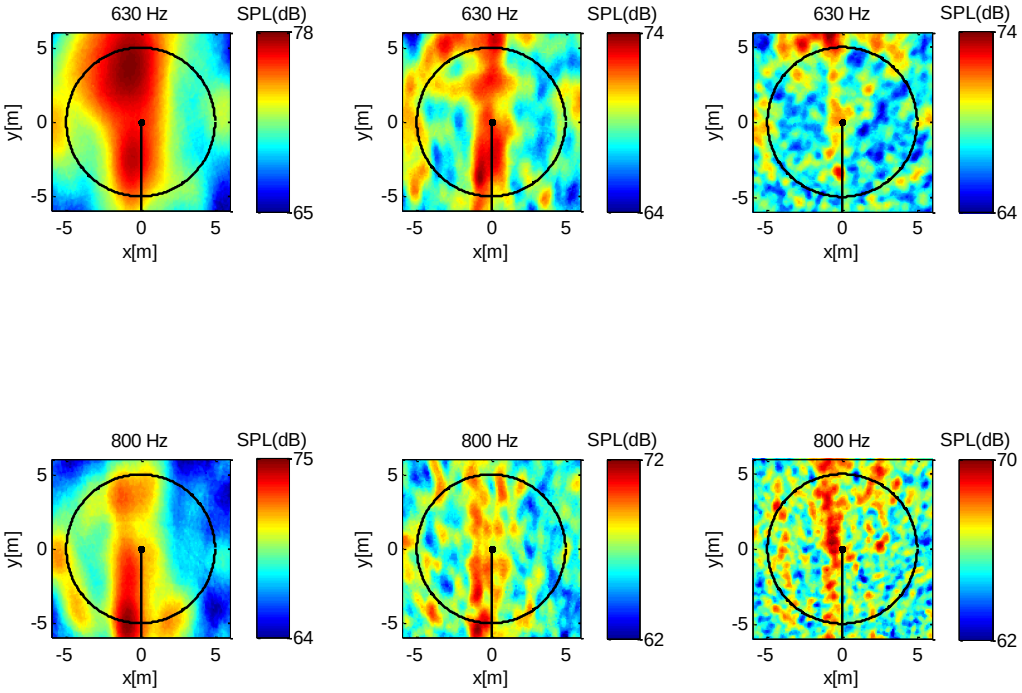

Figure IV.3 (continued).

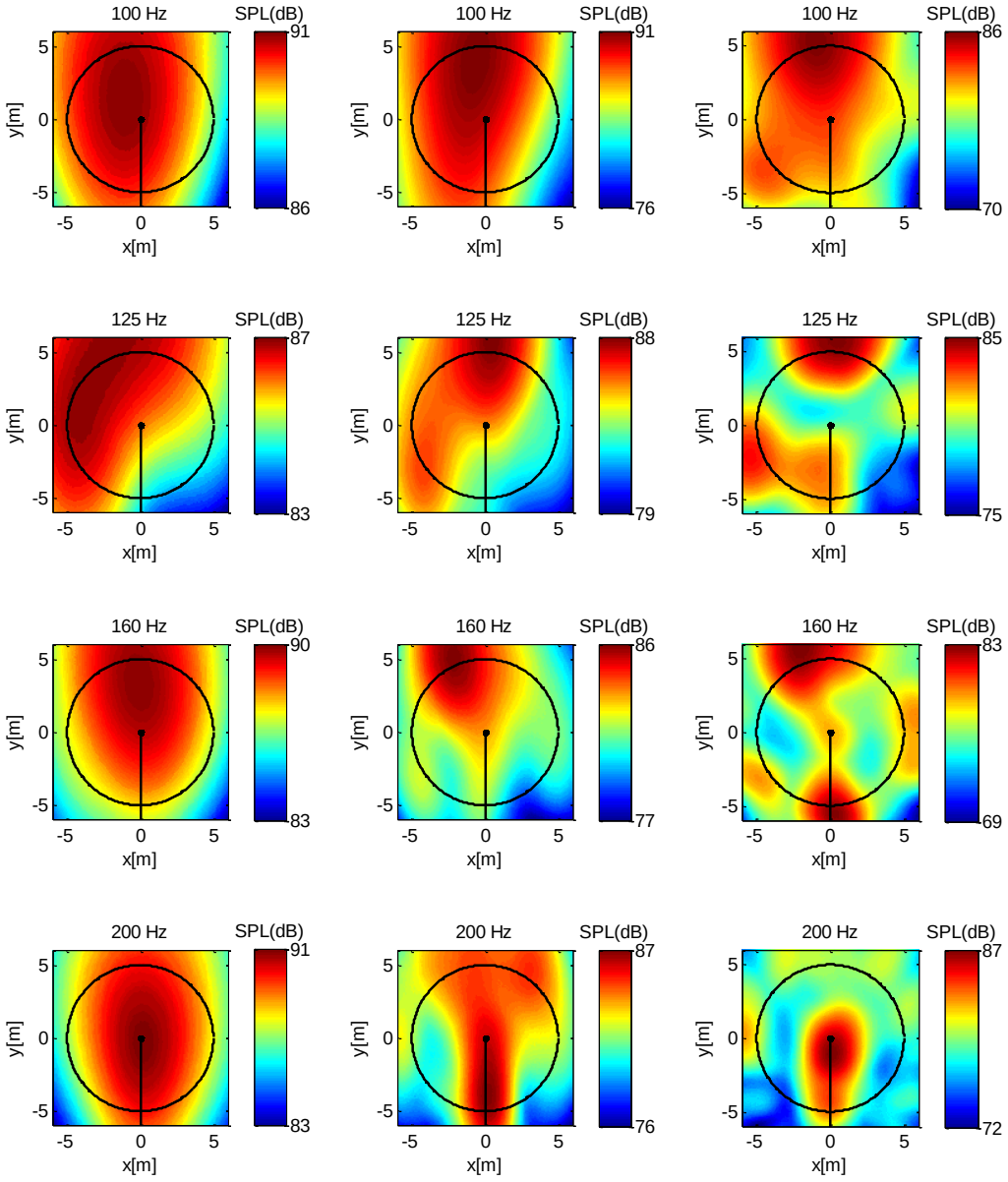

Figure IV.4: Numerical acoustic maps for the star spiral array: 8 m × 8 m horizontal array at ground level (left column), 20 m × 20 m horizontal array at ground level (middle column); 20 m × 20 m vertical array parallel to the wind turbine rotor plane (right column). The incident wind speed is 11 m s^{-1}. The wind turbine rotates in the counter-clockwise direction.

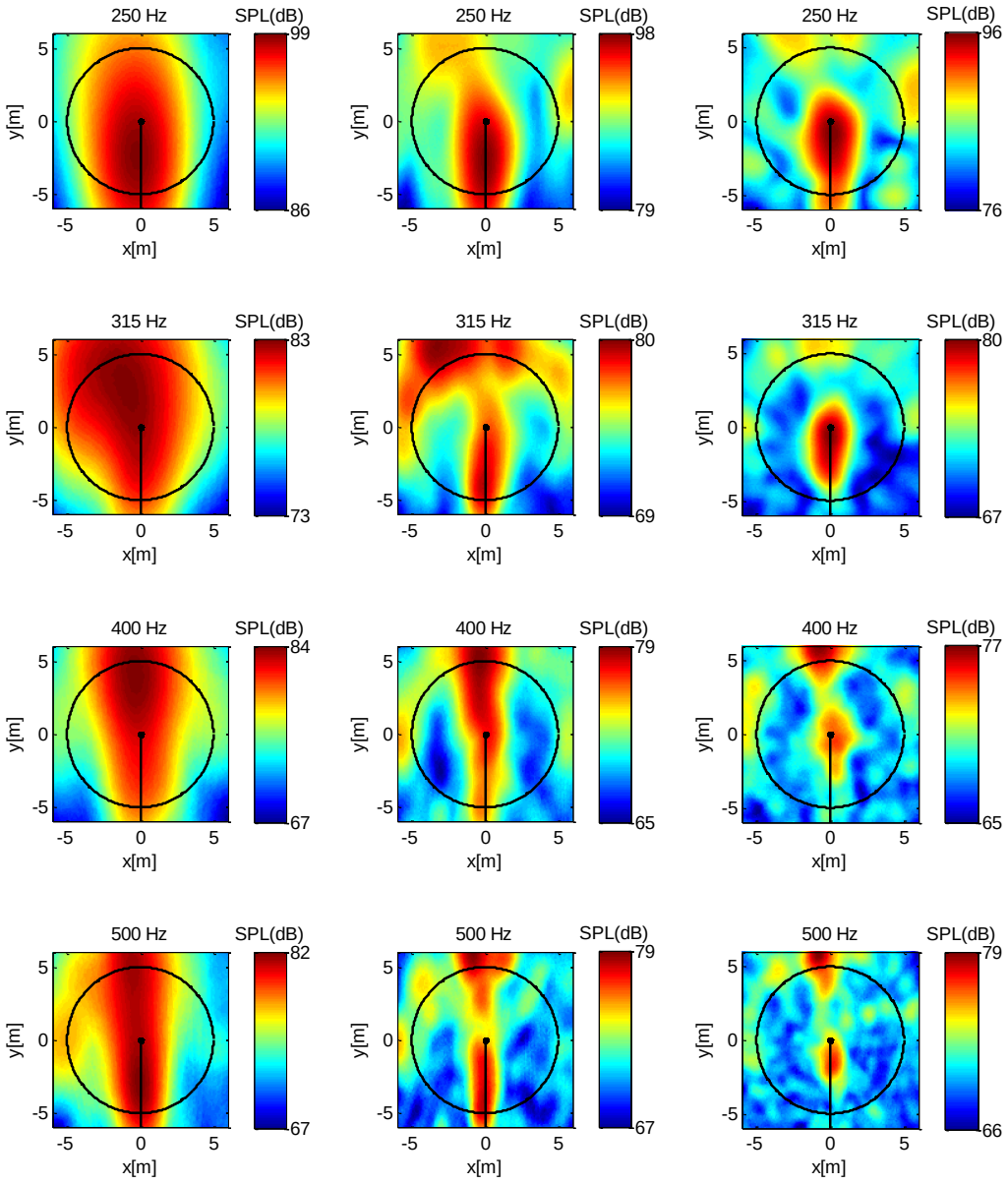

Figure IV.4 (continued).

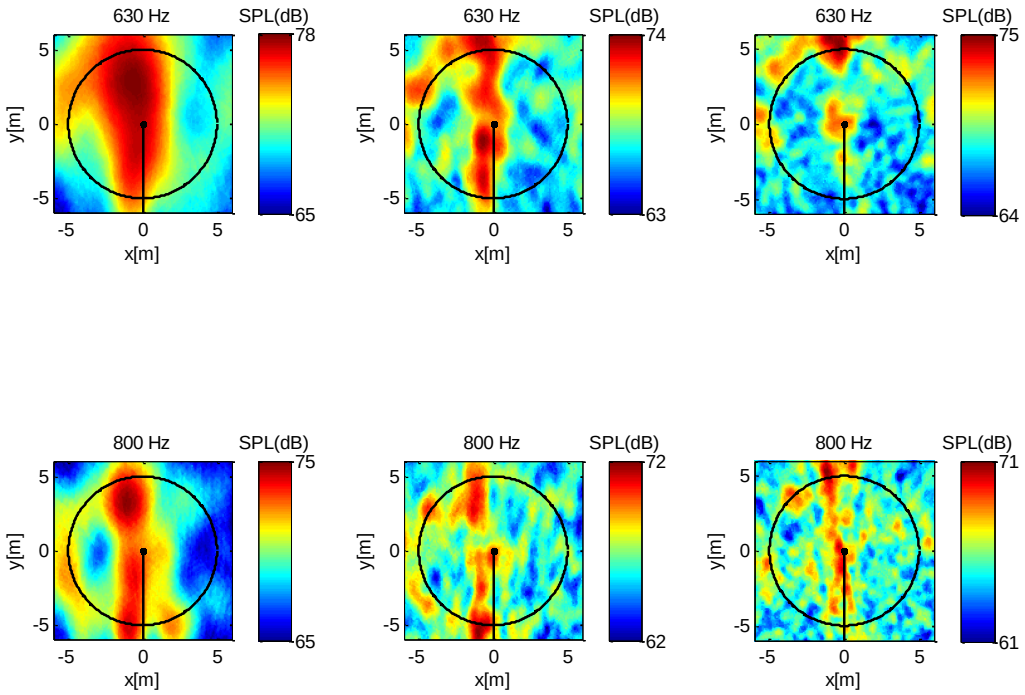

Figure IV.4 (continued).

Figures IV.5 and IV.6 show the maximum SPL on the acoustic maps at center frequency of each one-third octave band for the WINPhase 10 small commercial HAWT at reference wind speeds of 10 m s^{-1} and 11 m s^{-1}, respectively.

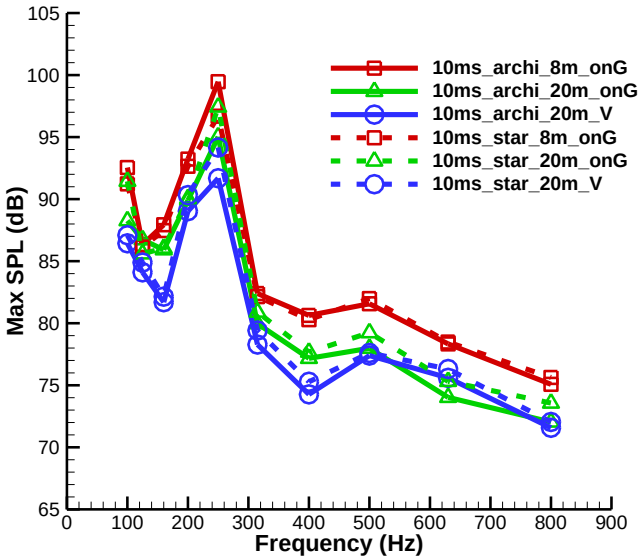

Figure IV.5: Max SPL vs. frequency for an incident wind speed of 10 m s^{-1}.

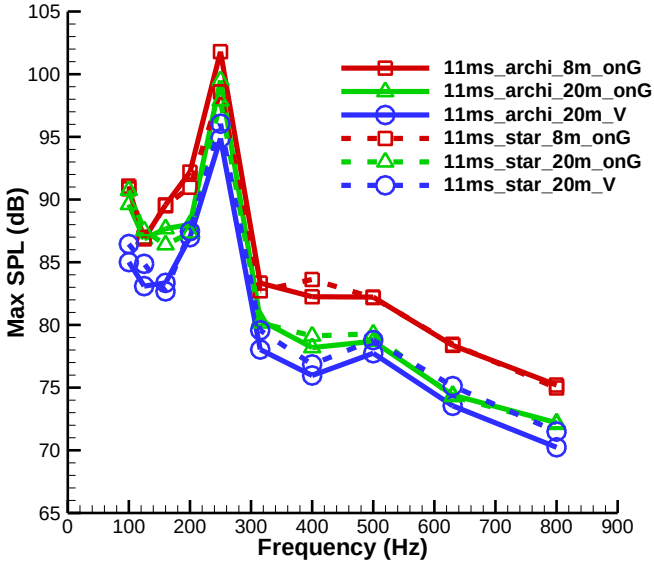

Figure IV.6: Max SPL vs. frequency for an incident wind speed of 11 m s^{-1}.